공학박사학위논문

수직 와후류 시스템의 소산 특성에 대한 연구

Study on Decay Characteristics of Vertical Four-Vortex Systems

2020 년 2 월

서울대학교 대학원

기계항공공학부

조 준 호

수직 와후류 시스템의 소산 특성에 대한 연구

Study on Decay Characteristics of Vertical Four-Vortex Systems

지도교수 이 관 중

이 논문을 공학박사 학위논문으로 제출함

2019 년 11 월

서울대학교 대학원

기계항공공학부

조 준 호

조준호의 공학박사 학위논문을 인준함

2019 년 12 월

위 원 장 : _____

부위원장 : _____

위 원 : _____

위 원 : _____

위 원 : _____

Abstract

Study on Decay Characteristics of Vertical Four-Vortex Systems

Junho Cho
School of Mechanical and Aerospace Engineering
The Graduate School
Seoul National University

The wake vortices of an aircraft descend by self-induction that enables a pilot to identify wake locations. A pilot taking off an aircraft can avoid a wake vortex encounter by performing early rotation and flying at or above the climb path of the preceding aircraft. Such an operation results in a situation, in which two wake vortices are present in the air simultaneously in close proximity. Also, there is a possibility of interactions among vortices where runways are parallel so that a pair of vortices from an aircraft moves to another runway due to crosswind. If the interaction between wake vortex pairs induces a rapid dissipation, it may be possible to adjust the take-off separation time and, therefore, in-crease the airport capacity.

In this study, the transport and decay characteristic processes involving

interactions between the wake vortex pairs formed by the preceding and following aircraft have been analyzed. The decay processes were analyzed by selecting suitable initial conditions that took into account the high altitude of the following aircraft and the descent of the preceding wake vortices. The high altitude of the following aircraft was included as initial conditions, and atmospheric turbulence conditions were applied to large eddy simulations to account for the vortex core instability and non-linear transport and decay. The obtained results were analyzed to identify the decay characteristic processes that induce the rapid dissipation of the wake vortices and their conditions.

The numerical simulation results were analyzed to identify the decay processes that induce the rapid dissipation of wake vortices such as merging into a single counter-rotating pair, rapid dissipation, and formation of a vortex ring with or without a deformation of the lower vortex pair. The third process could be effectively used to adjust the take-off separation time for increasing the capacity at airports.

Key Words : Aircraft wake vortex, Vortex interaction, Computational fluid dynamics, Take-off separation, Air traffic management

Student Number : 2015-30174

Table of Contents

Nomenclatures

Symbols

b_0	initial spacing of a vortex pair
b	lateral spacing of a vortex pair
h	initial vertical distance
L	size of computational domain
L_{ii}	longitudinal integral length scale
Re_Γ	circulation-based Reynolds number
R_Γ	Γ_u/Γ_l, circulation ratio of a vortex pair
$\mathrm{r_c}$	vortex core radius
t_0	b_0/V_0, characteristic vortex time scale
$t_{lifespan}$	time required for linking a counter-rotating vortex pair
V_0	$\Gamma_0/(2\pi b_0)$, initial descent rate of a vortex pair
$\mathbf{X}^{\mathrm{c}}$	$(\mathrm{x}, \mathrm{y}, \mathrm{z})$, location center with x: longitudinal axis, y: lateral axis, and z: vertical axis
ε	turbulence eddy dissipation rate
ε_f	energy forcing amplitude
τ	$4\pi b_0^2/(\Gamma_u + \Gamma_l)$, orbital period for isolated vortex pair
Δ	grid size
$\Delta \mathrm{z}_{lifespan}$	vertical distances of two vortex pair at the time of linking
$\Gamma(\mathrm{r})$	circulation distribution according to vortex core radius
Γ_{5-15}	averaged circulation between a radius of 5m to 15m
Γ_{tot}	total circulation
Γ_0	initial circulation
$\boldsymbol{\omega}$	vorticity vector

Subscripts

$\cdot_u$	upper wake vortex pair
$\cdot_l$	lower wake vortex pair
$\cdot_{ss}$	starboard side vortices
$\cdot_{ps}$	port side vortices

Superscripts

$\cdot^*$	dimensionless quantity using characteristic scale $(b_0,\ V_0,\ \Gamma_0,\ t_0)$
$\bar{\cdot}$	longitudinal averaged quantity
$\tilde{\cdot}$	quantity averaged over a vortex segment

Abbreviations

V4VS	vertical four-vortex system
LES	large eddy simulations
H4VS	horizontal four-vertex system
SNGR	stochastic noise generation and radiation
DVM	deterministic wake vortex model
TDP	TASS driven algorithms for wake prediction

List of Tables

List of Figures

Chapter 1. Introduction

1.1 Airport capacity and wake vortex

Air traffic has been forecasted to be the largest on record in this year and has grown steadily by about four percent every year. The airport logistics capacity has reached its limit with the steady increase of aviation demands. In order to cope with the increasing air traffic, there has been a growing interest in improving the capacity of the airport by adjusting the interval between aircraft during take-off and landing.

Wake vortices are generated as a consequence of a lift generation of aircraft's finite wings. They span for several miles on the aircraft route after the creation and dissipate after several minutes and effect as a potential risk for the following aircraft. Wake vortices are formed mainly at the wingtip of an aircraft because of pressure difference between the upper and the lower part of the wing. Vortices are rolled up to a single pair of counter rotating ones. The initial lateral separation, b_0, of vortices is about 70-80% length of the wingspan [1]. Due to the rolling moment generated by the wake vortices, a following aircraft may lose its controllability and descend abruptly, or even may crash into the ground (Fig. 1-1). It is reported that the incidents caused by wake vortices occur frequently during approach to the airport or low altitude flight [2]. For example, in January 2008, Air Canada A319 dived 1,400 feet with maximum of 55° rolling because of the wake vortices from B747-400 which was flying 11 NM ahead. In order to prevent such accidents, the International Civil Aviation Organization (ICAO) and the Federal Aviation Administration (FAA) have designated separation intervals according to the size difference between the leading aircraft and the

following one, so that the aircraft can be operated safely [3].

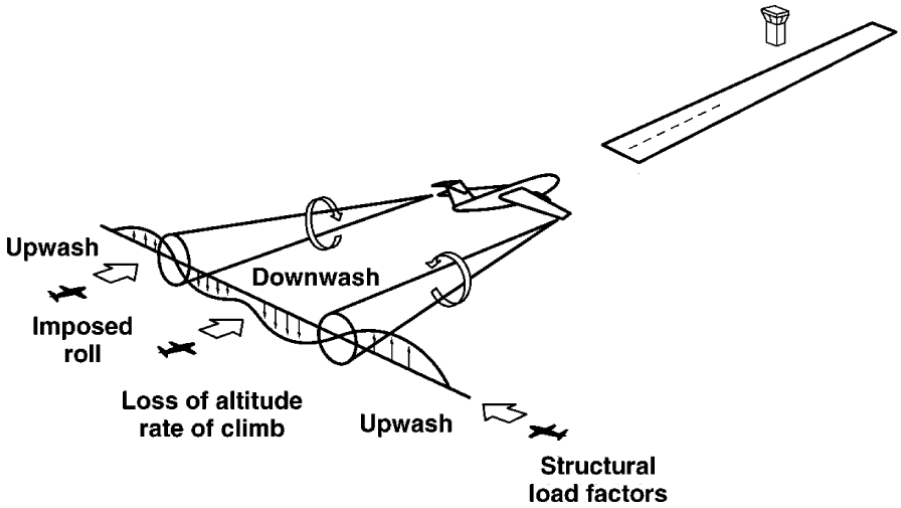

Fig. 1-1 Possible encounters with lift-generated wake by a following aircraft [4]

The aircraft is classified into four categories based on the maximum take-off mass (MTOM). Those are A380-800, heavy (136,000 kg or more), medium (7,000 kg or more and 136,000 kg or less) and light (7,000 kg or less). However, in the medium class for example, the difference between the maximum value and the minimum value is significant, which is about 130 t. It means that there can be difference of up to 130 t among medium class aircraft. In other words, if considering two different airplanes categorized as a medium aircraft, for example, A320 and ERJ-145, are following the heavy class aircraft A340-600, the separation to the preceding aircrafts as 5 NM can be too conservative for the A320. Therefore, research about re-categorizing the current aircraft classification into more subdivision categories is

on the way at the moment (Table 1.1,

Table 1.2) [5].

Table 1.1 Example aircraft assignment to proposed six category system [6]

Category A	Category B	Category C	Category D	Category E	Category F
A380 AN-225	B747 series A340 series B777 series A330 series B787 series …	MD11 B767 A306 A310 DC8 DC10 C-17 C-135 B-1 B-2	B757 series B737 series A320 series B727 series MD80 series …	AT72 RJ100 RJ85 B463 B462 E170 CRJ1/2 CRJ7/9 AT45 AT43 GLF4 SF34 DH8A/B/C E135/145	E120 B190 C650 H25B C525 GA multi-engine aircraft GA single engine aircraft

Table 1.2 RECAT wake separation standards [6]

Leader	Follower (Nautical Mile)						
		A	B	C	D	E	F
	A	MRS	5	6	7	7	8
	B	MRS	3	4	5	5	7
	C	MRS	MRS	MRS	3.5	3.5	6
	D	MRS	MRS	MRS	MRS	MRS	5
	E	MRS	MRS	MRS	MRS	MRS	4
	F	MRS	MRS	MRS	MRS	MRS	MRS

MRS: Minimum Radar Separation

It is also possible to increase the aircraft capacity by constructing another runway to airports, but it is limited because of problems such as securing site, and huge cost needed to build one. Therefore, in order to adjust the separation that is empirically set at the moment, it is necessary to study the transport and decay of the wake vortices from an aircraft. Thus, a method for improving the efficiency of airport capacity has been required while ensuring the safety. For this, it is recommended to reduce the time interval of the take-off and landing of consecutive aircraft. Meanwhile, unreasonable shortening of aircraft spacing would cause an accident due to the wake turbulence. Dissipation and behavior of wake vortex pair are dependent on the meteorology such as clear air turbulence, horizontal wind velocity, and the strength of wake vortex pair. Therefore, take-off and landing time interval must be controlled efficiently with the consideration of the meteorology condition.

Considering the environment of an airport (Fig. 1-2), it is also possible that a pair of vortices is generated in the atmosphere where another pair of vortices from the preceding aircraft still exists. For example, runways are parallel so that a pair of vortices from an aircraft moves to another runway path due to crosswind. In addition, the flight paths may cross each other. In such cases, the vortices of the following aircraft are influenced by interacting with the other vortices remained in the atmosphere. Therefore, it is necessary to clarify the transport and decay mechanism of the vortices considering the interaction with another pair of vortices.

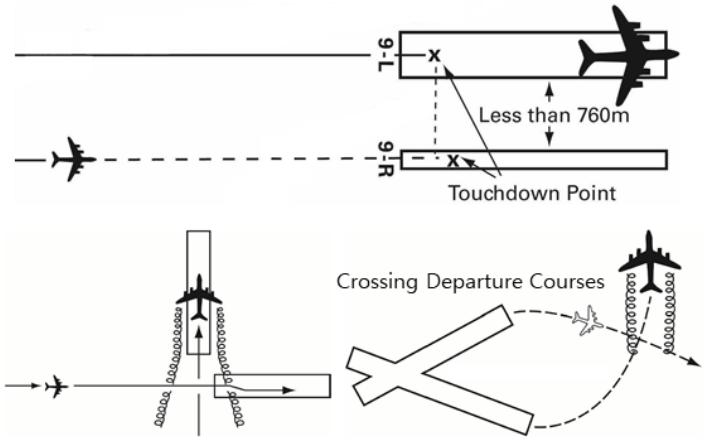

Fig. 1-2 Situation example where crossing of aircraft vortices can occur behind an aircraft; NATS Services [7]

The wake vortices descend by self-induction that enables a pilot to identify the wake location and perform a required avoidance maneuver. The initial vortex descent rate is determined by the weight, speed, and wingspan of the aircraft. Generally, vortices descend at the initial rate of about 300 to 500 feet per minute for about 30 seconds. The descent rate decreases and eventually approaches zero at between 500 and 900 feet below the flightpath. As shown in Fig. 1-3, the pilot taking off an aircraft can avoid a wake vortex encounter by rotating before the rotation point of the preceding aircraft and flying at or above its climb path [8].

The dual-glideslope approach concept proposes two airplanes landing on the same runway, with one of them flying a standard approach and the other flying a higher approach and touching down later on the runway as shown in Fig. 1-4 [9]. The advantage of creating a higher approach is that separations between the lower (standard) glideslope and the upper glideslope can be reduced significantly compared to same-glideslope separations, due to

the sinking nature of wake vortices.

These operations result in a situation, in which two wake vortices are present in the air at the same time. These wake vortex pairs generated by the preceding and following aircraft can potentially interact with each other if the distance between them is relatively small. If this interaction accelerates the vortex dissipation process, the take-off separation time for the next aircraft can be reduced, thus increasing the airport capacity limit. Therefore, it is necessary to examine the dissipation of newly generated wake vortices in the presence of the wake vortices produced by the preceding aircraft.

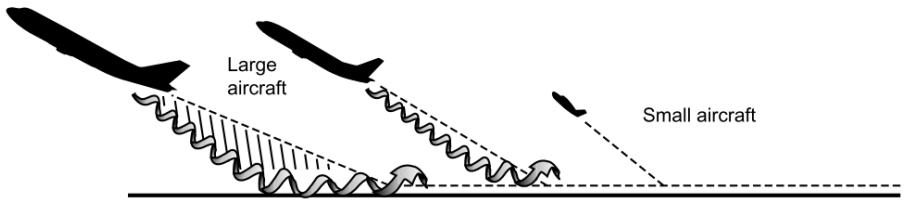

Fig. 1-3 Wake vortex avoidance maneuver performed behind a larger aircraft in the same runway [8]

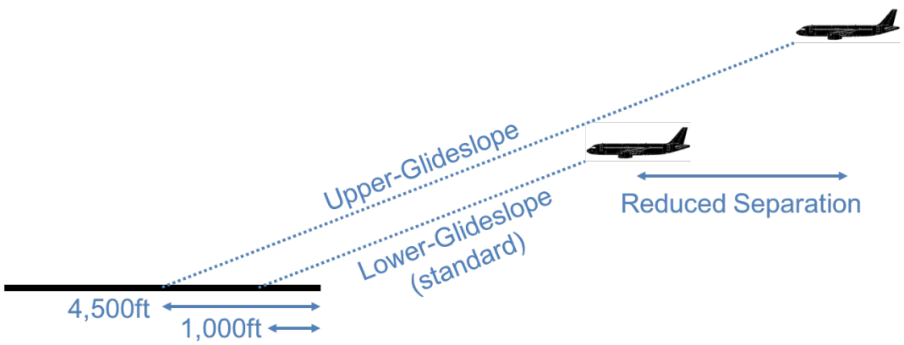

Fig. 1-4 dual glide slope concept to reduce the separation [9]

1.2 Previous study about wake vortex

Due to the importance of wake hazards to operational safety, various studies have been conducted on transport and decay of wake vortex over the last 50 years. The transport and decay of vortices are closely related to the surrounding atmospheric conditions such as turbulence intensity (ε) and stratification level [10–13]. Vortices show long-wave symmetric sinusoidal instability, which is also known as Crow instability [14], and the evolution of the instability is dependent of the atmospheric conditions. The parallel pair of vortices change their patterns due to Crow Instability and create a continuous vortex-ring like a train (Fig. 1-5). The time taken for making a ring is called the vortex lifespan and vortices dissipate rapidly after the formation of the ring. Crow and Bate have found that the life span of vortices is a function of the non-dimensional turbulence intensity [15]. This phenomenon is named after Crow who identified it firstly.

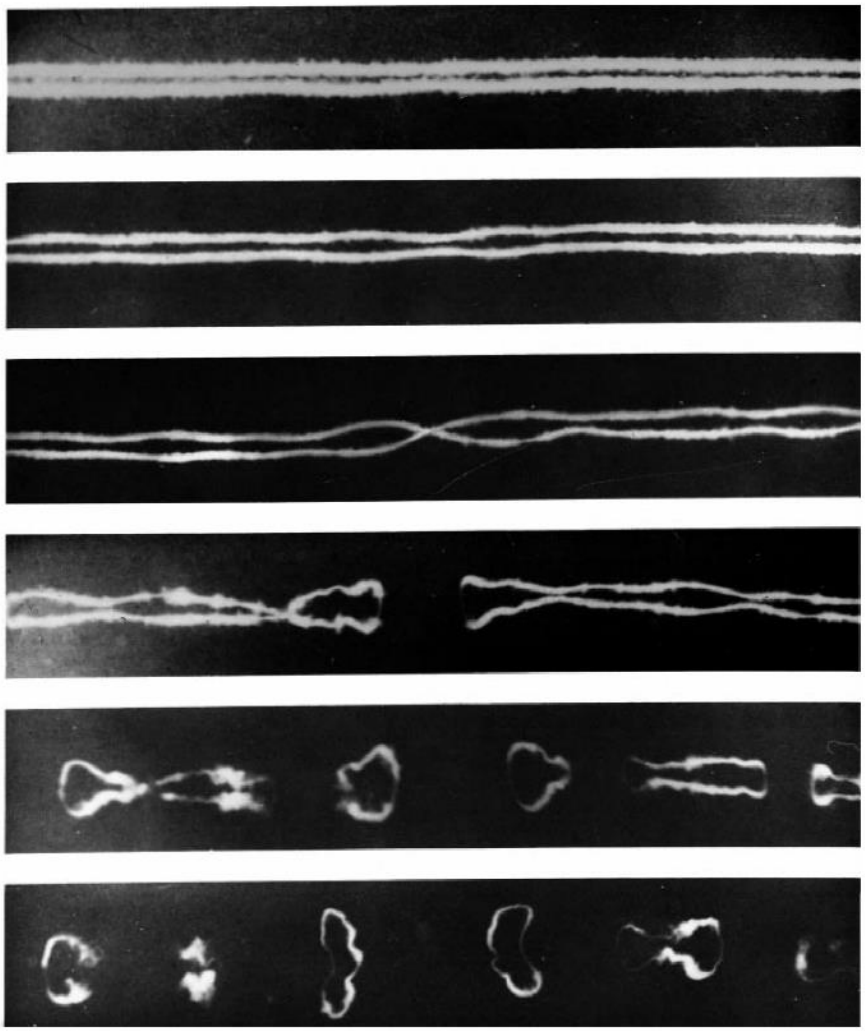

Fig. 1-5 Instability of a pair of trailing vortices of a B-47 aircraft photographed at intervals of 15 s after its passage [16]

The evolution of wake vortices proceeds through several stages including the roll-up, transport, and decay ones. During the transport and decay stages, the dissipation effects of the atmosphere on a single wake vortex pair were studied [10,13,15,17–22]. Crow and Bate materialized Crow instability in the process of wake vortex dissipation due to ambient turbulence [14]. At the transport stage of the wake vortex, the long-wave symmetric sinusoidal instability of core structure from atmospheric turbulence occurs along fixed and inclined planes. As a result, the two vortices are linked in the centerline, forming a train of the vortex ring. After the formation of the vortex ring, the parallel vortex pair rapidly dissipated, reducing the wake hazard for the trailing aircraft. Crow and Bate defined the vortex lifespan as the time of linking of the wake vortex pair and found that the vortex lifespan is a function of the non-dimensional turbulence intensity [15].

In addition, Sarpkaya and Daly showed that the non-dimensional descent distance of vortices is a function of the dimensionless time, turbulence intensity, and the longitudinal integral length scale [23]. Han et al. analyzed the influence of the turbulence intensity on the development of Crow Instability using the large eddy simulation [10]. It was found that the maximum amplified wavelength of instability and the vortex lifespan decrease as dimensionless turbulence intensity increases.

Recently, the influence of atmospheric stratification level on the Crow instability of aircraft wake vortices has been analyzed using LES [11]. If the stratification level is low or moderate, the development of Crow instability is promoted. Contrarily, at high stratification level, it is found that the instability of short wavelength is developed dominantly so the wake vortices are rapidly dissipated [12]. Visscher et al. found that stratification combined with weak ambient turbulence is an efficient mechanism to rapidly dissipate

wake vortex [13].

They focused on the relationship between the vortex dissipation and atmospheric conditions such as turbulence, stratification, and ground boundary layer. It was found that the dissipation mechanism consisted of two phases and that the vortex dissipation process could be quantified by constructing suitable decay models. Based on these findings, the hazard area for the next aircraft was calculated and was the basis for takeoff separation time [24,25]. In addition, various studies have been conducted on wake vortex for increasing airport capacity [26]. However, those studies did not consider the wake vortices generated by the preceding aircraft that were more condensed at a particular location and whose dissipating effect on the wake vortices of the following aircraft could be stronger than the other atmospheric parameters.

The wake vortex interactions occurred during the roll-up stage were investigated for the vortices detached from the high-lift configuration [27–33]. Based on the fundamental understanding of the vortex interaction, the vortex was controlled to alleviate the hazard by wake vortex. The vortex system containing a wing tip and inboard flap vortex pairs was defined as a horizontal four-vortex system (H4VS) to determine a method for weakening a fully rolled-up wake vortex pair by elucidating the control mechanism based on the fundamental understanding of vortex interactions.

Donaldson and Bilanin analyzed the evolution of 4HVS using the point vortex method and analyzed the behavior of 4HVS according to parameters such as vortex spacing ratio and circulation strength ratio [27]. Crouch analyzed the development of initial disturbance of 4HVS using linear instability analysis that extended Crow instability [34]. Rennich and Lele analyzed the behavior of counter-rotating 4HVS using vortex filament method and direct numerical simulation [28]. This study showed that the analysis using the

vortex filament method could be used as an initial investigation with sufficient accuracy for instability evolution. The instability of highly perturbed inboard vortices led to the rapid development of crow-type perturbation of outboard vortices and eventually led to the destruction of 4HVS.

Bristol et al. analyzed the initial sinuous instability of co-and counter-rotating unequal wake-vortex pairs using linear stability analysis and CFD calculation to reproduce the wrapping and ring-rejection behavior found in the towing tank experiments [35,36]. Babie et al. analyzed the development of instability according to the wavelength of the initial perturbation by constructing an experimental apparatus to generate 4HVS for use in the wake control strategy by uncovering the control method for rapid attenuation of 4HVS [32]. Stumpf studied the configuration of weakening the strength of the wake vortex during roll-up with 4HVS interaction through modification of the high-lift configuration [30].

The H4VS studies showed that it was possible to attenuate the fully rolled up wake vortices and provided a detailed explanation of their dissipation. Although they successfully confirmed the interaction effects, initial vortex locations were limited to the same horizontal plane, and the vertical distance between the vortices was not considered. However, the two pairs of wake vortices generated by different aircraft have different vertical positions because of the descent motion. Hence, the vertically arranged two pairs of wake vortices depicted in Fig. 1-6 should be examined. Here, the surrounding streamline patterns are divided into the three regions separated by the bold lines, which consist of the inner circulation region, recirculation region, and outer region. The rotation of the recirculation region induces a vertical approach of the two vortex pairs (blue arrows). While the vertical distance of the H4VS increases, its instability influenced by the strain field of the

other vortices also depends on their distances, which in turn affect its transport and decay characteristics. Therefore, two vortex pairs with different vertical positions should be studied separately.

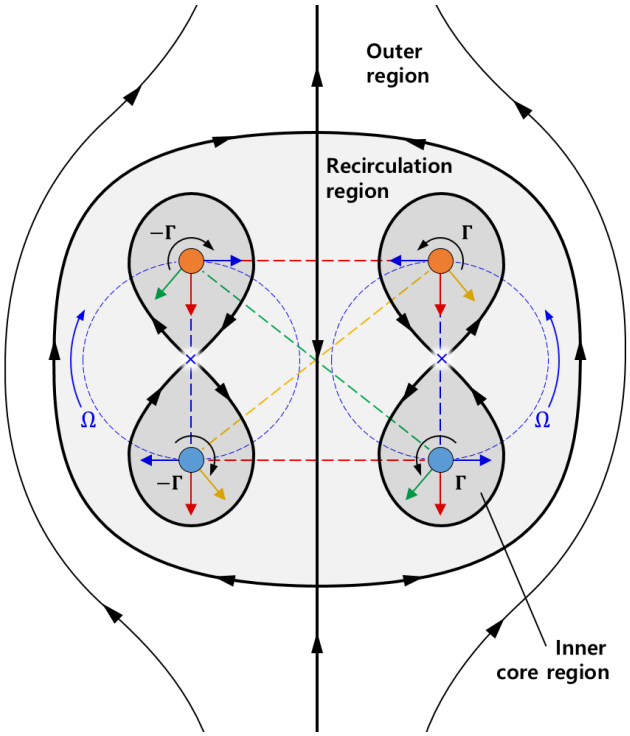

Fig. 1-6 Streamline patterns of the vertically aligned two wake vortex pairs (black lines) and initial vortex transport by mutual induction (colored lines).

1.3 Outline of Dissertation

This study focuses on the transport and decay characteristic processes involving interactions between the wake vortex pairs formed by the preceding and following aircraft. This is the first work to investigate the effect of the wake vortex formed by the preceding aircraft on the vortex formed by the following aircraft. The decay processes were analyzed by selecting suitable initial conditions that took into account the high altitude of the following aircraft and the descent of the preceding wake vortices. To consider possible vortex interactions, their parameters were defined based on the commercial aircraft size and routes. Atmospheric turbulence conditions were applied to LES to account for the vortex core instability and non-linear decay known as the Crow instability. The obtained results were analyzed to identify the decay characteristic processes that induce the rapid dissipation of the wake vortices and their conditions. If the interaction between wake vortex pairs induces a rapid dissipation, it may be possible to adjust the take-off separation time and, therefore, increase the airport capacity.

This paper is organized as follows. Details of numerical simulations are outlined in section 2. The time delayed wake vortex interaction analysis is described in section 3. In section 4 vertical four vortex system is described and the obtained results are presented. The transport and decay characteristics of wake vortices are classified by discussing their interaction mechanism and dissipation effects. Finally, the applicability limits of rapid vortex dissipation processes are determined, and the conclusions of this study are drawn in section 5.

Chapter 2. Numerical simulations

The numerical V4VS simulation procedure conducted under atmospheric turbulence conditions was as follows. 1) LES was performed until the V4VS was completely dissipated. 2) Stochastic noise generation and radiation (SNGR) and forcing methods were used to generate a background turbulence field. 3) For vortex initialization, the velocity profile calculated by the vortex model was superimposed on the turbulence field. 4) The vortex parameters were calculated to quantify the V4VS dissipation using a core-line identification method.

The overall flow of the simulation is described in the Fig. 2-1. First, we set the computational domain and generate the grid. Since the behavior of wake vortices varies depending on the atmospheric conditions, it is essential to make atmospheric background turbulence under specific conditions. In order to create a flow field with eddy dissipation rate similar to a real atmospheric condition, stochastic noise generation and radiation (SNGR) and forcing technique are used. In this process, the LES simulation continues and the statistical steady-state isotropic turbulence is generated as background turbulence. After the background turbulence is generated, a pair of counter-rotating vortices with same magnitude of circulation is modeled and added to the flow field. Then LES simulation is continuously performed to observe the behavior of vortices over time. When interpreting the behavior of a pair of vortices alone, the LES simulation is performed for the desired time and the procedure goes to the post-processing. On the other hand, when observing the interaction between two pairs of wake vortices, another pair of vortices is added to the flow field during the LES simulation. After that, the LES simulation is conducted for the required time (dotted line in Fig.

2-1). In the next section, each procedure is being explained in more detail starting from governing equations and numerical methods.

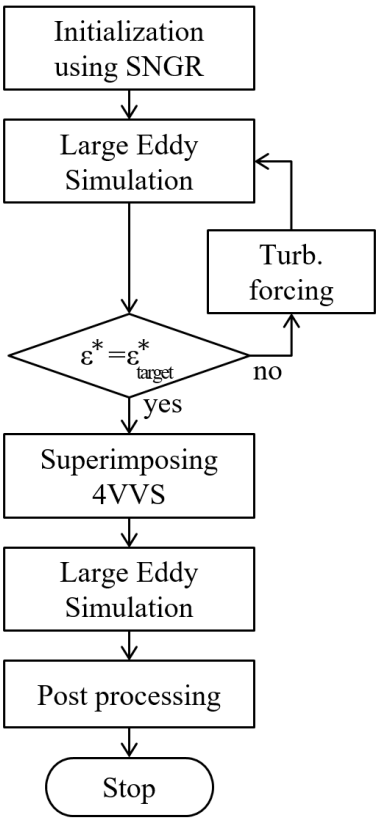

Fig. 2-1 Flow chart for wake vortex analysis

2.1 Large eddy simulation and computational domain

LES is based on the observation that the small turbulent structures are more universal in character than the large eddies. Therefore, the idea is to compute the contributions of the large, energy-carrying structures to momentum and energy transfer and to model the effects of the small structures, which are not resolved by the numerical scheme. Due to the more homogeneous and universal character of the small scales, we may expect that the so called subgrid-scale models can be kept much simpler than the turbulence models for the RANS equations.

In the case of a compressible Newtonian fluid, the Navier-Stokes equations read using tensor notation in the absence of source terms in coordinate invariant formulation as

$$\begin{aligned} \frac{\partial \rho}{\partial t} + \frac{\partial}{\partial x_i}(\rho v_i) &= 0, \\ \frac{\partial}{\partial t}(\rho v_i) + \frac{\partial}{\partial x_j}(\rho v_j v_i) &= -\frac{\partial p}{\partial x_i} + \frac{\partial \tau_{ij}}{\partial x_j}, \\ \frac{\partial}{\partial t}(\rho E) + \frac{\partial}{\partial x_j}(\rho v_j H) &= \frac{\partial}{\partial x_j}(v_j \tau_{ij}) + \frac{\partial}{\partial x_j}\left(k \frac{\partial T}{\partial x_j}\right) \end{aligned} \tag{2.1}$$

where v_i denotes a velocity component ($\vec{v} = [v_1, v_2, v_3]^{\mathrm{T}}$), and x_i stands for a coordinate direction, respectively.

The components of the viscous stress tensor τ_{ij} in Eq. (2.1) are defined as

$$\tau_{ij} = 2\mu S_{ij} + \lambda \frac{\partial v_k}{\partial x_k}\delta_{ij} = 2\mu S_{ij} - \left(\frac{2\mu}{3}\right)\frac{\partial v_k}{\partial x_k}\delta_{ij}, \tag{2.2}$$

where we utilized the Stokes's hypothesis. The second term in Eq. (7.2), that is, $\partial v_{\mathrm{k}} / \partial x_{\mathrm{k}}$, which corresponds to the divergence of the velocity.

The components of the strain-rate tensor are given by

$$S_{ij} = \frac{1}{2}\left(\frac{\partial v_i}{\partial x_j} + \frac{\partial v_j}{\partial x_i}\right). \tag{2.3}$$

In this connection, let us also define the rotation-rate tensor (antisymmetric part of the velocity gradient tensor) with the following components.

$$\Omega_{ij} = \frac{1}{2}\left(\frac{\partial v_i}{\partial x_j} - \frac{\partial v_j}{\partial x_i}\right). \tag{2.4}$$

The total energy E and the total enthalpy H in Eq. (2.1) are readily obtained from the formulas.

$$E = e + \frac{1}{2}v_i v_i, \qquad H = h + \frac{1}{2}v_i v_i = E + \frac{p}{\rho} \tag{2.5}$$

2.1.1 Reynolds averaging

The approximate treatment of turbulent flows is based on the decomposition of the flow variables into a mean and a fluctuating part. The governing equations are then solved for the mean values, which are the most interesting for engineering applications. Thus, the velocity components and the pressure in Eq. (2.1) are substituted [37]

$$v_i = \overline{v_i} + v_i', \qquad p = \bar{p} + p', \tag{2.6}$$

where the mean value is denoted by a bar and the turbulent fluctuations by a prime. The mean values are obtained by an averaging procedure.

The average of the fluctuating part is zero, that is, $\overline{v_i'} = 0$. However, it can be easily seen that $\overline{v_i' v_i'} \neq 0$. The same is true for $\overline{v_i' v_j'}$, if both turbulent velocity components are correlated.

2.1.2 Favre (mass) averaging

In cases where the density is not constant, it is advisable to apply the density (mass) weighted or Favre decomposition to certain quantities in Eq. (2.1) instead of Reynolds averaging. Otherwise, the averaged governing equations would become considerably more complicated due to additional correlations involving density fluctuations. The most convenient way is to employ Reynolds averaging for density and pressure, and Favre averaging for other variables such as velocity, internal energy, enthalpy, and temperature. Favre averaged quantities, for example, the velocity components, are obtained from the relation

$$\widetilde{v_i} = \frac{1}{\bar{\rho}} \lim_{T\to\infty} \frac{1}{T} \int_t^{t+T} \rho\, v_i \mathrm{d}t, \tag{2.7}$$

where $\bar{\rho}$ denotes the Reynolds-averaged density. Hence, the Favre decomposition reads

$$v_i = \widetilde{v_i} + v_i'', \tag{2.8}$$

where $\widetilde{v_i}$ represents the mean value and v_i'' the fluctuating part of the velocity v_i. Again, the average of the fluctuating part is zero, that is, $\widetilde{v_i''} = 0$. Furthermore, the average of the product of two fluctuating quantities is not zero, if the quantities are correlated. Hence, for example, $\widetilde{v_i'' v_i''} \neq 0$ and in general $\widetilde{v_i'' v_j''} \neq 0$.

The following relationships can be derived for a mix between Favre and Reynolds averaging

$$\widetilde{\rho v_i} = \bar{\rho}\widetilde{v_i}, \qquad \overline{\rho v_i''} = 0, \qquad \text{but } \overline{v_i''} \neq 0. \tag{2.9}$$

2.1.3 Favre- and Reynolds-Averaged Navier-Stokes Equations

In turbulence modeling, it is quite common to assume that Morkovin's hypothesis is valid. It states that the turbulent structure of a boundary layer is not notably influenced by density fluctuations if $\rho' \ll \bar{\rho}$. This is generally true for wall-bounded flows up to a Mach number of about five. However, in the case of hypersonic flows or for compressible free shear layers, density fluctuations have to be accounted for. The same holds also for flows with combustion or with significant heat transfer.

Application of the Reynolds averaging to density and pressure, and of the Favre averaging Eq. (2.7) to the remaining flow variables in the compressible Navier-Stokes equations (2.1) yields

$$\begin{aligned}
&\frac{\partial \bar{\rho}}{\partial t} + \frac{\partial}{\partial x_i}(\bar{\rho}\tilde{v}_i) = 0 \\
&\frac{\partial}{\partial t}(\bar{\rho}\tilde{v}_i) + \frac{\partial}{\partial x_j}(\bar{\rho}\tilde{v}_j\tilde{v}_i) = -\frac{\partial \bar{p}}{\partial x_i} + \frac{\partial}{\partial x_j}(\tilde{\tau}_{ij} - \bar{\rho}\widetilde{v_i''v_j''}) \\
&\frac{\partial}{\partial t}(\bar{\rho}\tilde{E}) + \frac{\partial}{\partial x_j}(\bar{\rho}\tilde{v}_j\tilde{H}) = \frac{\partial}{\partial x_j}\left(k\frac{\partial \tilde{T}}{\partial x_j} - \bar{\rho}\widetilde{v_j''h''} + \widetilde{\tau_{ij}v_i''} - \bar{\rho}\widetilde{v_j''K}\right) \\
&\qquad + \frac{\partial}{\partial x_j}\left[\tilde{v}_i\left(\tilde{\tau}_{ij} - \bar{\rho}\widetilde{v_i''v_j''}\right)\right]
\end{aligned} \tag{2.10}$$

These are the Favre- and Reynolds-averaged Navier-Stokes equations. In an analogy to the Reynolds averaging, the viscous stress tensor in the momentum (and energy) equation becomes extended by the Favre-averaged Reynolds-stress tensor, that is,

$$\tau_{ij}^{F} = -\bar{\rho}\widetilde{v_i''v_j''}. \tag{2.11}$$

The components of the laminar (molecular) viscous stress tensor $\tilde{\tau}_{ij}$ are

evaluated by Eq. (7.2) using Favre-averaged velocity components.

If we employ the definition of the Favre-averaged turbulent kinetic energy, that is,

$$\bar{\rho}\tilde{K} = \frac{1}{2}\bar{\rho}\widetilde{v_i''v_i''}, \tag{2.12}$$

we can express the total energy in Eq. (2.10) as

$$\bar{\rho}\tilde{E} = \bar{\rho}\tilde{e} + \frac{1}{2}\bar{\rho}\tilde{v}_i\tilde{v}_i + \frac{1}{2}\bar{\rho}\widetilde{v_i''v_i''} = \bar{\rho}\tilde{e} + \frac{1}{2}\bar{\rho}\tilde{v}_i\tilde{v}_i + \bar{\rho}\tilde{K} \tag{2.13}$$

The total enthalpy is defined as

$$\bar{\rho}\tilde{H} = \bar{\rho}\tilde{h} + \frac{1}{2}\bar{\rho}\tilde{v}_i\tilde{v}_i + \frac{1}{2}\bar{\rho}\widetilde{v_i''v_i''} = \bar{\rho}\tilde{h} + \frac{1}{2}\bar{\rho}\tilde{v}_i\tilde{v}_i + \bar{\rho}\tilde{K} \tag{2.14}$$

The individual parts of the Favre- and Reynolds-averaged Navier-Stokes equations (2.10) have the following physical meaning

$\frac{\partial}{\partial x_j}\left(k\frac{\partial \bar{T}}{\partial x_j}\right)$ – molecular diffusion of heat,

$\frac{\partial}{\partial x_j}\left(\bar{\rho}\widetilde{v_j''h''}\right)$ – turbulent transport of heat,

$\frac{\partial}{\partial x_j}\left(\widetilde{\tau_{ij}v_i''}\right)$ – molecular diffusion of $\tilde{K}$,

$\frac{\partial}{\partial x_j}\left(\bar{\rho}\widetilde{v_j''K}\right)$ – turbulent transport of $\tilde{K}$,

$\frac{\partial}{\partial x_j}\left(\tilde{v}_i\tilde{\tau}_{ij}\right)$– work done by the molecular stresses,

$\frac{\partial}{\partial x_j}\left(\tilde{v}_i\tau_{ij}^F\right)$– work done by the Favre-averaged Reynolds stresses.

The molecular diffusion and turbulent transport of $\tilde{K}$ are very often neglected. This is a valid approximation for transonic and supersonic flows. In order to close the Favre and Reynolds-averaged equations (2.10), we also have to supply six components of the Favre-averaged Reynolds-stress tensor (Eq. (2.11)) and three components of the turbulent heat-flux vector.

2.1.4 Spatial filtering

LES is based on a spatial filtering operation, which decomposes any flow variable U into a filtered (large-scale, resolved) part $\overline{U}$ and into a sub-filter (unresolved) part U', that is,

$$U = \overline{U} + U' \tag{2.15}$$

The filtered variable at the location $\overrightarrow{r_0}$ in space is defined as

$$\overline{U}(\vec{r}_0, t) = \int_D U(\vec{r}, t)\, G(\vec{r}_0, \vec{r}, \Delta)\mathrm{d}\vec{r}, \tag{2.16}$$

where Ω denotes the entire flow domain, G represents the filter function, and $\vec{r}$ is the position vector, respectively. The filter function determines the structure and size of the small scales. The filter function depends on the difference $\vec{r}_0 - \vec{r}$ and on the filter width $\Delta = (\Delta_1\, \Delta_2\, \Delta_3)^{1/3}$, with Δ_i being the filter width in the *i*th spatial coordinate.

2.1.5 Filtered governing equations

The spatial filtering has to be applied to the Navier-Stokes equations in order to remove the small turbulent scales. The filter width Δ as well as the filter function are considered as free parameters. In fact, the governing equations are usually not explicitly filtered. Instead, the grid as well as the discretization errors are assumed to define the filter G.

If LES is to be applied to compressible flows, we have to apply Favre averaging together with the spatial filtering to Eq. (2.1). Otherwise, the filtered Navier-Stokes equations would contain products between density and other variables like velocity or temperature. Thus, the velocity components, the energy and the temperature in Eq. (2.1) is decomposed

$$U = \widetilde{U} + U''. \tag{2.17}$$

The filtered variable at the location $\overrightarrow{r_0}$ in space is given by

$$\widetilde{U}(\vec{r}_0, t) = \frac{\overline{\rho U}}{\bar{\rho}} = \frac{1}{\bar{\rho}} \int_D \rho(\vec{r}, t) U(\vec{r}, t)\, G(\vec{r}_0, \vec{r}, \Delta) \mathrm{d}\vec{r}, \tag{2.18}$$

where the bar denotes filtering according to the Eq. (2.16). The Favre-filtered Navier-Stokes equations (2.1) read

$$\begin{aligned}
&\frac{\partial \bar{\rho}}{\partial t} + \frac{\partial}{\partial x_j}\left(\bar{\rho}\tilde{v}_j\right) = 0, \\
&\frac{\partial \bar{\rho}\tilde{v}_i}{\partial t} + \frac{\partial\left(\bar{\rho}\tilde{v}_j\tilde{v}_i\right)}{\partial x_j} + \frac{\partial \bar{p}}{\partial x_i} - \frac{\partial \hat{\sigma}_{ij}}{\partial x_j} = -\frac{\partial \tau_{ij}^{SF}}{\partial x_j} + \frac{\partial}{\partial x_j}\left(\bar{\sigma}_{ij} - \hat{\sigma}_{ij}\right), \\
&\frac{\partial \bar{\rho}\tilde{e}}{\partial t} + \frac{\partial\left(\bar{\rho}\tilde{v}_j\tilde{e}\right)}{\partial x_j} + \frac{\partial \hat{q}}{\partial x_j} + \bar{p}\tilde{S}_{kk} - \hat{\sigma}_{ij}\tilde{S}_{ij} = -\mathcal{A} - \mathcal{B} - \mathcal{C} + \mathcal{D}
\end{aligned} \tag{2.19}$$

with the terms

$\mathcal{A} = \frac{\partial}{\partial x_j}\left[\bar{\rho}\left(\widetilde{v_j' e} - \tilde{v}_j \tilde{e}\right)\right]$ – divergence of subgrid-scale heat flux,

$\mathcal{B} = \frac{\partial}{\partial x_j}\left[\bar{q}_j - \hat{q}_j\right]$ – divergence of SGS heat diffusion,

$\mathcal{C} = [\overline{pS_{kk}} - \bar{p}\tilde{S}_{kk}]$ – SGS pressure-dilatation,

$\mathcal{D} = [\overline{\sigma_{\iota J} S_{\iota J}} - \hat{\sigma}_{ij}\tilde{S}_{ij}]$ – SGS viscous dissipation

and

$$\begin{gathered}
\bar{\sigma}_{ij} = \overline{2\mu S_{\iota J}} + \overline{\left(\mu_{\mathrm{B}} - \frac{2\mu}{3}\right)\delta_{\iota J} S_{kk}}, \\
\hat{\sigma}_{ij} = 2\tilde{\mu}\tilde{S}_{ij} + \left(\tilde{\mu}_{\mathrm{B}} - \frac{2\mu}{3}\right)\delta_{ij}\tilde{S}_{kk}, \\
\tilde{S}_{ij} = \frac{1}{2}\left(\frac{\partial \tilde{v}_i}{\partial x_j} + \frac{\partial \tilde{v}_j}{\partial x_i}\right), \\
\bar{q}_j = -k\frac{\overline{\partial T}}{\partial x_j}, \quad \tilde{q}_j = -\tilde{k}\frac{\partial \tilde{T}}{\partial x_j}.
\end{gathered} \tag{2.20}$$

In Eqs. (2.19)– (2.20), e denotes internal energy per unit mass, $\widetilde{S_{\iota J}}$ is the Favre-filtered strain-rate tensor, and $\tau_{ij}^{SF} = \bar{\rho}(\widetilde{v_\iota v_J} - \tilde{v}_\iota \tilde{v}_J)$ represents the Favre-averaged subgrid-scale stress. Furthermore, μ, μ_{B}, and k stand for the molecular viscosity, the bulk viscosity, and for the thermal conductivity, respectively. Finally, $\tilde{\mu}$, $\tilde{\mu}_{\mathrm{B}}$, and $\tilde{k}$ are the corresponding values at the filtered temperature $\tilde{T}$.

The right-hand side of Eq. (2.19) contains terms which have to be modeled. In the momentum equation, the SGS stresses τ_{ij}^{SF} are approximated, but the second term, that is, $(\bar{\sigma}_{ij} - \hat{\sigma}_{ij})$ is usually neglected. In the energy equation, term A can be expressed through the SGS stresses, term B can be neglected, and terms C and D can be modeled.

2.1.6 Subgrid-scale modeling

The main task of a subgrid-scale model is to simulate energy transfer between the large and the subgrid scales. On the average, the energy is transported from the large scales to the small ones (turbulent cascade process). Therefore, a subgrid-scale model has to provide means of adequate energy dissipation. However, in some instances the energy also flows from the small to the large scales—a process called backscatter. Clearly, the model should account for this effect as well.

The Smagorinsky model, which forms the basis of all subgrid-scale models, approaches which model the SGS tensor τ_{ij}^{S} explicitly. A necessary condition is then that the numerical dissipation caused by the spatial discretization scheme must be much lower than the subgrid-scale dissipation. The majority of explicit SGS models is based on the eddy-viscosity concept.

Eddy-viscosity models

These explicit models are able to represent the global dissipative effects of the small scales, but they cannot reproduce the local details of the energy exchange.

The components of the Favre-averaged SGS stress tensor are approximated as

$$\tau_{ij}^{SF} - \frac{\delta_{ij}}{3}\tau_{kk}^{SF} = -2\bar{\rho}\nu_T\,\tilde{S}_{ij} + \left(\frac{2\bar{\rho}\nu_T}{3}\right)\frac{\partial\hat{\sigma}_k}{\partial x_k}\delta_{ij}. \tag{2.21}$$

The components of the strain-rate tensor $\tilde{S}_{ij}$ are given in Eq. (2.20). The eddy viscosity ν_T is in general evaluated from algebraic relations in order to save numerical costs. The isotropic part of the SGS stresses (τ_{kk}^{SF}) can

either be added to the filtered pressure, modeled, or neglected.

Smagorinsky SGSmodel

The Smagorinsky model [38] is based on the equilibrium hypothesis which implies that the small scales dissipate entirely and instantaneously all the energy they receive from the large scales. The algebraic model assumes the form

$$\nu_T = (C_s\Delta)^2\left|\widetilde{S_{ij}}\right| \tag{2.22}$$

where $\left|\tilde{S}_{ij}\right| = \left(2\tilde{S}_{ij}\tilde{S}_{ij}\right)^{1/2}$ is the magnitude of the strain-rate tensor and $\mathrm{C_s}$ denotes the Smagorinsky constant. The Smagorinsky constant depends on the type of the flow and is selected to be 0.16 [39]. The rotational corrected Smagorinsky model was used for the wake vortex problem. The subgrid eddy viscosity for momentum is modified by the Richardson numbers, Ri_{r}, factor of $(1 - 1.5Ri_{\mathrm{r}})^{1/2}$ [39].The filter width Δ in Eq. (2.22) is based on the minimal resolvable scale which is the twice the average grid size, that is, $\Delta = 2(\Delta x_1\,\Delta x_2\,\Delta x_3)^{1/3}$.

2.1.7 Numerical scheme

Inviscid flux was discretized based on Roe's flux difference splitting method utilizing the primitive variables interpolated by a higher-order monotonic upwind scheme for conservation laws [40]. Viscous flux was evaluated by the second-order central scheme, and time integration was performed using the explicit fourth-order Runge–Kutta method. The LES code was verified by a previous study on wake vortices [40]. The details for numerical simulations are summarized in Table 2.1.

Table 2.1 Flow simulation methods

Inviscid flux	Roe's flux difference splitting
Viscous flux	2^{nd}-order central difference
time integration	4^{th}-order Runge-Kutta
Turbulence model	LES (Smagorinsky model)

Fourth(fifth)-order compact upwind TVD scheme

This scheme can be explained by using the one-dimensional scalar conservation Eq. (2.23).

$$\frac{\partial q}{\partial t} + \frac{\partial f(a,q)}{\partial x} = 0, \tag{2.23}$$

Where $f(a,q)$ is a function of the unknown variable q and the characteristic speed $a = \partial f/\partial q$. The semi-discrete conservation form of equation Eq. (2.23) with respect to x at a point l in space can be written as

$$\frac{\partial q}{\partial t} = \frac{\left(\hat{f}_{l+1/2} - \hat{f}_{l-1/2}\right)}{\Delta x} = 0, \tag{2.24}$$

and in the existing second(third)-order upwind finite-difference scheme the numerical flux $\hat{f}_{l+1/2}$ is calculated by

$$\hat{f}_{l+1/2} = \frac{1}{2}[f(a_{l+1/2}, q_l) + f(a_{l+1/2}, q_{l+1})] - \frac{1}{2}(\Delta f^{+}_{l+1/2} - \Delta f^{-}_{l+1/2})$$
$$+ \frac{1-\phi}{4}\Delta \bar{f}^{+}_{l-1/2} + \frac{1+\phi}{4}\Delta \tilde{f}^{+}_{l+1/2} - \frac{1+\phi}{4}\Delta \bar{f}^{+}_{l+1/2} - \frac{1-\phi}{4}\Delta \tilde{f}^{+}_{l+3/2}, \tag{2.25}$$
$$\Delta f^{\pm}_{j+1/2} = f^{\pm}(a_{l+1/2}, q_{j+1}) - f^{\pm}(a_{l+1/2}, q_j) \cong a^{\pm}_{l+1/2}(q_{j+1} - q_j)$$
$$a^{\pm} = (a \pm |a|)/2.$$

The first term on the right-hand side of Eq. (2.25) is the form of the second-order central-difference scheme, and the second term is the correction term which converts the central-difference scheme into the first-order upwind-difference scheme. The remaining terms transform the scheme into the second-order upwind-difference scheme for the smoothly varying monotone function f and, especially for $\phi = 1/3$, into the third-order upwind-difference scheme.

Firstly, the numerical flux $\hat{f}_{l+1/2}$ of the third-order upwind-difference scheme Eq. (2.25) can be rewritten as

$$\hat{f}^{(3)}_{l+1/2} = h(q_l, q_{l+1}) + \frac{1}{6}\left(\Delta f^{+}_{l-1/2} + 2\Delta f^{+}_{l+1/2} - 2\Delta f^{-}_{l+1/2} - \Delta f^{-}_{l+3/2}\right), \tag{2.26}$$

where

$$h(q_l, q_{l+1}) = \frac{1}{2}[f(q_l) + f(q_{l+1})] + \frac{1}{2}\left[\Delta f^{+}_{l+1/2} - \Delta f^{-}_{l+1/2}\right]. \tag{2.27}$$

On the other hand, the numerical flux of the fourth(fifth)-order upwind-difference scheme also can be derived as

$$\hat{f}^{(4)}_{l+1/2} = h(q_l, q_{l+1}) + \frac{1}{12}[(0-12\phi)\Delta f^{+}_{l-3/2} + (1+36\phi)\Delta f^{+}_{l-1/2}$$
$$(6-36\phi)\Delta f^{+}_{l+1/2} + (-1+12\phi)\Delta f^{+}_{l+3/2} + (1-12\phi)\Delta f^{-}_{l-1/2} \quad (2.28)$$
$$(-6+36\phi)\Delta f^{-}_{l+1/2} + (-1-36\phi)\Delta f^{-}_{l+3/2} + (0+12\phi)\Delta f^{-}_{l+5/2}].$$

The accuracy of this expression only becomes fifth order for $\phi = 1/30$.

Now, we define a difference in flux in order to compose a compact form of Eq. (2.28), i.e.

$$Df_{l+1/2} \equiv \hat{f}^{(4)}_{l+1/2} - f^{(3)}_{l+1/2} \quad (2.29)$$

and also

$$\Delta^2 f_l \equiv \Delta f_{l+1/2} - \Delta f_{l-1/2},$$
$$\Delta^3 f_{l+1/2} \equiv \Delta^2 f_{l+1} - \Delta^2 f_l = \Delta f_{l-1/2} - 2\Delta f_{l+1/2} + \Delta f_{l+3/2}. \quad (2.30)$$

By using these definitions and Eq. (2.26) and Eq. (2.28), Df can be written as

$$Df_{l+1/2} = \frac{1}{12}[-12\phi\Delta^3 f^{+}_{l-1/2} - (1-12\phi)\Delta^3 f^{+}_{l+1/2}$$
$$(1-12\phi)\Delta^3 f^{-}_{l+1/2} + 12\phi\Delta^3 f^{-}_{l+3/2}]. \quad (2.31)$$

Therefore, Eq. (2.28) can be rewritten in a compact form, which is quite similar to the third-order form of Eq. (2.26), as

$$\hat{f}^{(4)}_{l+1/2} = \hat{f}^{(3)}_{l+1/2} + Df_{l+1/2}$$
$$= h(q_l, q_{l+1}) + \frac{1}{6}\left(\Delta^* f^{+}_{l-1/2} + 2\Delta^* f^{+}_{l+1/2} - 2\Delta^* f^{-}_{l+1/2} - \Delta^* f^{-}_{l+3/2}\right), \quad (2.32)$$

where

$$\Delta^* f^{+}_{l-1/2} = \Delta f^{+}_{l-1/2} - 12\phi\Delta^3 f^{+}_{l-1/2}/2,$$
$$\Delta^* f^{+}_{l+1/2} = \Delta f^{+}_{l+1/2} - (1-12\phi)\Delta^3 f^{+}_{l+1/2}/4, \quad (2.33)$$
$$\Delta^* f^{-}_{l+1/2} = \Delta f^{-}_{l+1/2} - (1-12\phi)\Delta^3 f^{-}_{l+1/2}/4,$$

$$\Delta^* f^-_{l+3/2} = \Delta f^-_{l+3/2} - 12\phi\Delta^3 f^-_{l+3/2}/2.$$

If the additional terms of A3f in Eq. (2.33) are omitted, then Eq. (2.32) is reduced to the third-order form Eq. (2.30). And Eq. (2.32) becomes the fourth-order central-difference scheme for $\phi = 0$, and the 5-point upwind-difference scheme for $\phi = 1/12$. The accuracy of Eq. (2.32) is, in general, fourth order and only becomes fifth order for $\phi = 1/30$.

Rewriting Eq. (2.32) as an upwind TVD scheme by applying the flux limiters, we get

$$\hat{f}^{(4)}_{l+1/2} = h(q_l, q_{l+1})\,\frac{1}{6}\left(\Delta^*\bar{f}^+_{l-1/2} + 2\Delta^*\tilde{f}^+_{l+1/2} - 2\Delta^*\bar{f}^-_{l+1/2} - \Delta^*\tilde{f}^-_{l+3/2}\right), \quad (2.34)$$

where

$$\begin{aligned}
\Delta^*\bar{f}^+_{l-1/2} &= \text{minmod}[\Delta^* f^+_{l-1/2}, b\Delta^* f^+_{l+1/2}],\\
\Delta^*\tilde{f}^+_{l+1/2} &= \text{minmod}[\Delta^* f^+_{l+1/2}, b\Delta^* f^+_{l-1/2}],\\
\Delta^*\bar{f}^-_{l+1/2} &= \text{minmod}[\Delta^* f^-_{l+1/2}, b\Delta^* f^-_{l+3/2}],\\
\Delta^*\tilde{f}^-_{l+3/2} &= \text{minmod}[\Delta^* f^-_{l+3/2}, b\Delta^* f^-_{l+1/2}],
\end{aligned} \quad (2.35)$$

Although the accuracy of Eq. (2.32) is only fifth-order for $\phi = 1/30$ mathematically, the accuracy of the computational results seems to be altered gradually according to the value of ϕ. As a matter of fact, the calculated results for $\phi = 1/36$ were almost the same as those for $\phi = 1/30$. Therefore, if we set $\phi = 1/36$, then Eq. (2.33) can be expressed by the single form

$$\Delta^* f^\pm_{j-1/2} = \Delta f^\pm_{j+1/2} - \frac{1}{6}\Delta^3\bar{f}^\pm_{j+1/2}, \quad (2.36)$$

and the third-order flux difference $\Delta^3\bar{f}$ is

$$\Delta^3\bar{f}_{j+1/2} = \Delta\bar{f}_{j-1/2} - \Delta\bar{f}_{j+1/2} + \Delta\bar{f}_{j+3/2}, \quad (2.37)$$

where

$$\Delta\bar{f}_{j-1/2} = \text{minmod}[\Delta f_{j-1/2}, b_1\Delta f_{j+1/2}, b_1\Delta f_{j+3/2}],$$
$$\Delta\bar{f}_{j+1/2} = \text{minmod}[\Delta f_{j+1/2}, b_1\Delta f_{j+3/2}, b_1\Delta f_{j-1/2}], \quad (2.38)$$
$$\Delta\bar{f}_{j+3/2} = \text{minmod}[\Delta f_{j+3/2}, b_1\Delta f_{j-1/2}, b_1\Delta f_{j+1/2}],$$

and

$$\text{minmod}[x, y, z] = \text{sign}(x)\max[0, \min\{|x|, y\,\text{sign}(x), z\,\text{sign}(x)\}]. \quad (2.39)$$

2.1.8 Computational grid

The computational domain in the longitudinal direction, parallel to the aircraft flight path, was 8.5 times the vortex spacing to observe the most amplified wavelength (MAW) of Crow instability. The lateral and vertical domains were set equal to the longitudinal direction. The overall domain was discretized using a 400×400×400 grid. In order to accurately describe the isotropy characteristic of small eddies, the grid size is made smaller than the integral length scale, L_{11}. The integral length scale can be calculated by Eq. (2.40) where the domain averaged value is denoted by $< >$. Grid spacing was selected to include at least three grids within the core radius ($\Delta < r_c/3$) [13]. Periodic boundary conditions are applied for all directions. The influence of the boundary conditions is negligible because the vertical computational domain is eight times as long as the initial spacing of the wake vortices. Moreover, it is advantageous to simulate the behavior of wake vortices for a long time by applying the periodic boundary conditions.

$$L_{11} = \int_0^\infty < u(x)u(x+r) > / < u^2 > dr \qquad (2.40)$$

2.2 Background turbulence field

It is necessary to generate an initial background turbulence in order to see the characteristics of the wake vortices according to the atmospheric conditions. Background turbulence causes perturbation along the core line of the initial wave vortex. The vortex then behaves and this perturbation grows under the influence of the strain field of the other vortex. It is called instability that the core line is distorted by this growth of perturbation. Therefore, it is important to create a background turbulence field that matches the actual atmospheric conditions. The turbulence field was generated using the SNGR [41] model and corrected by an artificial external forcing method [10] considering the atmosphere around the runway. LES was conducted by applying forcing to the low wavenumber flow components with a fixed amplitude. This process was repeated until a statistically converged state was reached. The dissipation rate (ε) of the turbulence field was $0.0006\ \mathrm{m}^2/\mathrm{s}^3$, and the integral length scale (L_{11}) was $57.5\ m$.

2.2.1 Stochastic Noise Generation and Radiation (SNGR)

First, SNGR model [41] was used to generate random turbulence. In the model, the random velocity field $\boldsymbol{u_t(x)}$ is defined as a finite sum of discrete Fourier modes as in Eq. (2.41):

$$\boldsymbol{u_t(x)} = 2\sum_{n=1}^{N} \tilde{u}_{tn}\cos(\boldsymbol{k_n}\cdot\boldsymbol{x} + \Psi_n)\boldsymbol{\sigma_n} \qquad (2.41)$$

where $\boldsymbol{x}$ is a position vector, and $\tilde{u}_{tn}$, Ψ_n, $\boldsymbol{\sigma_n}$ are the nth mode components of the wave vector $\boldsymbol{k_n}$, indicating the amplitude, phase, and direction, respectively. In the case of random turbulence generated by SNGR, it can be seen that the velocity distribution is symmetrical about the middle point as shown in Fig. 2-2.

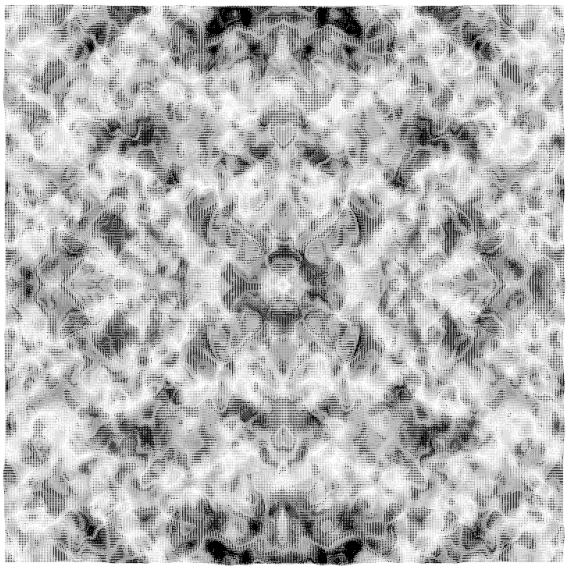

Fig. 2-2 Spatial distribution of the turbulent velocity field generated by SNGR; velocity vector is plotted in the x-z plane

2.2.2 Artificial External Forcing

Although SNGR generate mathematically homogeneous isotropic turbulence, but it is different from actual atmospheric turbulence. Therefore, for the more accurate atmospheric turbulence simulation, a method of artificially adding external force to the low-frequency wave component of the flow field has been adopted [42]. Three-dimensional fast Fourier transform (FFT) of the flow field is conducted at each time step, and then a fixed amplitude f is added to the wave number whose magnitude is less than 3.0 [10][13]. Finally, the inverse fast Fourier transform (inverse FFT) was performed (Fig. 2-3). Since the size of computational domain is not same for x,y, and z direction, the actual wavelength along the longitudinal, transverse and vertical directions can be calculated differently. In this case, the components in the longest direction are normalized with respect to the shortest direction, so that energy is not added to waves of different sizes according to the directions, but added to waves of the same size for each direction.

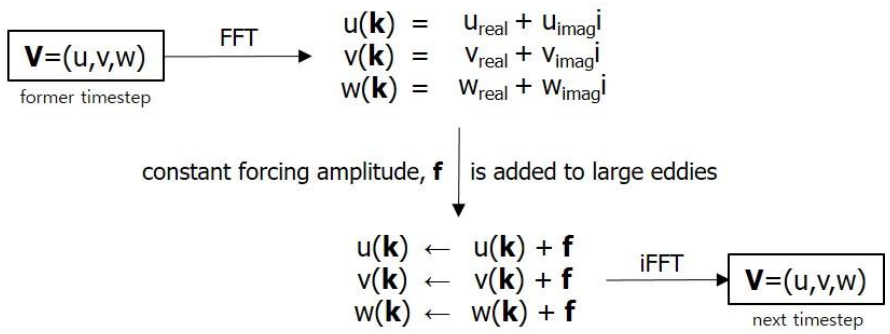

Fig. 2-3 Forcing technique to make background turbulence field

Since the low-frequency component exhibits the longest wavelength characteristic, adding energy here can be regarded as adding the flow components of large eddies from a physical point of view. These added components transfer energy to the small eddies according to the energy cascade of the turbulence, which eventually leads to turbulent dissipation by viscosity. Therefore, the turbulent field reaches a statistical steady state when the energy added and the energy dissipated by the viscosity become equal. Fig. 2-4 shows that the turbulent flow field enters the statistical steady state after about 400 seconds. At this time, if the integral length scale L_{11} according to Eq. (2.40) is calculated, it is confirmed that L_{11} = 57.5 m. In addition, isotropy parameters that are defined as Eq. (2.42) and Eq. (2.43), both I_1 and I_2

$$I_1 = [\langle u^2 \rangle / \langle v^2 \rangle]^{0.5} \quad (2.42)$$

$$\boldsymbol{I_2 = [\langle w^2 \rangle / \langle v^2 \rangle]^{0.5}} \quad (2.43)$$

oscillate around 1. Since the isotropic parameters in the isotropic turbulence field are 1, it can be confirmed that the generated turbulence field is the isotropic turbulence field. The background turbulence field is generated as shown in Fig. 2-5 with various size of eddies.

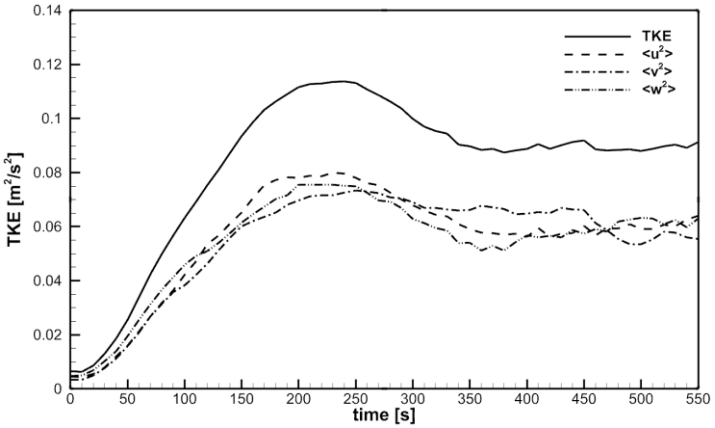

Fig. 2-4 Time evolution of turbulent kinetic energy (TKE) before vortices are injected

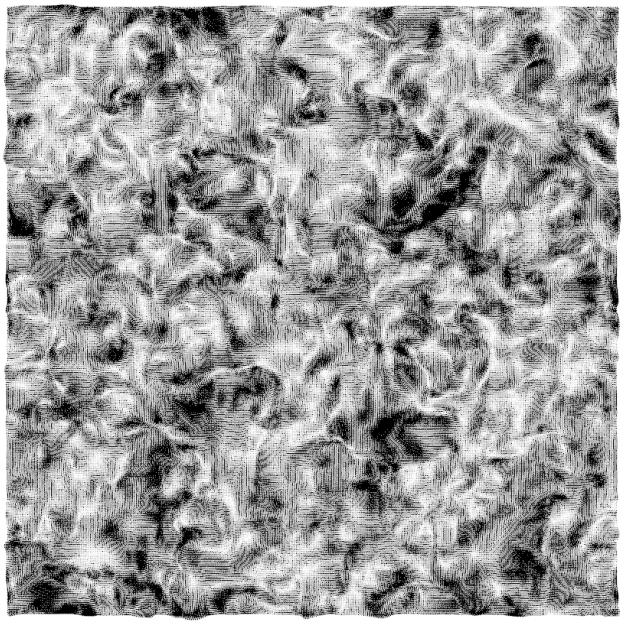

Fig. 2-5 Spatial distribution of the turbulent velocity field corrected by external forcing; velocity vector is plotted in the x-z plane

The energy spectrum of the generated turbulence field is analyzed and shown in Fig. 2-6. The distribution of the turbulent energy spectrum by wavelength can be seen in the energy cascade phenomenon where the energy decreases from large eddies to small eddies. The slope is generally consistent with -5/3, which is known theoretically. However, the generated turbulence has been found to be less than theoretical values for components with small wavelength scale. The impact will be analyzed in the validation section.

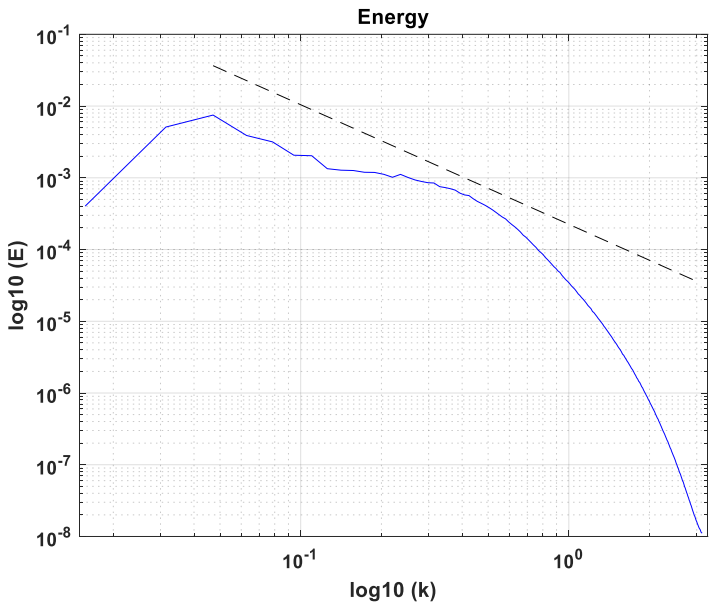

Fig. 2-6 The energy spectra of initial turbulence field

2.3 Wake vortex initialization

A fully rolled-up vortex served as the initial state for each vortex. The distribution of the tangential velocity $V_\theta(\mathrm{r})$ at a distance r away from the center of the vortex core were calculated using the Burnham-Hallock vortex model [43]. The Burnham-Hallock vortex model is widely used for applications such as aircraft wake vortex initialization and the simulating of aircraft behavior near wake vortices. The tangential velocity profile of each vortex was expressed as

$$\boldsymbol{V_\theta(r) = \frac{\Gamma_0}{2\pi r} \times \frac{r^2}{r^2 + r_c^2}} \quad \textbf{(}2.44\textbf{)}$$

In Eq. (2.44), where r_c is the core radius, and Γ_0 is the initial vortex circulation. The core radii were set to $r_c = 3m$ [44]. In case of the initial vortex circulation, it can be calculated through the Eq. (2.45) as a function of the aircraft mass (M) and wingspan (b).

$$\Gamma_0 = \frac{4Mg}{\pi\rho V b} \quad \textbf{(}2.45\textbf{)}$$

The velocity distribution of the V4VS was linearly superimposed on the turbulence field. The wake vortices initially descended at the rate $V_0 = \Gamma_0/2\pi b_0$ according to the Biot–Savart law. The vortex characteristic time scale, $t_0 = b_0/V_0$, was set to 26.3 in all cases for consistency. The non-dimensional turbulence intensity, $\varepsilon^* = (\varepsilon b_0)^{1/3}/V_0$, was 0.203, while the circulation-based Reynolds number, $Re_\Gamma \equiv \Gamma/\nu$, was around 2.3×10^7.

2.4 Core line identification and calculations of wake vortex parameters

The transport and decay processes of the V4VS were quantified by studying the evolution of the related wake vortex parameters. To quantitatively analyze the transport and decay of 4VVS, the vortex core lines of each vortex must be found. It is generally known that vortex core lines can be identified using streamline, maximum vorticity, and minimum pressure. For more accurate core line identification, identification is carried out by two steps of prediction and correction steps, and different parameters are used for each step [45]. However, this method has not been used in this study because it could not distinguish the vortex of the same side or find the position of the core in a complex flow field, such as when non-linear interaction such as linking of vortex core occurs.

In this study, the core lines were identified by performing flow field visualization using the λ_2 iso-surface [46]. The λ_2-criterion is the second eigenvalue of $S_2 + \Omega_2$, where S and Ω are the strain-rate tensor (symmetric part, (2.46)) and the spin tensor (antisymmetric part, (2.47)) of the velocity gradient tensor ($\nabla \mathbf{u}$), respectively. The λ_2-criterion is widely used in computational fluid dynamics because it has a merit of expressing high shear. Where the value of λ_2 is negative has a vortex flow.

$$S_{ij} = \frac{1}{2}\left(\frac{\partial u_i}{\partial x_j} + \frac{\partial u_j}{\partial x_i}\right) \quad (2.46)$$

$$\Omega_{ij} = \frac{1}{2}\left(\frac{\partial u_i}{\partial x_j} - \frac{\partial u_j}{\partial x_i}\right) \quad (2.47)$$

Identification of the vortex core using the negative value of λ_2 in the flow field can confirm the secondary vortex structure (SVS) generated by the interaction as well as the vortex core as shown in Fig. 2-7 a). Since the SVS forms a complex structure around the vortex core, it needs to be filtered to identify the correct core line. By filtering from the vortex core of the expected position based on the size of the λ_2 iso-surface the core lines of wake vortex can be extracted as in Fig. 2-7 b) SVS filtered result.

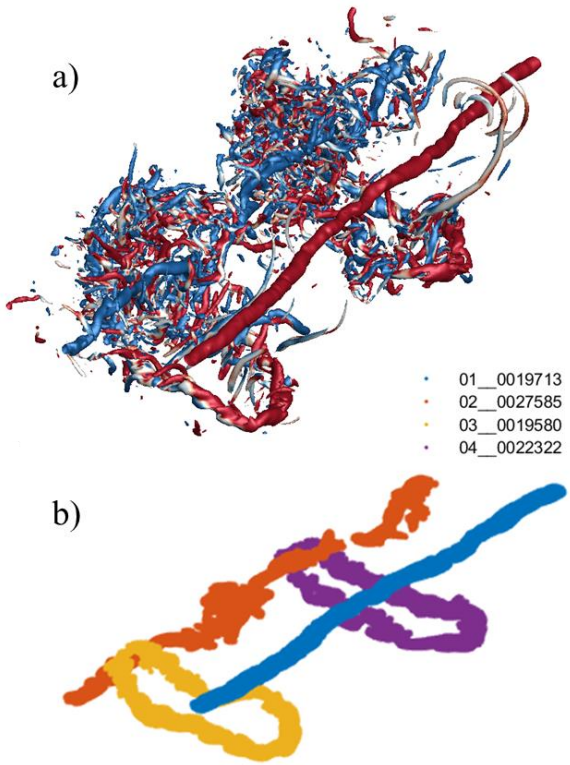

Fig. 2-7 vortex core-line identification;
a) core line identification using $\boldsymbol{\lambda_2}$; b) SVS filtered result

The vortex parameters such as the vertical and lateral positions and circulation were calculated along the core line. Parameters of each vortex were determined by averaging the values obtained for different core segments. Secondary parameters such as vortex spacing and the vertical distance were calculated from the averaged parameters. The vortex spacing was set to zero after linking.

$$\bar{y}(t) = \frac{1}{n}\sum_{i=1}^{n} y(x_i, t) \tag{2.48}$$

$$\bar{z}(t) = \frac{1}{n}\sum_{i=1}^{n} z(x_i, t) \tag{2.49}$$

$$b_c^*(t) = \overline{y_{ss}^*}(t) - \overline{y_{ps}^*}(t) \tag{2.50}$$

$$\Delta z^*(t) = \overline{z_u^*}(t) - \overline{z_l^*}(t) \tag{2.51}$$

Circulation is a variable that is closely related to the wake turbulence hazard. Its magnitude was computed on a plane perpendicular to each core segment to take into account the vortex instability. The value when the circulation becomes maximum according to the distance from the position of the vortex center in each x cross section is defined as (2.53). The averaged total circulation value can also be defined as Eq. (2.54). It can be nondimensionalized by initial circulation strength Γ_0.

$$\Gamma(x_i, r, t) = \oint_c \mathbf{V}_\theta(x_i, r, t)\, dl \tag{2.52}$$

$$\Gamma_{tot}(x_i, t) = \max_r \Gamma(x_i, r, t) \tag{2.53}$$

$$\bar{\Gamma}_{tot}(t) = 1/n \sum_{i=1}^{n} \Gamma_{tot}(x_i, t) \tag{2.54}$$

2.5 Validation of numerical methods

The obtained numerical simulation data were validated by comparing the single wake vortex decay with the results of previous studies. The behavior of post roll-up vortices with respect to nondimensional turbulence intensity is compared. The initial and boundary conditions are set to the same with those of Han et al [10]. The grid size is set to 324 × 128 × 128 and the grid size is (Δx, Δy, Δz) = (1.0 m, 0.66 m, 0.66 m). The initial lateral separation of vortices is b_0 = 16 m. We set the domain length to be long enough in the axial direction to simulate the maximum amplification wavelength of Crow instability. In addition, the length in the transverse direction and the vertical direction corresponds to $5b_0$, which limits the influence of the boundaries. The vortex core radius, r_c, is set to 2 m, and statistical steady state isotropic turbulence is generated using the SNGR and forcing technique. Then, a pair of counter-rotating wake vortices with opposite circulation is generated in the flow field.

The transport and decay of wake vortex for the dimensionless turbulence intensity is visualized by the iso-surface of λ_2 as shown in Fig. 2-8. It can be seen that the non-dimensional time t* required for the linking of wake vortices reduces as the dimensionless turbulence intensity ε* increases. With weak turbulence, it clearly shows the formation of a vortex ring which results from the Crow instability. Also, it has almost symmetrical shape without advection effect by the atmospheric turbulence. Under strong turbulent, it is difficult to observe the formation of the ring, and the asymmetrical behavior of the wake vortices pair with respect to longitudinal direction is confirmed. This is because the atmospheric turbulent is stronger than the circulation of the wake vortices so that the interactions with atmospheric

turbulence are more prominent than the Crow instability.

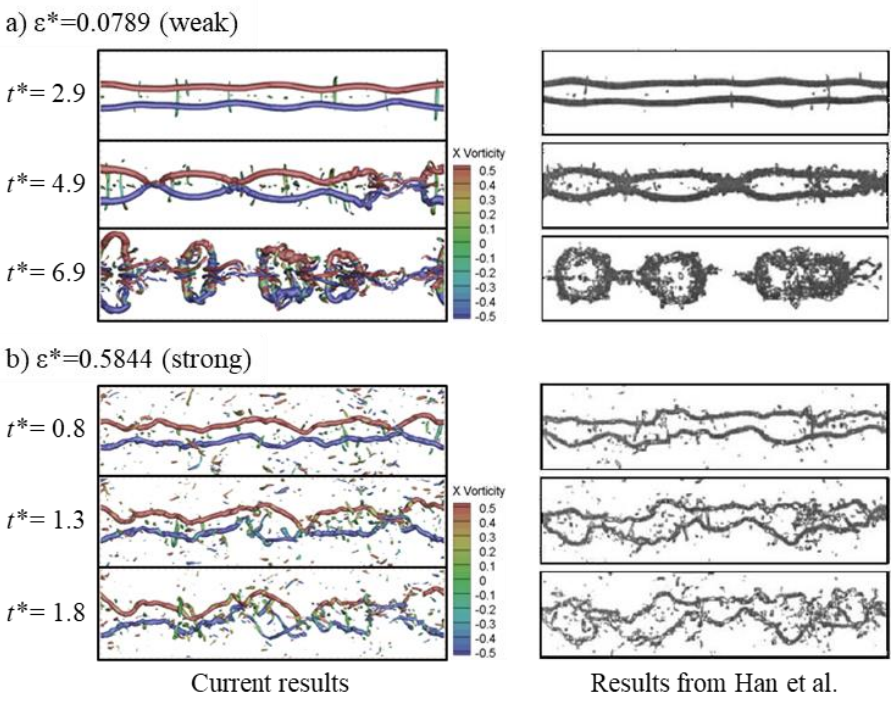

Fig. 2-8 the comparison of numerical simulation with previous study [10];

a) weak turbulence intensities (ε* = 0.0789);

b) strong turbulence intensities (ε* = 0.5844)

In particular, the circulation evolutions of each dimensionless turbulence intensity were compared using Visscher's deterministic wake vortex model (DVM) [17] and Proctor's TASS driven algorithms for wake prediction (TDP) model [47], as shown in Fig. 2-9. The detailed formulas of DVM model are summarized in the appendix A. The obtained data exhibit the two-phase decay characteristics that are consistent with these two vortex models. In the first phase, the circulation intensity does not substantially decrease before the vortices form a ring. The second phase begins with the formation of a ring due to Crow instability. The larger the dimensionless turbulence intensity, the faster the point becomes.

At $\varepsilon^* = 0.1753$, the circulation evolutions in the first phase differ between the two models. The TDP model is physically more valid as the turbulence diffusion increases proportionally to the dimensionless turbulence intensity ε^*. The values of the ε^* used in the DVM model were 0.0623 and 0.0289 indicating relatively low computational accuracy under the high turbulence conditions. In particular, in the case of the vertical position, the rate of change of the vertical position with time can be modeled as shown in Eq. (2.55), considering the induced velocity by the Biot-Savart law between the counter-rotating vortices. As shown in Fig. 2-10, since there is no stratification level due to the potential temperature difference, the vertical position calculated by Biot-Savart law alone is in good agreement with the LES results.

$$\frac{dz^*}{dt^*} = v_{BS}^* = -\Gamma_{tot}^* \quad \textbf{(}2.55\textbf{)}$$

Background turbulence causes perturbation along the core line of the initial wave vortex. The vortex then behaves and this perturbation grows under the influence of the strain field of the other vortex. It is called instability

that the core line is distorted by this growth of perturbation. The energy spectrum of the generated turbulence field is analyzed. The slope is generally consistent with -5/3, which is known theoretically. However, the generated turbulence has been found to be less than theoretical values for components with small wavelength scale.

In vortex problems, instability is primarily affected by large wavelength components. In the validation using the turbulence field used in this study, it was confirmed that the dissipation characteristics known as crow instability, which is the dissipation characteristic of the vortex, were qualitatively and quantitatively consistent with those known in the previous study. Therefore, it can be concluded that the present numerical method has sufficient accuracy to solve the vortex problem.

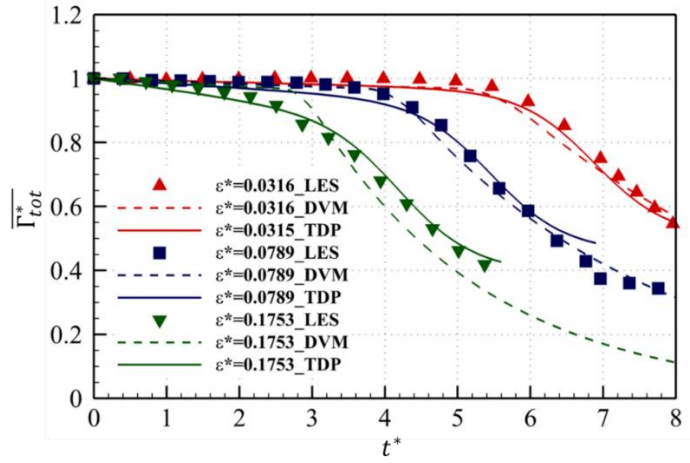

Fig. 2-9 Circulation evolutions observed for different wake vortex models.

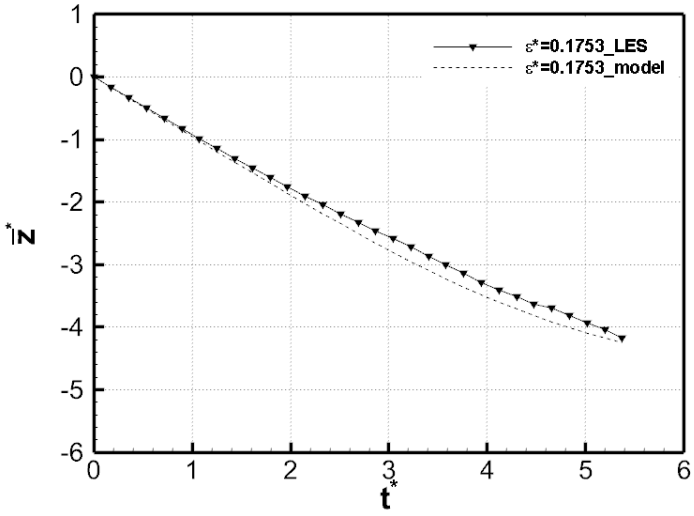

Fig. 2-10 vertical displacement comparison to wake vortex model

Chapter 3. Time delay wake vortex interaction

In this section, the difference in the transport and decay characteristic of single wake vortex pair will be compared to the transport and decay characteristic of multiple wake vortex pair. In cases where interaction happens, a pair of wake vortices is added and after a certain time, another pair of wake vortex is superimposed to the field (Fig. 3-1).

In order to confirm the effect of the interaction, the results of a pair of wake vortices alone are shown in 3.1. In 3.2., an interaction effect will be discussed. Light-medium, medium-medium, and medium-heavy combinations are selected as the cases for confirming the interaction effects. The time difference applied between the preceding and the following vortices is half of the current separation time ruled by the ICAO. This is arbitrarily set by assuming that the aircraft wake vortices move to other places because of various factors such as crosswind, or the crossing of the flight path resulting in the interaction among vortices. To compare the effect of interaction with the cases without interaction, transport and decay characteristic of a single wake vortex pair is discussed.

A pair of fully developed wake vortex pair was simulated using Burnham-Hallock vortex model. The number of grids was 360 × 360 × 120 and the grid size was $\Delta = 0.89$ m. The initial lateral separation of vortices and the circulation strength were set as shown in Table 3.1, according to the size of the aircraft. The vortex core radius was set to $r_c = 2.8$ m, and statistical steady state isotropic turbulence was generated using the SNGR and forcing technique. Then, a pair of counter-rotating vortices with same circulation strength was superimposed in the flow field.

Table 3.1 Vortex parameters for different aircraft sizes

	Light	Medium	Heavy
Airplane model	Business jet	A320 B737	DC-10 B747
Γ_0 [m^2/s]	45	265	400
b_0 [m]	16	27	40
V_0 [m/s]	0.45	1.56	1.59
t_0 [m/s]t	35.74	17.28	25.13

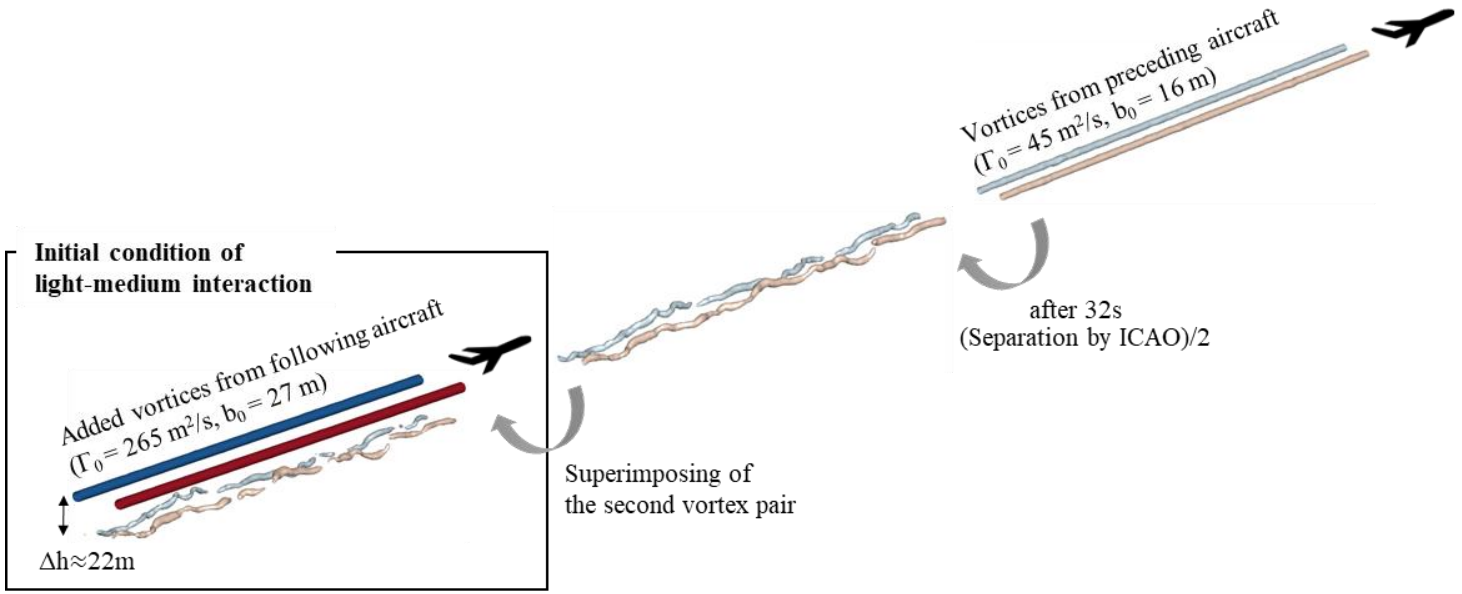

Fig. 3-1 Initial condition for analyzing interaction among vortices

3.1 Single Pair of Vortices

The results of LES simulation of the wake vortices for each aircraft size are present in this section. In the case of vortices from light aircraft, the atmospheric turbulence intensity is relatively stronger than the initial circulation strength of vortices. The dimensionless turbulence intensity is calculated as $\varepsilon^*_{\mathrm{light}} = 0.355$. Therefore, the formation of a ring is not clearly visible, and the irregular distortion of wake vortices due to atmospheric advection effect is observed (Fig. 3-2). In the case of wake vortices from medium aircraft or heavy aircraft, the initial circulation intensity is larger than the one from light aircraft. The dimensionless turbulence intensities are calculated as $\varepsilon^*_{\mathrm{medium}} = 0.121$ and $\varepsilon^*_{\mathrm{heavy}} = 0.135$, respectively.

In other words, the circulation intensity is relatively stronger than the atmospheric turbulence intensity compared to $\varepsilon^*_{\mathrm{light}}$. Therefore, the formation of a vortex ring resulting from the Crow instability is clearly observed. In addition, secondary vortices are generated over time by three-dimensional interaction between the wake vortices and atmosphere.

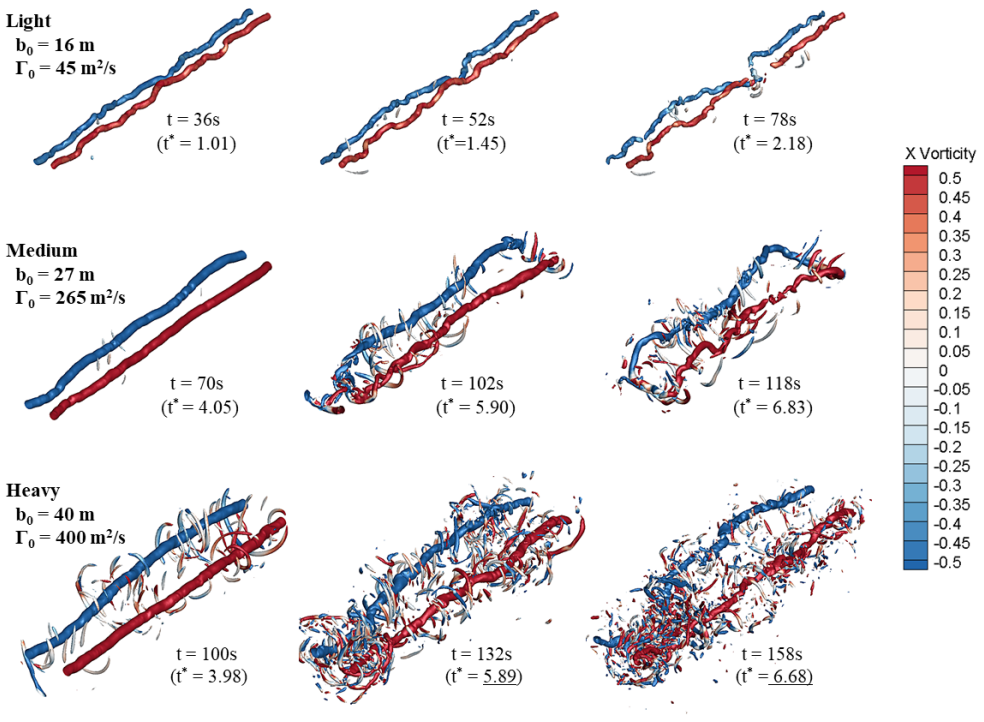

Fig. 3-2 Top views of wake vortices at three different nondimensional times for the cases of light, medium, and heavy aircraft

As shown in Fig. 3-3, the non-dimensional vortex lifespan, which represents the time until the vortex linking decreases with increasing dimensionless turbulence intensity as in previous studies [13].

The difference in the characteristics of vortices from each aircraft is also evident in the descending speed due to induced effect (Fig. 3-3). Vortices from light aircraft has a descending speed of about 0.45 m/s, which is about 30% of that from medium and heavy aircraft, 1.6 m/s. Therefore, it can be seen that if the vortices from lighter aircraft are located higher than the vortices from heavier airplane, there is a greater likelihood that the interaction will not occur due to the difference in descent speed. Considering this, interaction cases are chosen such that the vortices from the relatively light aircraft are located at lower position, and the vortices from the relatively heavy aircraft are at higher position. In the next section, we will look at the mechanism by which the two pairs of vortices meet and interact.

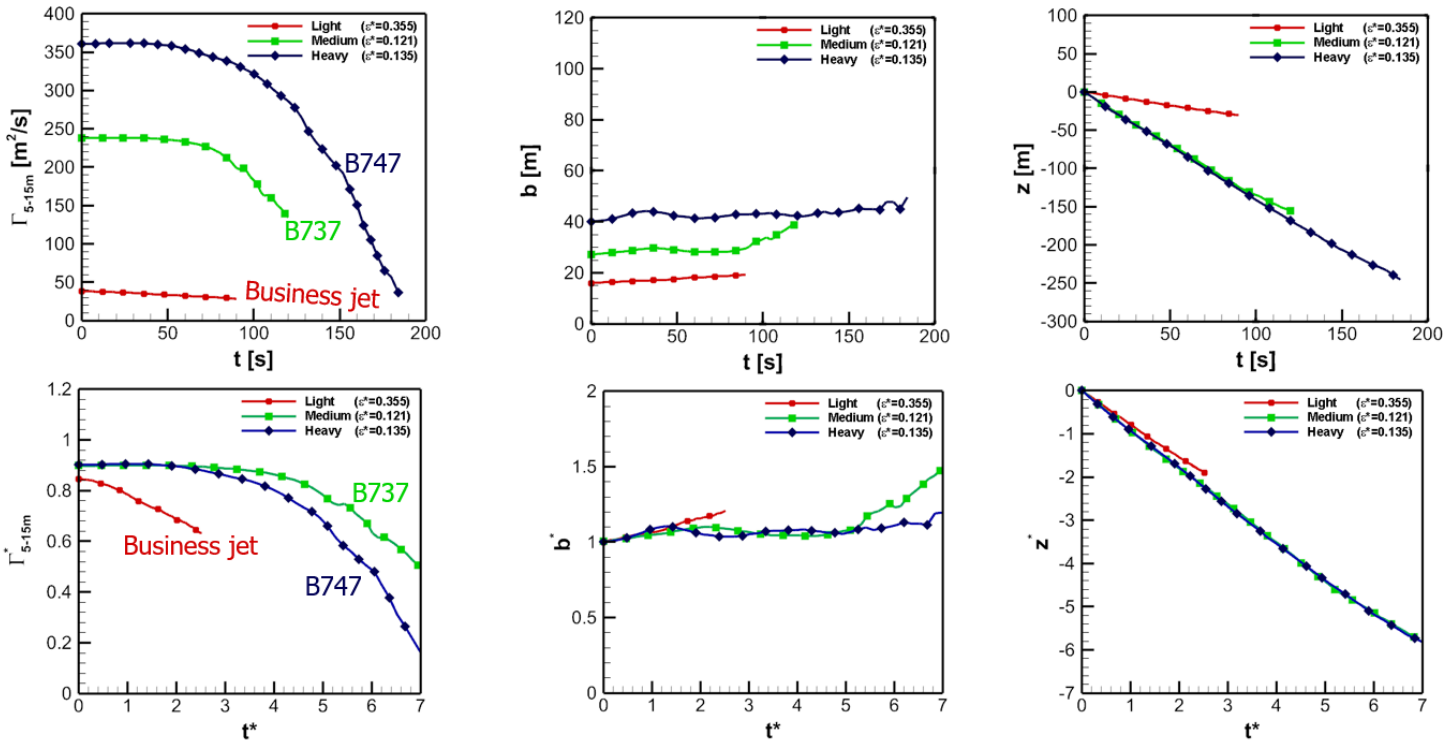

Fig. 3-3 The evolution of averaged vortex circulation and vertical position with respect to aircraft MTOW

3.2 Interaction Between Two Pairs of Vortices

3.2.1 Light – medium wake vortices interaction

As the first case considering interaction, a pair of wake vortices from light aircraft and that from medium aircraft is considered. The vortices from the medium aircraft were initialized 22 m higher and 32 s after the vortices from light aircraft were initialized. The circulation strength of vortices from light aircraft is small compared to the atmospheric turbulence intensity, so vortices are distorted by the atmospheric advection effect. In addition, the descending speed is about 0.45 m/s, which is smaller than the descending speed of vortices from medium aircraft of 1.6 m/s. Due to this difference in descent speed, the distance between the two pairs of vortices is close and the interaction occurs quickly. It is shown that the vortices generated from the light aircraft disappeared due to the strong induced velocity of the vortices made by medium aircraft (Fig. 3-4).

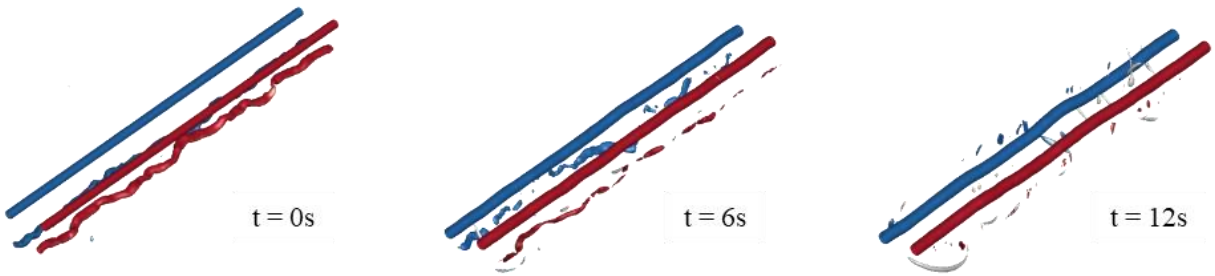

Fig. 3-4 Isometric view of light – medium wake vortices interaction at early stage

Although vortices from light aircraft dissipate quickly, there is an impact on the vortices from medium aircraft (Fig. 3-5). At the beginning, the lateral separation of the vortices from medium aircraft is slightly reduced by the induced effect of vortices from light aircraft. In addition, the vertical position evolution shows that the descent rate also becomes slightly higher. At the same time, the circulation intensity is slightly increased as the vortices from medium aircraft reach the vertical position of the vortices from light aircraft.

The vortices from medium aircraft make the vortices from light aircraft dissipate quickly. As a result, it can be seen that secondary vortices are generated more compared to the case when just a single pair of wake vortices from medium aircraft is considered. These secondary vortices accelerate dissipation by interacting with the primary vortices. Therefore, it can be seen that the vortices interacted with the other ones from light aircraft show an earlier linking compared to the vortices without interaction. After the linking, the circulation strength of vortices from medium aircraft interacted is always lower than the case when just a pair of wake vortices from medium aircraft is considered.

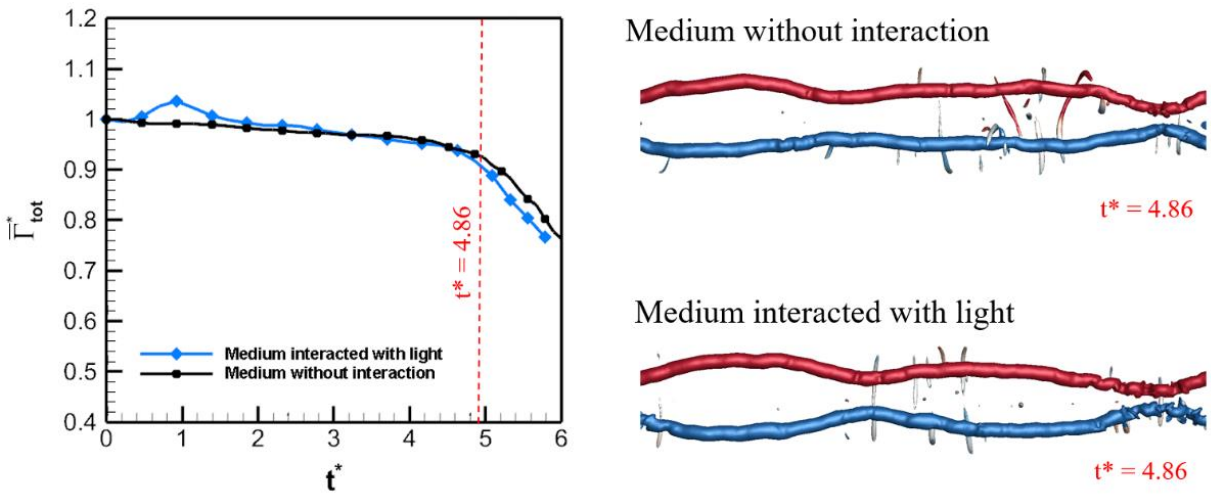

Fig. 3-5 Circulation evolution and top-view at t* = 4.86
of medium wake vortices interacted with light and without interaction

3.2.2 Medium – medium wake vortices interaction

The second case is where interactions between vortices from medium aircraft such as B737 have occurred. 38 s after the generation of the vortices by the preceding aircraft, a pair of vortices from another medium aircraft was formed at 27 m higher.

Before $t^* = 0.58$, the wake vortices formed at higher position move downward while gathering to the center by the induced effect of the vortices at lower part as shown in Fig. 3-6. The vortices located at lower position are being separated with a relatively low descent rate. As a result, it can be seen that at $t^* = 0.58$, the vortices of the trailing aircraft are gathered to $0.45b_0$ compared to the initial vortex spacing b_0. Meanwhile, the vortices of the preceding aircraft are about $1.6b_0$ away from each other.

In addition, at this point, there is a vertical stoppage of the vortices from preceding aircraft. This is because the descent due to the induced velocity of vortices from the preceding aircraft has been canceled by the ascent due to the induced velocity of vortices from the trailing aircraft. On the other hand, vortices from the trailing aircraft go down at a faster rate than when they are acting alone. The reason is that the descent due to the induced velocity of vortices from the trailing aircraft is combined with the descent due to the induced velocity of the vortices from the preceding aircraft.

After $t^* = 0.58$, there is a phenomenon opposite to that of the previous time because of the position change between two pairs of vortices. In other words, the vortices from trailing aircraft that has descended with high speed while gathering toward each other before are being spread on both sides, and the descending speed of them becomes small. As the vortices from preceding aircraft which have been separated away and have maintained its

altitude before on the other hand, the descending speed gradually increases. This is also due to the superposition effect of mutual induction, which can be concatenated with the results before $t^* = 0.58$. The vortices at higher position are gathered close to each other and have a higher descending speed, whereas the vortices at lower position are spread on both sides and have a lower descending speed.

It is confirmed that a pair of vortices (marked in red in Fig. 3-6) starts merging together as they change their vertical positions again at $t^* = 1.39$. Over time, the two vortices are rolled-up together in more parts and are observed to be combined about half the length at $t^* = 1.62$. In addition, at this point, linking occurs with the vortices rotating the other way (marked in blue in Fig. 3-6). It is clearly observed that the circulation intensity decreases after the connection happens. The vortex lifetime is reduced to about one-third compared to the case of single pair of vortices from medium aircraft.

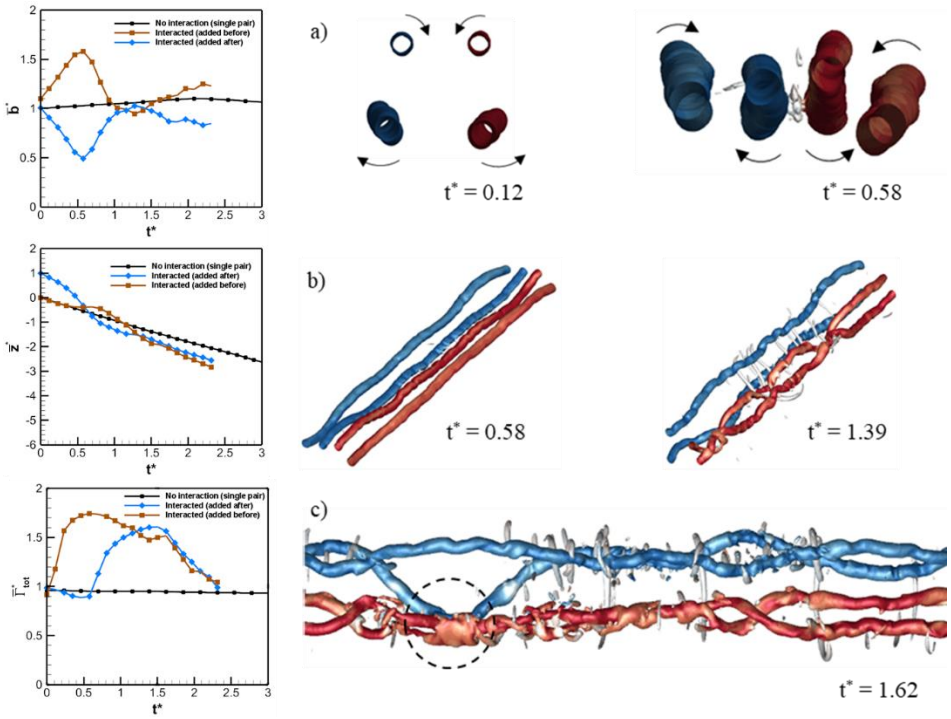

Fig. 3-6 Averaged lateral separation, vertical position, circulation of wake vortices from medium sized aircraft with respect to t^* and snapshots at four different times

3.2.1 Medium – heavy wake vortices interaction

The last is the case where a pair of vortices from heavy aircraft is generated with a height difference of 33 m, and 38 s after the vortices from medium aircraft are formed. As in the previous case, the induced effect of the vortices from medium aircraft makes the vortices from large aircraft move closer. The induced effect of the vortices from large aircraft on the other hand, causes the vortices from medium aircraft to separate in the opposite direction. Up to this point, there seems to be no distinct differences from the previous cases. However, a characteristic phenomenon appears at $t^* = 0.8$ as the vortices from heavy aircraft get close enough for linking to be occurred (Fig. 3-7). As the vortices from heavy aircraft are getting closer, the circulation strength of them becomes smaller.

At $t^* = 1.03$, the linking point is fully attached and the circulation strength decreases by about 20 %. Considering that the time required to reduce the circulation strength to 50 % is about $t^* = 6$ in the case of single pair of vortices from heavy aircraft, the dissipation of the vortices from heavy aircraft interacted by those from medium aircraft can be seen to be very rapid. As vortices from heavy aircraft have a significant impact on airport operations in a view of vortex separation minima, the result of this case shows the possibility of reducing the separation interval between aircraft.

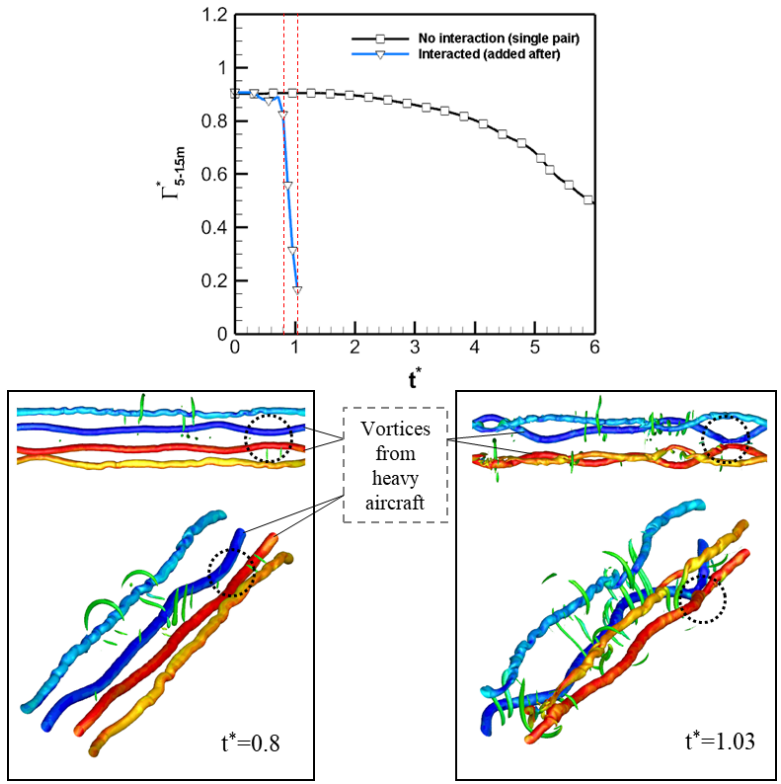

Fig. 3-7 Top views and isometric views at two different time and averaged circulation of wake vortices of heavy aircraft with respect to t^* interacted with vortices from medium one and without interaction

3.3 Summary of the time delay interaction

In order to investigate the interaction between two pairs of wake vortices, the vortex parameters were set with respect to the aircraft classification criteria by ICAO. In three cases, which are the combination of 1) light and medium, 2) medium and medium, and 3) medium and heavy aircraft, wake vortices were added to the flow field with time difference and height difference. It was assumed that the wake vortices formed before had been still remained in atmosphere.

The upper wake vortices were initially moved toward each other and showed a fast descending speed, while the lower wake vortices were initially spread to both sides and showed a slow descending speed. It was confirmed that when the upper wake vortices reached the vertical position of lower wake vortices, different results occurred for three cases. In the case of combination light and medium aircraft, the vortices from light aircraft were rapidly dissipated. In addition, as the vortices from light aircraft interacted with the vortices from medium aircraft, a large number of secondary vortices were generated so that the vortex lifespan shortened. In the medium and medium aircraft case, it was confirmed that the circulation intensity temporarily increased due to the combination of the pair of vortices rotating in the same direction. Then the circulation intensity decreased as the linking happened with the vortices rotating in opposite direction. Finally, it was confirmed that the dissipation of wake vortices from heavy aircraft, which interacted with wake vortices from medium aircraft was 5 times faster than the case of a single pair of wake vortices from heavy aircraft without interaction.

However, in the case of interaction of a wake vortex pair with the current

time delay, it is difficult to quantitatively parameterize the vortex interaction. The difference in the vertical distance between the analysis cases occurs because the vortex pair descends at different speeds over time. Therefore, in order to quantitatively analyze the behavior characteristics, we will define the vertical four vortex system and analyze the behavior characteristics according to the parameters.

Chapter 4. Vertical Four Vortex System

4.1 Definition of a vertical four-vortex system

When a wake vortex from a preceding aircraft cruising the same route is maintained for a long time, a trailing aircraft is induced to the Instrument Landing System (ILS) with a higher path than the preceding aircraft, a wake vortex drift from preceding aircraft occurs on a landing on an adjacent runway at an airport. There is always a difference in the vertical location of the two pairs because of the vertical descent of early generated vortex pair, although the wake vortex is generated in the same position. 4VVS, which interacts with two pairs of wake vortices from different aircraft, is defined as an initial condition. Although each wake vortex pair is generated at a different time, both pairs are initialized simultaneously for parameter quantification. The vertical four-vortex system (V4VS) including the vertical position difference between two wake vortex pairs is described in Fig. 4-1. The lateral displacement of the two vortex pairs was not considered because the preceding and following aircraft were assumed to fly on the same route and the correlation with the previous studies. The initial condition of 4HVS in the previous study is defined as $\theta = 0°$, and 4VVS with two pairs of wake vortices with the same vortex spacing are defined as $\theta = 90°$. The upper vortex pair consists of counter-rotating vortices 1 and 2, and the lower vortex pair consists of vortices 3 and 4. The circulation center on the starboard side is defined as

$$\mathbf{X}_{ss}^{c} = \frac{\Gamma_2 \mathbf{X}_2^{c} + \Gamma_4 \mathbf{X}_4^{c}}{\Gamma_2 + \Gamma_4} \tag{4.1}$$

which is identical to the center of the recirculation region indicated by the blue $\times$ marks in Fig. 1-6. The distance between the starboard side and the port side circulation center is b, and the distance between the upper and lower vortices on each side is h. The difference in vortex spacing is the angle between the lateral axis and the co-rotating vortices θ.

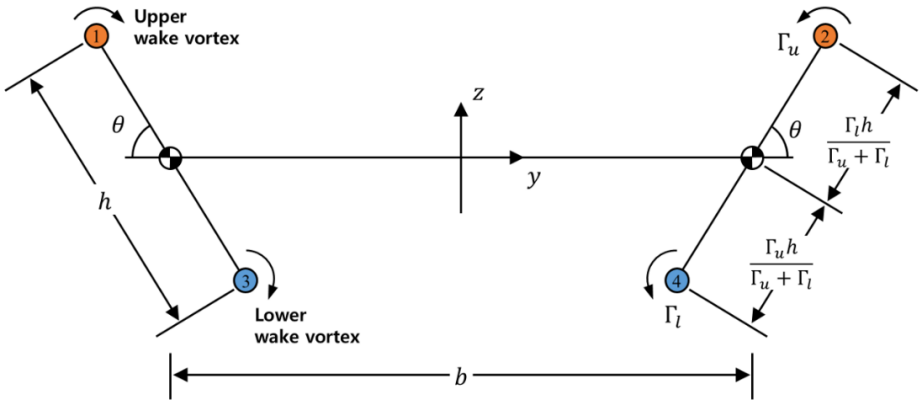

Fig. 4-1 Schematic of the studied vertical four vortex system

4.2 V4VS numerical simulation cases

In Table 4.1, 18 simulation cases with different combinations of the circulation ratio $(\mathrm{R}_\Gamma \equiv \Gamma_u/\Gamma_l)$ and vertical distance $(h^* \equiv h/b)$ are considered. The case names are selected to indicate their parameters. The digits after "Hv" denote the vertical distance, and the digits after "Rg" denote the circulation ratio. The base circulations equal to $530\ \mathrm{m}^2/\mathrm{s}$ and $360\ \mathrm{m}^2/\mathrm{s}$ represent the wake vortices generated by the large and medium aircraft, respectively [44]. Three circulation ratios corresponding to various situations were examined. For example, the case with $\mathrm{R}_\Gamma = 1.47$ implies that the following large aircraft takes off after the preceding medium aircraft. The vertical distance ranged from a half to triple vortex spacing (b_0) considering the descent of the preceding wake vortices. The magnitude of b_0 was set to $47.1\,m$ for the large aircraft; hence, the angle was set to $90°$ in all cases to focus on these two parameters.

Table 4.1 V4VS simulation cases with various combinations of the circulation ratio (R_Γ) and vertical distance (h^*).

h^* \ R_Γ	0.68	1.00	1.47
0.5	Hv05Rg07	Hv05Rg10	Hv05Rg15
1.0	Hv10Rg07	Hv10Rg10	Hv10Rg15
1.5	Hv15Rg07	Hv15Rg10	Hv15Rg15
2.0	Hv20Rg07	Hv20Rg10	Hv20Rg15
2.5	Hv25Rg07	Hv25Rg10	Hv25Rg15
3.0	Hv30Rg07	Hv30Rg10	Hv30Rg15

4.3 Overall temporal evolutions of V4VS

The temporal evolutions of vortex interactions in 18 different cases were analyzed to determine the decay characteristics that induce rapid dissipation. In addition, their interaction mechanisms and related vortex dissipation effects were examined, and parameter criteria for different characteristic decay processes were derived. The V4VS exhibits a two-phase decay similar to that of a single wake vortex that consists of a diffusion phase followed by a rapid decay phase. In the diffusion phase, the vortices dissipate slowly and undergo two motions: the orbital motion (Fig. 1-6; blue lines) and the descent motion (Fig. 1-6; red lines). In the diffusion phase, vortex transport occurs mainly, and this is explained by linear interaction between vortices and distinguished from later non-linear interactions. In the rapid decay phase, the vortex structure collapses due to non-linear interactions.

The overall temporal evolutions of the V4VS observed at various circulation ratios are shown in Fig. 4-2–Fig. 4-4. The V4VS core line was visualized using the λ_2 iso-surface, and the circulation direction of each core was identified by applying a vorticity contour. Snapshots in each case were selected for different states such as the visibility of core-line instability, start of non-linear interactions, and end of non-linear interactions. The initial and final (t* = 5.3) states were added, and five snapshots were depicted for each case. Non-linear interaction refers to the behavior of the entire vortex merged in the Hv05Rg15 case and the linking of a specific position of the vortex in the Hv30Rg15 case. Instability refers to the transformation of the vortex core-line into a sinusoidal wave form, which is a straight line at the beginning of the behavior, which is a continuous development and causes a non-linear interaction. The snapshots were arranged on the time axis so that the non-linear

interaction times could be compared. The second and fourth snapshots have time differences of $0.38t_0$ or $0.76t_0$ based on the third snapshot in most cases. The final V4VS dissipation states were compared using the last snapshots.

Exceptionally, only the two cases in Fig. 4-4 have different final times because of the late non-linear interactions. A single wake vortex pair with the circulation ratio equal to that of the upper vortex pair was added as a control for the numerical experiment, and their final dissipations were compared.

4.3.1 Effect of the vertical distance at a large circulation ratio

The dependence of the transport and decay properties of the V4VS with a circulation ratio of 1.47 on the vertical distance is described in Fig. 4-2. Three characteristic decay processes – merging into a single pair, complex interactions, and formation of a vortex ring – were observed. In the first process, the co-rotating vortices at the same lateral position merged, and a single counter-rotating pair was formed at $h^* = 0.5$. In the second process, the co-rotating vortices at the same lateral position dissipated rapidly at $h^* = 1.0$, leading to complex interactions and the collapse of the coherent V4VS structure. The third decay process resulted in the instability of the counter-rotating upper vortex pair and formation of a train of rings. The train of rings deformed the lower vortex pair and dissipated rapidly at $h^* \geq 1.5$.

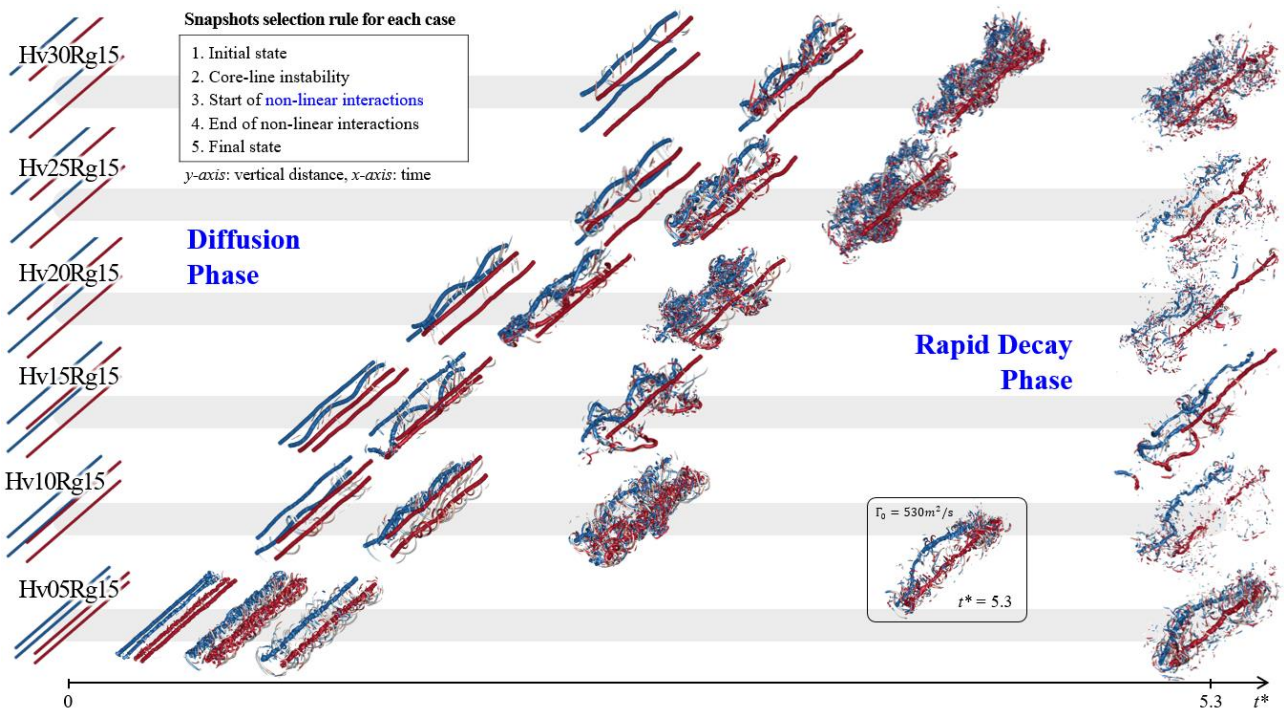

Fig. 4-2 Wake vortex evolution observed at the circulation ratio $R_\Gamma = 1.47$ and dissipation of the single wake vortex pair at $\Gamma_0 = 530\ m^2/s$.

4.3.2 Effect of the vertical distance at the same circulation

The dependence of the transport and decay properties of the V4VS with a circulation ratio of 1.47 on the vertical distance is described in Fig. 4-2. Three characteristic decay processes – merging into a single pair, complex interactions, and formation of a vortex ring – were observed. In the first process, the co-rotating vortices at the same lateral position merged, and a single counter-rotating pair

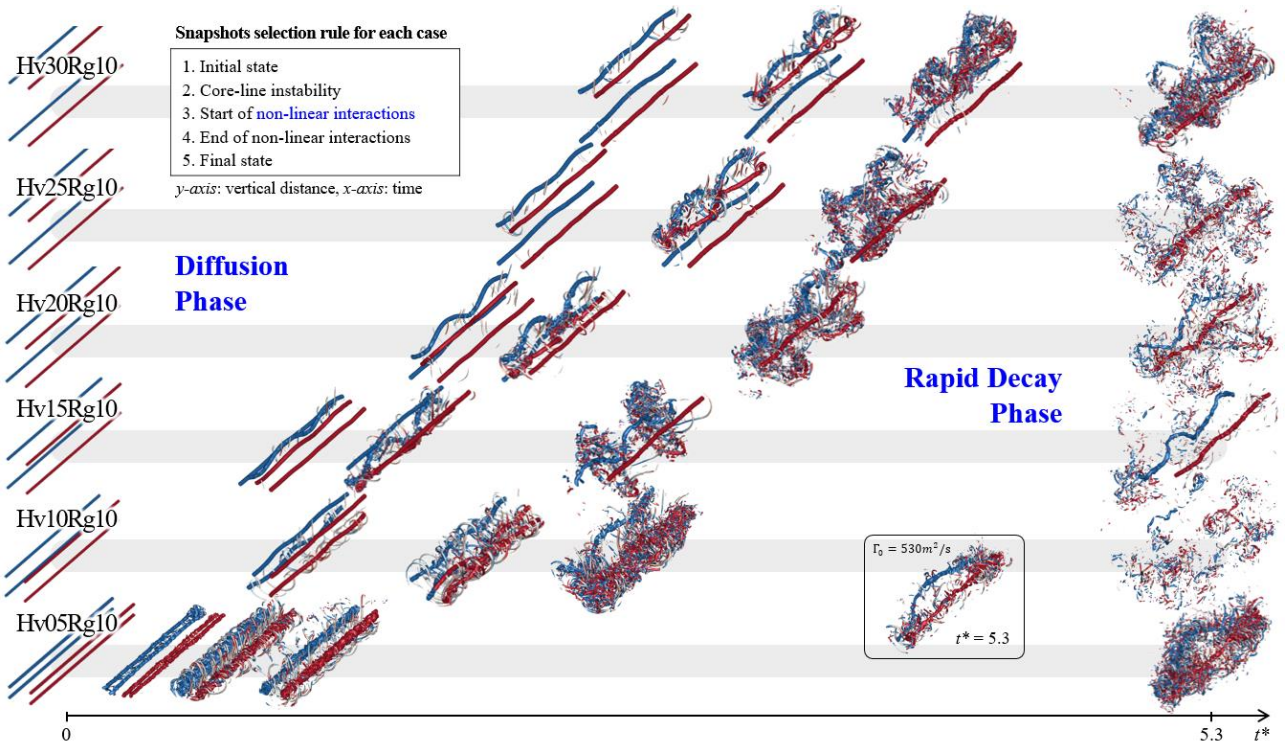

Fig. 4-3 Wake vortex evolution observed at the circulation ratio $R_\Gamma = 1.0$ and dissipation of the single wake vortex pair at $\Gamma_0 = 530\ m^2/s$.

4.3.3 Effect of the vertical distance at a small circulation ratio

The dependence of the transport and decay properties of the V4VS with a circulation ratio of 0.68 on the vertical distance is shown in Fig. 4-4. The temporal evolution of the V4VS with $h^* \leq 2.0$ is similar to that observed at $\mathrm{R}_\Gamma = 1.47$. As the vertical distance further increased, additional decay processes were detected at $h^* = 3.0$, and the upper vortex ring formed by linking has not apparently affected the dissipation of the lower vortex pair.

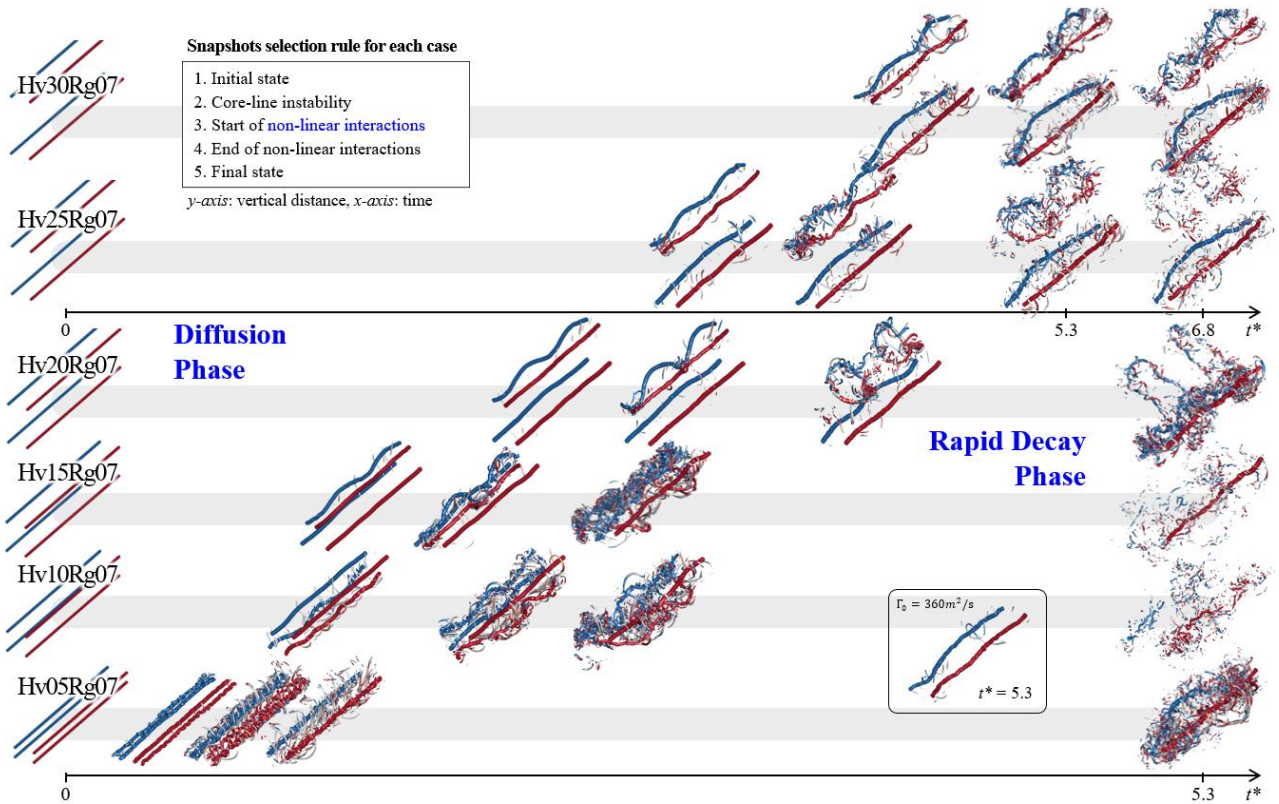

Fig. 4-4 Wake vortex evolution observed at the circulation ratio $R_\Gamma = 0.68$ and dissipation of the single wake vortex pair at $\Gamma_0 = 360\ m^2/s$.

4.4 Criteria for switching between different decay processes

Four different vortex decay processes were detected: merging into a single counter-rotating pair, occurrence of complex interactions followed by rapid dissipation, and formation of vortex rings with or without deforming the lower vortex pair. These four processes can be divided into two groups based on the type of the non-linear interaction pair. At $h^* \leq 1.0$, non-linear interactions between the co-rotating vortices occur, while at $h^* \geq 1.5$, non-linear interactions between the counter-rotating upper vortex pairs are observed. Hence, the type of the non-linear interaction pair varies between the vertical distances of 1 and 1.5. The vertical differences, Δz^*, computed for nine cases at a vertical distance of 1.5 or less are compared in Fig. 4-5. In the six cases with $h^* \leq 1.0$, the vortex transport proceeds through orbital motion, and no differences at various circulation ratios are observed (in contrast to the three cases with $h^* \geq 1.5$). The co-rotating vortices approach during the orbital motion, and in the case of Hv10Rg10, the vertical distance does not reach −1 after a half orbit rotation ($t^* \cong 1.1$). The same phenomenon is observed at $h^* = 0.5$ (yellow dotted line), which is consistent with the experimental results obtained for the merging of co-rotating vortices [29]. Therefore, the criterion for switching the non-linear interactions is $h^* \cong 1.25$ rather than $h^* = 1.0$.

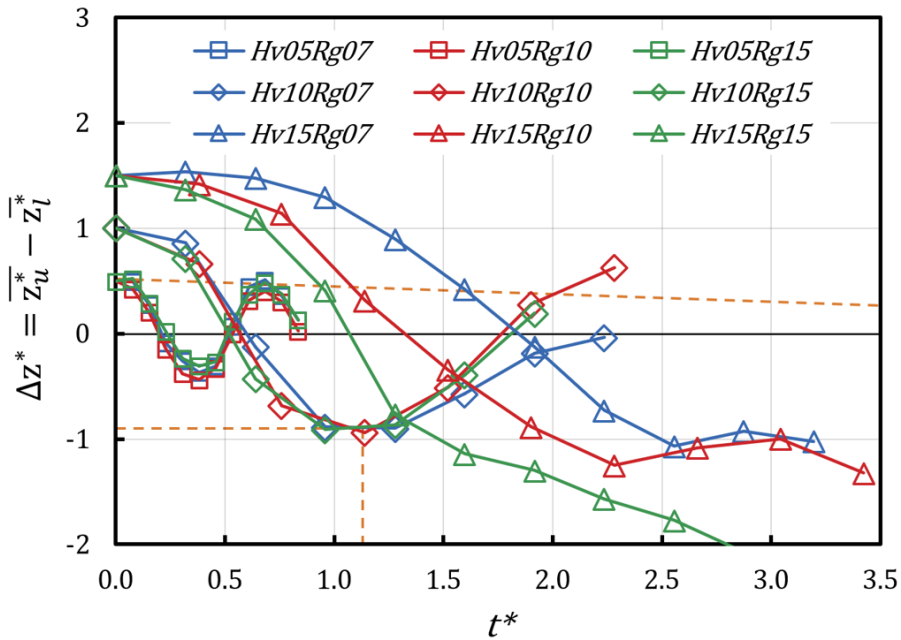

Fig. 4-5 Vertical distance vortex evolutions with respect to the initial vertical distance.

4.4.1 Non-linear interactions of the co-rotating pair

In this section, two vortex decay processes – merging into a single pair and complex interactions followed by rapid dissipation – were analyzed. The development of vortex instability, which is the main cause of non-linear interactions, is examined by plotting the evolution of longitudinal modal energies in Fig. 4-6. The cases with the same circulation ratio representing the vertical distances of 0.5 and 1.0 were Hv05Rg15 and Hv10Rg15, respectively. Here, vortex instability develops under the influence of the strain fields of other vortices, and the unstable wavelength varies with the circulation direction and distance between the interacting vortices. Long-wave instability develops when the counter-rotating vortices interact at a distance of the vortex spacing scale, and the unstable wavelength is $\lambda_{long} \cong 8.0b_0$ [15]. Short-wave instability develops when the co-rotating vortices interact at a distance of the core radius scale, and the unstable wavelength is $\lambda_{short} \cong 0.126b_0$ [48]. The longitudinal model energy is analyzed from 8 to 0.125 vortex spacing to cover the entire range.

The development of short-wave instability indicates that non-linear interactions have started. When Hv05Rg15 rapidly begins to develop the short-wave instability, the same process gradually occurs for Hv10Rg15. The difference can be analyzed as the other instabilities at the starting time of non-linear interactions (red boxes). While Hv05Rg15 shows little development of the long-wave instability, Hv10Rg15 starts non-linear interactions with the development of long- and medium-wave instabilities. Because the core line of Hv10Rg15 interacts in a disturbed state, the distance between the vortices is not consistent, which makes their interactions more complicated. Thus, the different decay processes originate from the vortex instability

development.

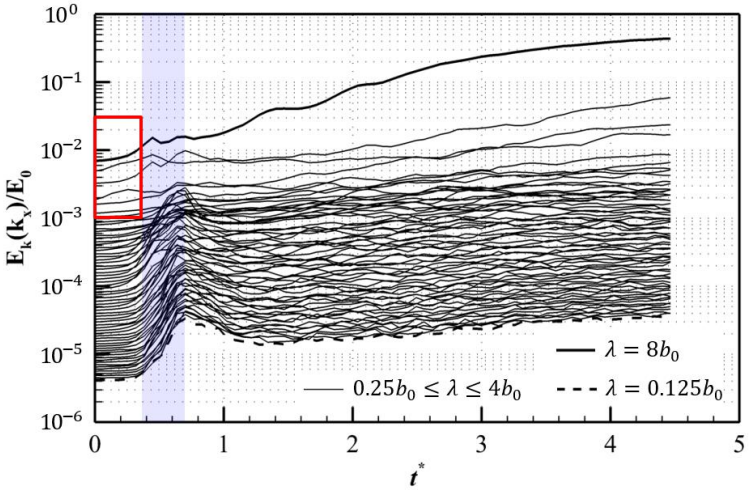

a) Hv05Rg15 - Merging (non-linear interaction)

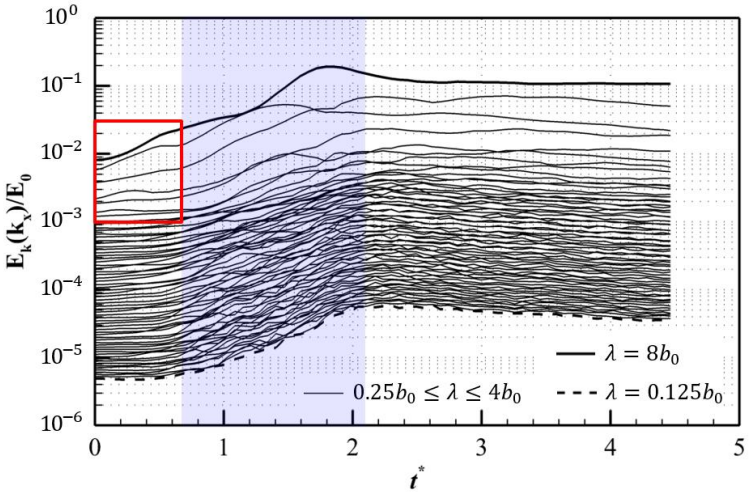

b) Hv10Rg15 - Wrapping (non-linear interaction)

Fig. 4-6 Longitudinal modal energy evolutions observed for a) Hv05Rg15 and b) Hv10Rg15.

4.4.2 Two decay processes occurring at a high vertical distance

The other two decay processes involving the formation of the upper vortex ring with or without a deformation of the lower vortex pair were analyzed as well. In most cases, the upper vortex ring encounters the lower vortex pair, resulting in rapid dissipation. However, in some cases, the upper vortex ring dissipates without encountering the lower vortex pair. The core line instability angles of the second snapshots, vortex lifespans, and vertical distances of the third snapshots in Fig. 4-2–Fig. 4-4 are compared in Fig. 4-7.

The instability angles (green columns) were determined to evaluate the effect of the lower vortex pair. The instabilities of the single wake vortex were developed in the planes inclined at an angle of approximately $45°$ with respect to the horizontal plane, where the maximum effect of the strain field was observed [49]. The instability angle increases due to the effect produced by the lower vortex pair. Therefore, the core line instability angle can quantify the effect of the lower vortex pair in each case, and the angle close to $45°$ observed in cases Hv25Rg07 and Hv30Rg07 means that this effect is negligible (green dotted line). In the case of Hv25Rg15, the angle is also close to $45°$, but only because the direction of the maximum strain field has changed due to the reversal of the vertical location of the two pairs.

The lifespans of the upper vortices (t^*_{lifespan}, blue columns) were compared to further access the effect of the lower vortex pair. Without this effect, the spacing of the upper vortex pair cannot be reduced by mutual induction and consequently, vortex linking may not be promoted. The lifespan at each circulation ratio tends to increase proportionally with the vertical distance (blue dotted line). This proportional relationship is not observed at $\mathrm{R}_\Gamma =$

0.68 and $h^* \geq 2.5$, and the vortex lifespan is significantly increased. In the two cases of Hv25Rg07 and Hv30Rg07, the decay processes significantly differ from those occurred in the other cases.

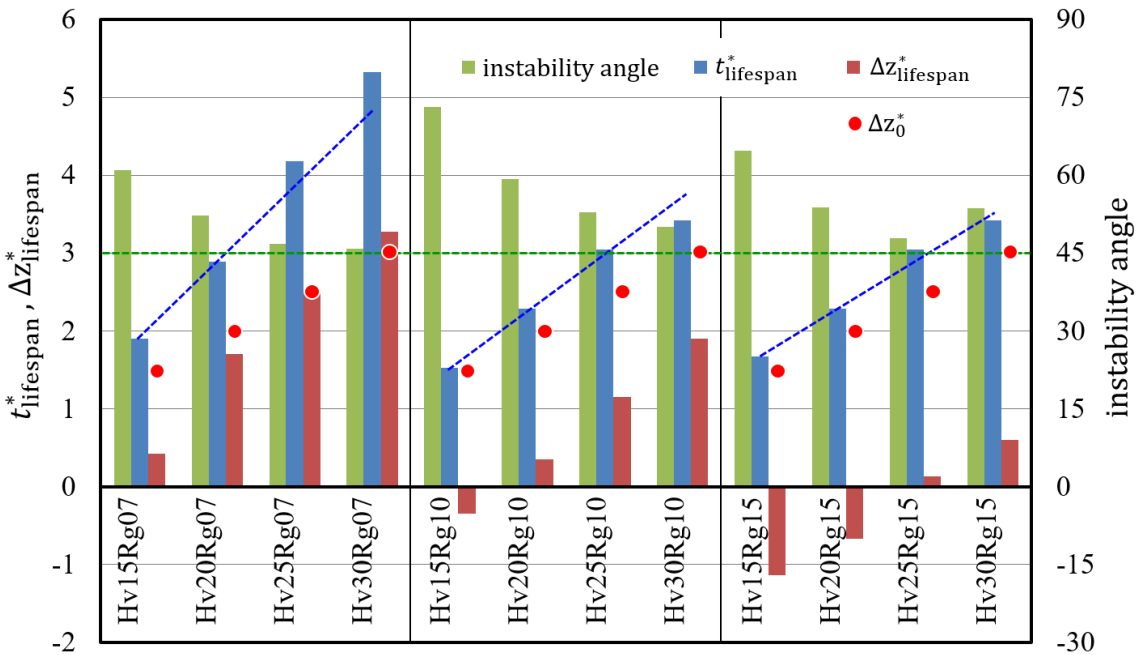

Fig. 4-7 Core line instability angles, non-linear times to linking, and vertical distances between the upper and lower vortices for different cases.

4.4.3 Linking of the upper vortex pair

The differences between the vertical distances at the time of linking ($\Delta z^*_{\mathrm{lifespan}}$, red columns in Fig. 4-7) were compared to obtain a criterion for switching the processes in the rapid decay phase. In most cases, the vertical distance decreased with respect to the initial vertical distance (Δz^*_0, red circles), and in some cases, it decreased to below zero due to the reversal of the vertical location. In contrast, the vertical distances of Hv25Rg07 and Hv30Rg07 did not decrease. The circulation ratio of 0.68 initially increased the vertical distance. If the mutual induction of the lower vortex pair does not sufficiently reduce the upper vortex spacing, then the vertical distance cannot be decreased. Thus, at a certain criterion, the interaction effect becomes negligible, and the two pairs of vortices are separately dissipated. The measure of the criterion is defined as the amount of the vertical distance reduction. If the vertical distance is not decreased until the time of linking, it will not be further reduced because of the descent rate retained during the transformation of the vortex ring [50]. Therefore, this criterion corresponds to the zero reduction in the vertical distance. The vertical distance reduction is approximated by a second-order polynomial with two parameters as shown in Fig. 4-8. The approximated criterion for interaction of upper and lower vortex pair can be expressed by Eq. (4.2) with the constants listed in Table 4.2. Here, the approximated vertical distance reduction increases quadratically with increasing circulation ratio on the basis of around 1.3.

$$\begin{aligned}&\Delta z^*_{\mathrm{lifespan}} - \Delta z^*_0 \\ &= c_{20}(R_\Gamma)^2 + c_{11}R_\Gamma h^* + c_{02}(h^*)^2 + c_{10}R_\Gamma + c_{01}h^* + c_{00}\end{aligned} \tag{4.2}$$

Table 4.2 Constants obtained for strong and weak interactions.

constant	value	constant	value
c_{20}	1.995	c_{10}	-5.264
c_{11}	-0.8242	c_{01}	2.037
c_{02}	-0.1432	c_{00}	-0.1773

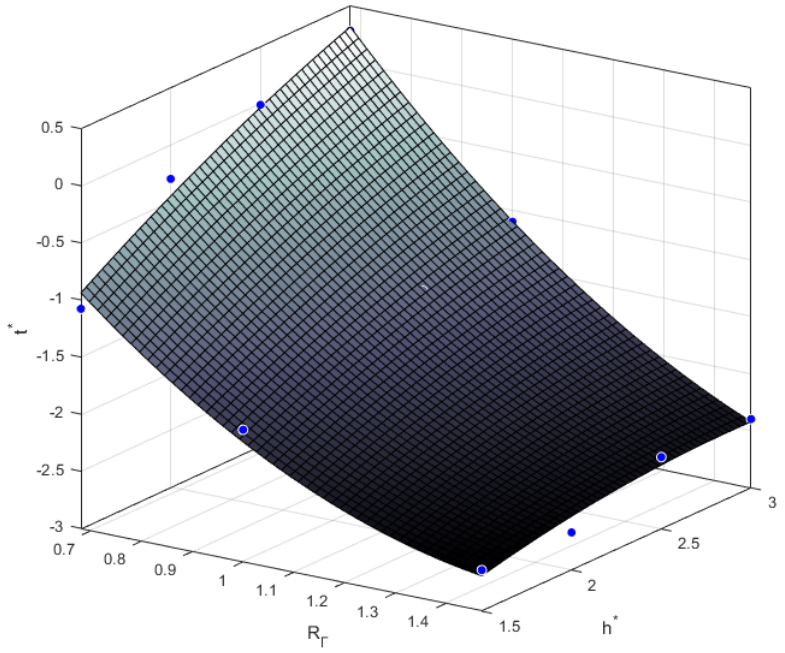

Fig. 4-8 vertical distance reduction is approximated by a second-order polynomial

4.5 Four decay processes of V4VS

The main V4VS decay processes and their criteria are summarized in Fig. 4-9. The decay processes that induce the rapid dissipation of wake vortices such as merging into a single counter-rotating pair, rapid dissipation, and formation of a vortex ring with or without a deformation of the lower vortex pair. These processes are named as merging, wrapping, ring deformation, parallel ring dissipation.

The four processes are divided into two groups based on the vertical distance criterion of 1.25, resulting in the formation of different non-linear interaction pairs. The co-rotating vortex interactions include the merging and wrapping processes separated by the vertical distance criterion of 0.75. The processes of the upper vortex pair linking include ring deformation and parallel ring dissipation affected by two parameters and separated by the criterion of the vertical distance reduction of zero.

Since most of the analysis cases show similar behavior characteristics, the analysis results of the selected cases with characteristic non-linear behaviors were analyzed. Vortex core location and velocity evolution in time are plotted for every case. Modal energy analysis was performed to quantitatively confirm the growth of instability of unstable wavelength developed during the interaction of 4VVS, and only the components corresponding to three instability types were summarized and compared. Comparing the growth by type of instability can be identified by the unstable instability which mainly developed by case.

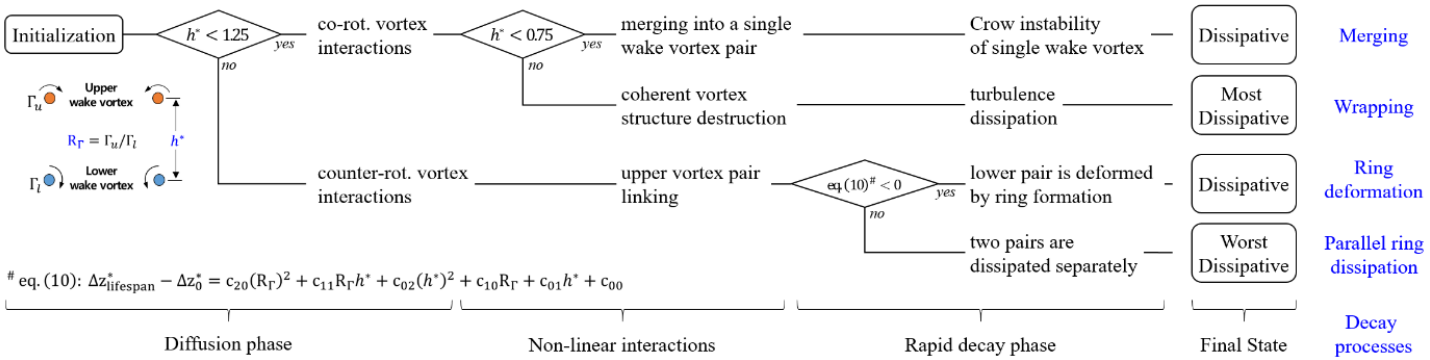

Fig. 4-9 A map of the V4VS transport and decay processes occurring at $\theta = 90°$.

4.5.1 Merging – the 1st V4VS characteristic decay process

The first V4VS characteristic decay process is merging into a single vortex pair after one orbital motion of the vortices located on the same side as summarized in Fig. 4-10. It occurs when the vertical distance is close to a half vortex spacing and is similar to the roll-up process of the vortices generated in a high lift configuration [25]. After merging, vortex dissipation accompanied by the Crow instability phenomenon (similar to that observed for a single wake vortex) occurs and continues for a relatively long time.

The transport and decay of Hv05Rg15 are analyzed in Fig. 4-10 as a representative case for wrapping decay process. The time evolution and the core velocity graph show the distinct orbital motion of co-rotating vortices on the same side when the vertical distance is close. When $t^* = 0.32$, the positions of the upper and lower vortices were reversed, and the orbital time for the isolated vortex pair (τ^*) was 0.41 and the rotating motion was accelerated. According to the orbital motion, upper vortex spacing decreases again after 44% increase, while lower vortex spacing increases again after 29% decrease. The distance between vortices on the same side is minimum when the vortex spacing change is maximum and decreases continuously with time. The short-wave instability grows along the core-line at the beginning of the decay process.

When $t^* = 0.64$, the vertical position of the upper and lower vortex changes again. At this time, $\tau^* = 0.81$, and the orbital motion of the co-rotating vortices proceeded more than one orbit. The decrease in the distance between vortices on the same side shows that the period is shortened. A thin vorticity bridge resulting from the perturbation disturbance of the instability is connected throughout the co-rotating vortices. Vorticity

bridges are increasingly complex and energy exchange occurs between vortices.

When $t^* = 0.96$, co-rotating vortices are merged into a single vortex. The co-rotating pairs are mered after the occurrence of short-wavelength sinuous disturbance, Bristol et al. And the development of instability is consistent. [36] Bristol et al. [51] is a model for the towing tank experiment, which agrees well with the analysis that merging between co-rotating vortex pairs occurs within one revolution of rotation based on the circulation centroid.

Since the merge occurs in the entire vortex core, it forms a single wake vortex pair after being merged. After combining, we show the transport and decay of a single wake vortex that is linked with the development of long-wave instability, such as $t^* = 4.47$. The distinctive orbital motion of 4VVS can be classified as periodic according to the Donaldson-Bilanin diagram, followed by the merging of co-rotating vortices. For three cases with a vertical distance of $0.5b_0$, the decay process is merged into the same single vortex pair, regardless of the value of $\mathrm{R_\Gamma}$.

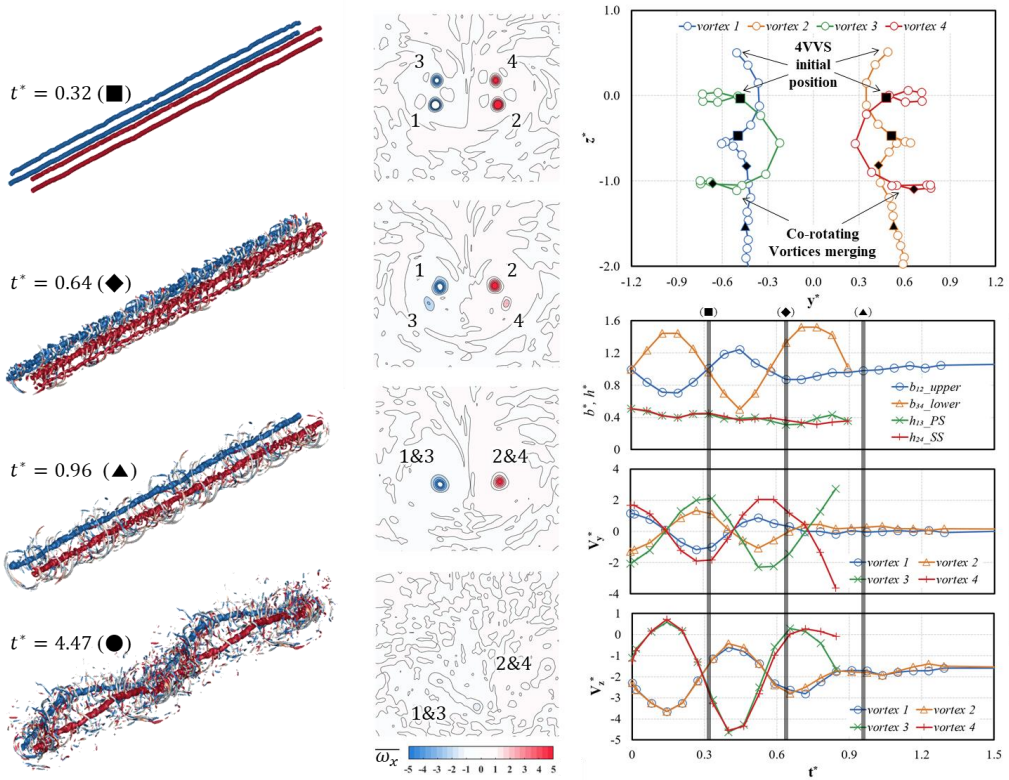

Fig. 4-10 time evolution of Hv05Rg15 ($R_\Gamma = 1.47,\ R_h = 0.5$)

iso-λ_2 surface (left); $\overline{\omega_x}$ contour (middle); and time evolution of vortices core (right)

4.5.2 Wrapping – the 2nd V4VS characteristic decay process

The second vortex decay process occurs when the vertical distance is close to the vortex spacing. The coherent vortex structure collapses after the interaction due to the instability developed during the orbital motion of the co-rotating vortices and is rapidly dissipated. The second process is named wrapping because it is similar to the wrapping and ring-rejection activities. This phenomenon is identical to the process observed by a previous study where non-linear interactions started in a perturbed state of the vortex core line [36]. In that study, the inner vortex wrapped Ω hoops around the outer vortex to form a ring, whereas in this work, the coherent structure of the vortices collapsed and rapidly dissipated, owing to the different circulation ratios. The second decay process indicates that the interactions of co-rotating vortices with close circulation strengths could lead to rapid dissipation if their instability had been developed earlier.

The transport and decay of Hv10Rg10 are analyzed in Fig. 4-11 as a representative case for wrapping decay process. At the beginning of the decay process, the orbital motion appears to be the same as in the case of $R_h = 0.5$, which is closer to the vertical distance, but the non-linear interaction such as vortex merging tends to appear. When $t^* = 0.38$, the orbital motion reduces the interval of the upper vortex pair, while the interval of the lower vortex pair increases. Vortex spacing changes up to 55% and induces a descent velocity difference to bring the co-rotating pair closer. Vortex spacing scale instability develops along the core-line.

When $t^* = 1.14$, the rotation of the half orbit progresses and the vertical location of the upper pair and the lower pair changes. The instability in the upper vortex pair develops prominently along the incline of 35 degrees with

respect to the horizontal plane. Instability of the lower vortex pair with increased spacing is slow, although the instability increases rapidly due to the increased imposed strain filed due to the reduction of the spacing of the upper pair.

When $t^* = 1.90$, a vortex bridge is generated by the SVS and linking occurs throughout the vortex. Linking vortices occur mainly between co-rotating vortices in the same direction, and after linking, the coherent structure of 4VVS collapses and is rapidly dissipated. The feature that distinguishes from the previous merging characteristic is the difference in the vortex merging process. The merging proceeds after crow type instability has developed, which is characterized by a complicated characteristic and cannot maintain the vortex core structure and is rapidly dissipated.

The non-linear interaction occurs due to the instability of co-rotating vortices resulting in simultaneous linking and merging. For three cases with a vertical distance of $1.0b_0$, the same non-linear interaction behavior occurs regardless of the value of R_Γ.

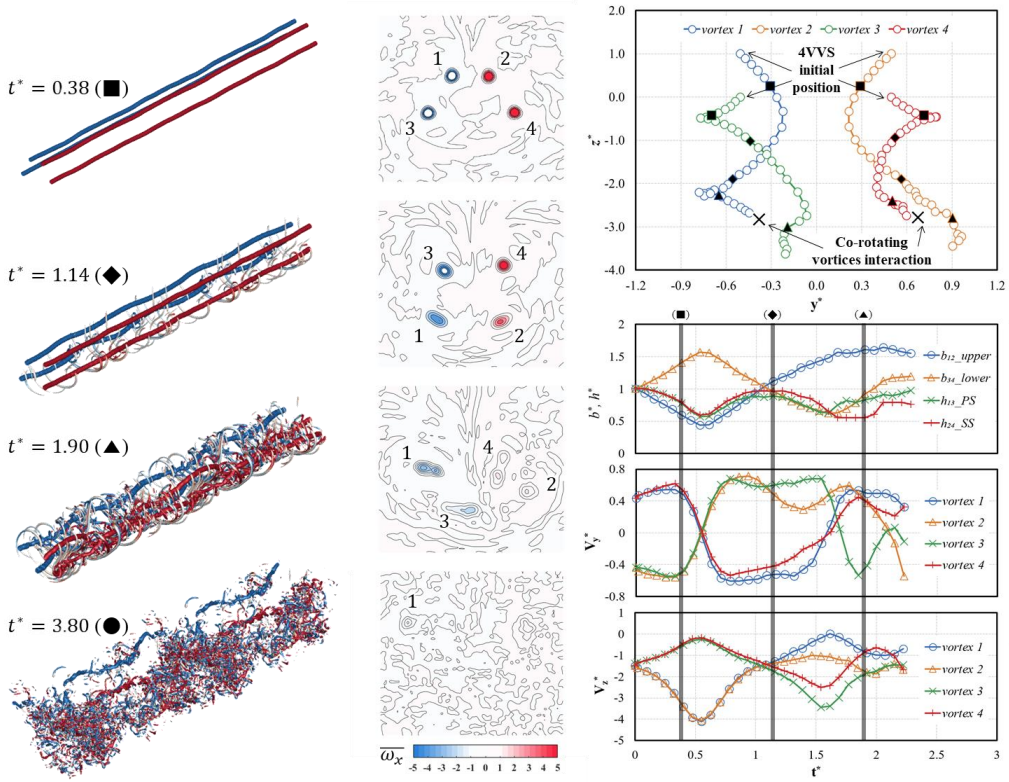

Fig. 4-11 time evolution of Hv10Rg10 ($R_\Gamma = 1.00,\ R_h = 1.0$)

iso-λ_2 surface (left); $\overline{\omega_x}$ contour (middle); and time evolution of vortices core (right)

4.5.3 Ring deformation – the 3rd V4VS characteristic decay process

The third characteristic decay process is the formation of the upper vortex ring followed by the encounter of the two vortex pairs, which leads to their deformation and rapid dissipation of the V4VS. The third process occurs under the conditions corresponding to the negative vertical distance reduction. The condition of $R_\Gamma \geq 1.0$ is likely to cause ring deformation because the difference in the initial descent rate decreases the distance between the two pairs. The condition of $R_\Gamma < 1.0$ at a vertical distance twice as large as the vortex spacing causes the upper vortex spacing to decrease and the lower vortex pair spacing to increase due to mutual induction. These spacing variations decrease the distance between the two pairs resulting in ring deformation.

The transport and decay of Hv15Rg15 are analyzed in Fig. 4-12 as a representative case for ring deformation decay process. The orbital motion of the co-rotating vortices is not apparent, and vortex pair linking occurs to form the train of vortex ring. At the initial $t^* = 0.32$, the orbital motion of co-rotating vortices on the same side reduces the b_c of the upper vortex pair, increases the b_c of the lower vortex pair, and the initial disturbance perturbation occurs along the core-line.

When $t^* = 0.96$, the distance between the two pairs approaches $0.7b_0$ due to the difference in descent speed caused by the variation of the vortex spacing. The rotation of each side is proceeded by the quarter orbital motion. It can be seen that $\tau^* = 0.14$ at this time, the orbital motion is accelerated by the reduction of the spacing.

The development of instability resulted in a marked increase in disturbance perturbation along the plane inclined 70deg from the ground in the

upper vortex pair. Due to instability, a streak of SVS begins to form between upper vortices. This is because the effect of the strain field is strengthened by the influence of the decreased b_c of the upper pair. In addition, the developmental direction of the instability changes due to the strain field of the lower vortex.

When $t^* = 1.6$, the vertical positions of the upper and lower vortices change each other. While the upper pair is passing between the lower pair, the vortex spacing approaches to $0.48b_0$, and the collapse point occurs in the upper vortex pair due to instability development and linking. After linking, train of vortex ring is formed. It is generally known that the vortex life span, which is the time until linking of counter-rotating vortex pair occurs, is halved when the vortex spacing is reduced by $1/\sqrt{2}$ times under the same background turbulence conditions [17].

When $t^* = 3.83$, the lower vortex pair also undergoes distortion due to the vortex ring, loses its coherent vortex structure and begins to dissipate rapidly. The location and time of linking of the upper vortex pair varies depending on the parameter. The vortex interaction is mainly occurred in the same direction, and it is confirmed that interaction between vortex pair with vertical distance leads to linking of upper vortex pair and induces rapid dissipation.

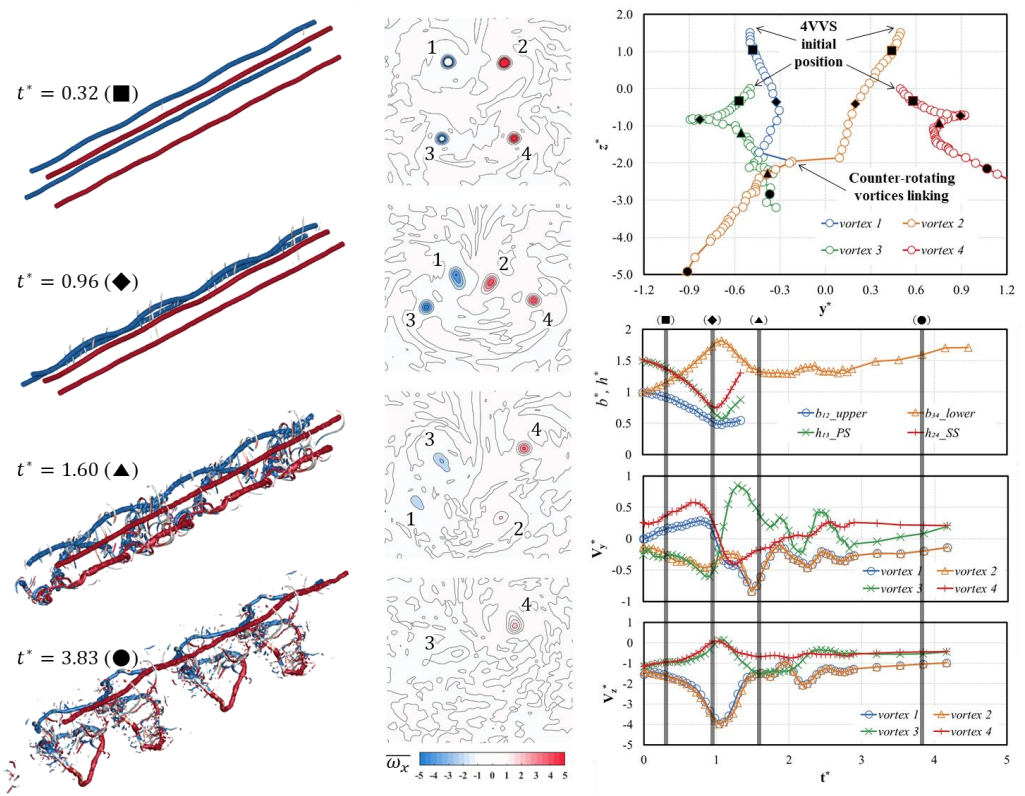

Fig. 4-12 time evolution of Hv15Rg15 ($R_\Gamma = 1.47,\ h = 1.5$)

iso-λ_2 surface (left); $\overline{\omega_x}$ contour (middle); and time evolution of vortices core (right)

4.5.4 Parallel ring dissipation – the 4th V4VS characteristic decay process

The fourth characteristic decay process is the parallel dissipation of the upper vortex ring and lower vortex pair without any direct interactions. The latter do not occur because of the high vertical distance, and the vortices are gradually dissipated. Instead, mutual induction increases the spacing of the lower vortex pair, resulting in a longer lifespan. The fourth process is observed when the vertical distance reduction is above zero, and mainly – when the circulation ratio is less than one and the two vortex pairs are distant.

The overall behavior of the fast vortex pair is similar to ring deformation process, but the orbital motion of the co-rotating vortices cannot be confirmed. The vertical distance is nearer to the beginning, $t^* = 1.1$, then slowly approaches and vortex pair is dissipated. There is a difference in how much the train of vortex ring generated by the linking of the upper vortex interacts with the lower vortex pair.

When $t^* = 0.32$, the variation of vortex spacing of the upper and lower wake vortices progresses slowly and instability due to disturbance perturbation develops. When $t^* = 1.92$, we can confirm the remarkable development of long-wave instability in the upper pair.

The instability develops along a 45-degree incline plane with respect to the horizontal plane, indicating that the strain field of the lower vortex is less affected. When the upper vortex spacing is $0.52b_0$ due to the instability development, the collapse point of the upper vortex pair occurs and linking occurs.

When $t^* = 2.87$, the upper vortex ring was formed, the vortex spacing of the lower pair was increased by 28%, and the instability was slightly

increased. The increase in vortex spacing resulted in a decrease in instability and an increase in the lifespan of the lower vortex pair.

After $t^* = 4.15$, the upper vortex ring is stretched and non-linear interaction begins with the lower vortex pair. In the case of $R_h = 2$ or more and R_Γ less than 1, the vortex lifespan of the upper pair is shortened and the vortex lifespan of the lower vortex becomes longer due to the interaction of 4VVS. After formation of the upper vortex ring, the lower vortex is distorted by non-linear interaction and dissipated.

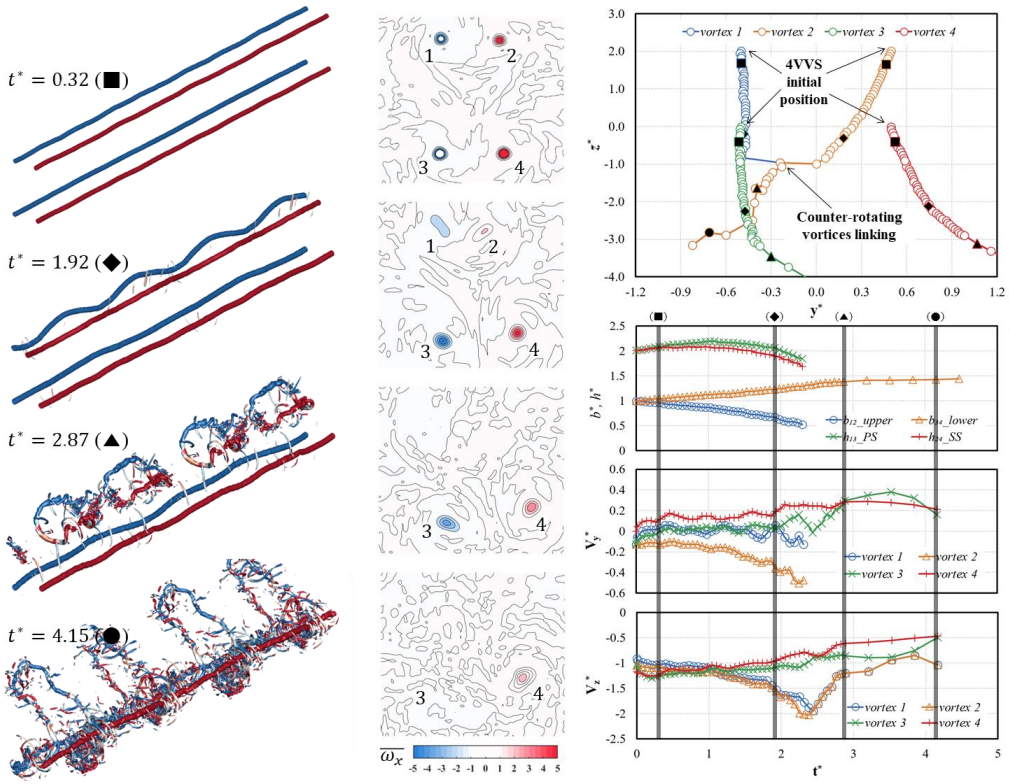

Fig. 4-13 time evolution of Hv20Rg07 ($R_\Gamma = 0.68,\ R_h = 2.0$)

iso-λ_2 surface (left); $\overline{\omega_x}$ contour (middle); and time evolution of vortices core (right)

4.6 Dissipation effects of various V4VS decay processes

The dissipation effect of each decay characteristic process was analyzed by considering the total circulation. Its maximum value for the upper and lower vortex pairs was calculated because the lower pair could also affect the next aircraft. Fig. 4-14 shows the times required to dissipate the total circulation to less than 50% of the initial circulation. A similar trend was observed after over-plotting the criteria for various V4VS decay processes, which were found to have a significant influence on the dissipation effect.

The strongest effect was produced by wrapping followed by merging and ring deformation. Interestingly, the dissipation effects of the Hv15Rg10 and Hv15Rg15 cases produced by ring deformation were relatively small because the vertical distance at the time of linking was large after the reversal of the two pairs. Therefore, the interactions between the upper vortex ring and the lower vortex pair were strong when the vertical distance was around 2.0.

The weakest dissipation effect was produced by parallel dissipation that increased the lifespan of the lower vortex pair by mutual induction; as a result, the vortex dissipation process was the longest one. Clearly, the wake vortex generated by the preceding aircraft can very efficiently destroy the wake vortices of the following aircraft. The dissipation effect is strong when the circulation ratio is greater than 1.0 and the vertical distance is relatively large.

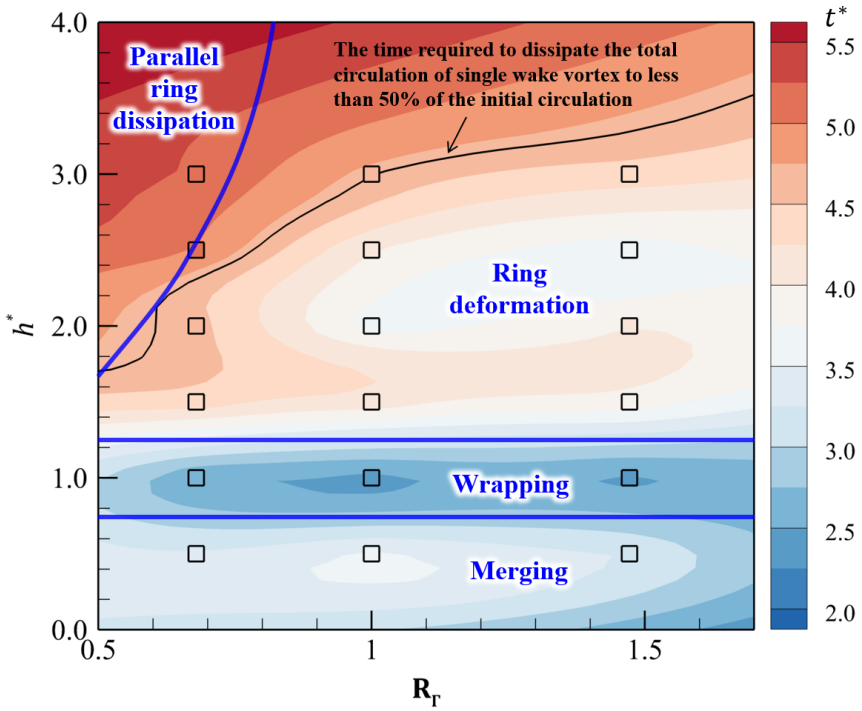

Fig. 4-14 A map of the V4VS transport and decay processes occurring at $\theta = 90°$.

4.7 V4VS efficiency assessment for increasing airport efficiency

The take-off separation time adjustment was investigated by considering the interactions of the vertically arranged wake vortex pairs generated by the preceding and following aircraft. The objective was to determine whether the separation of the next aircraft could be adjusted in the situation where three aircraft took off sequentially (assuming the ideal situation for numerical simulations). The separation adjustment of the next aircraft was deduced from the time required to dissipate the total circulation to less than 50% of the initial circulation. The obtained results were compared with the dissipation time of the single wake vortex depicted by the black line in Fig. 4-14.

The wrapping and ring deformation processes were analyzed, and the representative cases Hv10Rg10 and Hv25Rg15 with excellent vortex dissipation properties were selected. The merging process was excluded because the distance between the aircraft must be extremely close, and parallel ring dissipation was excluded as well because the lifespan of the lower vortex pair increased.

Hv10Rg10 was examined as a representative case of the wrapping process. Here, vortex interactions occur when the following aircraft takes off after 26.3 s on the route taken by the preceding aircraft. It reduces the time required for vortex dissipation by 48% and, therefore, can significantly decrease the separation time. The observed vortex dissipation effect is very strong, but also dangerous because both the preceding and following aircraft are located very close; hence, its practical implementation requires special care.

Hv25Rg15 was analyzed as a representative case of the parallel ring dissipation process. Here, vortex interaction occurs when the large following aircraft takes off 96.8 s after the medium preceding aircraft on the same route. It reduces the dissipation time by 22% and, therefore, may decrease the take-off separation time.

Overall, the dissipation effect is strong during merging, but the ring deformation process is more feasible in terms of safety. In the latter case, not only the distance between the two aircraft is relatively large, but also the following aircraft is more maneuverable because of its bigger size. In addition, higher V4VS efficiency can be achieved by performing the separation adjustment of the following aircraft.

Chapter 5. Conclusion

In this study, various vortex decay characteristic processes were investigated considering the interactions between the wake vortex pairs generated by the preceding and following aircraft. If these interactions promote the dissipation of the latter wake vortices, the take-off separation time for the next aircraft can be reduced in a recursive manner thus increasing the airport capacity limit.

In this study, LES simulation has been performed to examine the interaction of wake vortex pairs. The parameters for wake vortices were based on the classification criteria ruled by ICAO. To simulate atmospheric conditions, isotropic turbulence was generated using SNGR and forcing technique. After generating the background turbulence, wake vortices were added to the flow field to investigate the behavior.

In three cases, which are the combination of 1) light and medium, 2) medium and medium, and 3) medium and heavy aircraft, wake vortices were added to the flow field with time difference and height difference. It was assumed that the wake vortices formed before had been still remained in atmosphere. In all cases, the superposition of the induced effect of each pair of vortices was observed. The upper wake vortices were initially moved toward each other and showed a fast descending speed, while the lower wake vortices were initially spread to both sides and showed a slow descending speed.

It was confirmed that when the upper wake vortices reached the vertical position of lower wake vortices, different results occurred for three cases. In the case of combination light and medium aircraft, the vortices from light

aircraft were rapidly dissipated. In addition, as the vortices from light aircraft interacted with the vortices from medium aircraft, a large number of secondary vortices were generated so that the vortex lifespan shortened. In the medium and medium aircraft case, it was confirmed that the circulation intensity temporarily increased due to the combination of the pair of vortices rotating in the same direction. Then the circulation intensity decreased as the linking happened with the vortices rotating in opposite direction. Finally, it was confirmed that the dissipation of wake vortices from heavy aircraft, which interacted with wake vortices from medium aircraft was 5 times faster than the case of a single pair of wake vortices from heavy aircraft without interaction.

Initial conditions were defined as a V4VS with a high altitude of the following aircraft. A total of 18 different cases with various combinations of the vertical distance and circulation ratio were analyzed. From the obtained results, the following conclusions were drawn.

Four main processes involving non-linear vortex interactions were observed: merging into a single counter-rotating pair, rapid dissipation, and formation of a vortex ring with or without a deformation of the lower vortex pair. These decay characteristic processes were named merging, wrapping, ring deformation, and parallel ring dissipation, respectively. The dissipation effect of each process was examined to determine the corresponding wake turbulence separation.

The wake vortex formed by the preceding aircraft can effectively destroy the wake vortices produced by the following aircraft. The strongest V4VS dissipation effect was achieved by wrapping. The next efficient vortex dissipation process was ring deformation, during which the upper vortex ring interacted with the lower vortex pair.

The effect of vortex dissipation on the take-off separation time was investigated as well. Overall, the dissipation effect was strong during merging; however, ring deformation was more feasible in terms of safety, owing to not only the large distance between the two aircraft, but also to the higher maneuverability of the following aircraft with a size larger than that of the preceding aircraft.

References

[1] D.P. Delisi, M.J. Pruis, D.Y. Lai, F.Y. Wang, Estimates of the initial vortex separation distance, bo, of commercial aircraft from pulsed lidar data, 51st AIAA Aerosp. Sci. Meet. Incl. New Horizons Forum Aerosp. Expo. 2013. (2013) 1–10. doi:10.2514/6.2013-365.

[2] S. Matthews, R.H. Vandel, C.N. Phillips, S.D. Reed, SPECIAL DOUBLE ISSUE Data Show That U . S . Wake-turbulence Accidents Are Most Frequent at Low Altitude and, (2002).

[3] C.J. OConnor, D.K. Rutishauser, Enhanced Airport Capacity Through Safe, Dynamic Reductions in Aircraft Separation: NASA's Aircraft VOrtex Spacing System (AVOSS), (2001).

[4] V.J. Rossow, Wake-vortex separation distances when flight-path corridors are constrained, 14th Appl. Aerodyn. Conf. 33 (1996) 971–980. doi:10.2514/3.46978.

[5] V.T. Frédéric Rooseleer, "RECAT-EU" European Wake Turbulence Categorisation and Separation Minima on Approach and Departure, n.d.

[6] A.C.A. 90-23G FAA, Aircraft Wake Turbulence, (2014) 3–5. doi:10.1177/004728757301200242.

[7] UK Aeronautical Information Services, Aeronautical Information Circular P 092/2017, 2017. http://www.nats-uk.ead-it.com/public/index.php%3Foption=com_content&task=blogcategory&id=161&Itemid=58.html.

[8] G.C. Hay, R.H. Passman, Pilot and air traffic controller guide to wake turbulence, 1995. http://www.faa.gov/training_testing/training/media/wake/04SEC2.PDF.

[9] T. Kolos-Lakatos, R.J. Hansman, A System Level Study of New Wake

Turbulence Separation Concepts and Their Impact on Airport Capacity, (2017). https://dspace.mit.edu/handle/1721.1/108355.

[10] J. Han, Y.-L. Lin, D.G. Schowalter, S.P. Arya, F.H. Proctor, Large eddy simulation of aircraft wake vortices within homogeneous turbulence: Crow instability, AIAA J. 38 (2000) 292–300. doi:10.2514/2.956.

[11] G.F. Switzer, F.H. Proctor, Wake vortex prediction models for decay and transport within stratified environments, 40th AIAA Aerosp. Sci. Meet. Exhib. (2002). doi:10.2514/6.2002-945.

[12] F.H. Proctor, N.N. Ahmad, G.S. Switzer, F.M. Limon Duparcmeur, Three-phased wake vortex decay, AIAA Atmos. Sp. Environ. Conf. 2010. (2010) 1–11. doi:10.2514/6.2010-7991.

[13] I. De Visscher, L. Bricteux, G. Winckelmans, Aircraft vortices in stably stratified and weakly turbulent atmospheres: simulation and modeling, AIAA J. 51 (2013) 551–566. doi:10.2514/1.J051742.

[14] S.C. CROW, Stability theory for a pair of trailing vortices, AIAA J. 8 (1970) 2172–2179. doi:10.2514/3.6083.

[15] S. C. Crow, E. R. Bate, Lifespan of trailing vortices in a turbulent atmosphere, J. Aircr. 13 (1976) 476–482. doi:10.2514/3.44537.

[16] Milton Van Dyke, An Album of Fluid Motion, Parabolic Press, stanford, California, 1982.

[17] F. Holzäpfel, T. Hofbauer, D. Darracq, H. Moet, F. Garnier, C.F. Gago, Analysis of wake vortex decay mechanisms in the atmosphere, Aerosp. Sci. Technol. 7 (2003) 263–275. doi:10.1016/S1270-9638(03)00026-9.

[18] F. Holzäpfel, Probabilistic two-phase wake vortex decay and transport model, J. Aircr. 40 (2003) 323–331. doi:10.2514/2.3096.

[19] A. Stephan, F. Holzäpfel, T. Misaka, Aircraft wake-vortex decay in ground proximity — physical mechanisms and artificial enhancement,

J. Aircr. 50 (2013) 1250–1260. doi:10.2514/1.C032179.

[20] T. Misaka, F. Holzäpfel, I. Hennemann, T. Gerz, M. Manhart, F. Schwertfirm, Vortex bursting and tracer transport of a counter-rotating vortex pair, Phys. Fluids. 24 (2012) 025104. doi:10.1063/1.3684990.

[21] M. Ahmadi-Baloutaki, R. Carriveau, D.S.K. Ting, An experimental study on the interaction between free-stream turbulence and a wing-tip vortex in the near-field, Aerosp. Sci. Technol. 43 (2015) 395–405. doi:10.1016/j.ast.2015.03.021.

[22] C.H.J. Wang, D. Zhao, J. Schlüter, F. Holzäpfel, A. Stephan, LES study on the shape effect of ground obstacles on wake vortex dissipation, Aerosp. Sci. Technol. 63 (2017) 245–258. doi:10.1016/j.ast.2016.12.032.

[23] T. SARPKAYA, J.J. DALY, Effect of ambient turbulence on trailing vortices, J. Aircr. 24 (1987) 399–404. doi:10.2514/3.45459.

[24] F. Holzäpfel, M. Frech, T. Gerz, A. Tafferner, K.-U. Hahn, C. Schwarz, H.-D. Joos, B. Korn, H. Lenz, R. Luckner, G. Höhne, Aircraft wake vortex scenarios simulation package – WakeScene, Aerosp. Sci. Technol. 13 (2009) 1–11. doi:10.1016/j.ast.2007.09.008.

[25] C.W. Schwarz, K.-U. Hahn, Full-flight simulator study for wake vortex hazard area investigation, Aerosp. Sci. Technol. 10 (2006) 136–143. doi:10.1016/j.ast.2005.09.005.

[26] J.N. Hallock, F. Holzäpfel, A review of recent wake vortex research for increasing airport capacity, Prog. Aerosp. Sci. 98 (2018) 27–36. doi:10.1016/j.paerosci.2018.03.003.

[27] C.D. Donaldson, A.J. Bilanin, Vortex wakes of conventional aircraft, Princeton, NJ, 1975. doi:10.1109/ICCSP.2014.6949794.

[28] S.C. Rennich, S.K. Lele, Method for accelerating the destruction of aircraft wake vortices, J. Aircr. 36 (1999) 398–404. doi:10.2514/2.2444.

[29] D. Fabre, L. Jacquin, Stability of a four-vortex aircraft wake model, Phys. Fluids. 12 (2000) 2438–2443. doi:10.1063/1.1289397.

[30] E. Stumpf, Study of four-vortex aircraft wakes and layout of corresponding aircraft configurations, J. Aircr. 42 (2005) 722–730. doi:10.2514/1.7806.

[31] A. Allen, C. Breitsamter, Experimental investigation of counter-rotating four vortex aircraft wake, Aerosp. Sci. Technol. 13 (2009) 114–129. doi:10.1016/j.ast.2008.05.004.

[32] B.M. Babie, R.C. Nelson, An experimental investigation of bending wave instability modes in a generic four-vortex wake, Phys. Fluids. 22 (2010) 1–15. doi:10.1063/1.3456713.

[33] O.A. Elsayed, A.A. Omar, W. Asrar, K. Kwon, Effect of differential spoiler settings (DSS) on the wake vortices of a wing at high-lift-configuration (HLC), Aerosp. Sci. Technol. 15 (2011) 555–566. doi:10.1016/j.ast.2010.11.001.

[34] J.D. Crouch, Instability and transient growth for two trailing-vortex pairs, J. Fluid Mech. 350 (1997) 311–330. doi:10.1017/S0022112097007040.

[35] J.M. Ortega, Stability Characteristics of Counter-Rotating Vortex Pairs in the Wakes of Triangular-Flapped Airfoils, Dr. Philos. Univ. Calif. 91 (2001) 399–404.

[36] R.L. Bristol, J.M. Ortega, P.S. Marcus, Ö. Savaş, On cooperative instabilities of parallel vortex pairs, J. Fluid Mech. 517 (2004) 331–358. doi:10.1017/S0022112004001016.

[37] O. Reynolds, On the Dynamical Theory of Incompressible Viscous Fluids and the Determination of the Criterion, Philos. Trans. R. Soc. London. 186 (1895) 123–164. doi:10.1037/11715-001.

[38] J. SMAGORINSKY, General Circulation Experiments With the Primitive Equations, Mon. Weather Rev. 91 (1963) 99–164.

doi:10.1175/1520-0493(1963)091<0099:gcewtp>2.3.co;2.

[39] F. Proctor, D. Hamilton, J. Han, Wake vortex transport and decay in ground effect - Vortex linking with the ground, in: 38th Aerosp. Sci. Meet. Exhib., American Institute of Aeronautics and Astronautics, Reston, Virigina, 2000. doi:10.2514/6.2000-757.

[40] S. Yamamoto, H. Daiguji, Higher-order-accurate upwind schemes for solving the compressible Euler and Navier-Stokes equations, Comput. Fluids. 22 (1993) 259–270. doi:10.1016/0045-7930(93)90058-H.

[41] W. Bechara, C. Bailly, P. Lafon, S.M. Candel, Stochastic approach to noise modeling for free turbulent flows, AIAA J. 32 (1994) 455–463. doi:10.2514/3.12008.

[42] A. Vincent, M. Meneguzzi, The spatial structure and statistical properties of homogeneous turbulence, J. Fluid Mech. 225 (1991) 1–20. doi:10.1017/S0022112091001957.

[43] D.C. Burnham, J.N. Hallock, Chicago monosctatic acoustic vortex sensing system, volume IV: wake vortex decay, Springfield, Virginia, 1982. https://apps.dtic.mil/dtic/tr/fulltext/u2/a120081.pdf.

[44] T. Gerz, F. Holzäpfel, D. Darracq, Commercial aircraft wake vortices, Prog. Aerosp. Sci. 38 (2002) 181–208. doi:10.1016/S0376-0421(02)00004-0.

[45] I. Hennemann, F. Holzapfel, Large-eddy simulation of aircraft wake vortex deformation and topology, Proc. Inst. Mech. Eng. Part G J. Aerosp. Eng. 225 (2011) 1336–1350. doi:10.1177/0954410011402257.

[46] J. Jeong, F. Hussain, On the identification of a vortex, J. Fluid Mech. 285 (1995) 69. doi:10.1017/S0022112095000462.

[47] F.H. Proctor, D.W. Hamilton, TASS driven algorithms for wake prediction, System. (2006) 1–20. doi:10.2514/6.2006-1073.

[48] S.E. Widnall, D.B. Bliss, C.Y. Tsai, The instability of short waves on a vortex ring, J. Fluid Mech. 66 (1974) 35–47.

doi:10.1017/S0022112074000048.

[49] T. Leweke, C.H.K. Williamson, Cooperative elliptic instability of a vortex pair, J. Fluid Mech. 360 (1998) 85–119. doi:10.1017/S0022112097008331.

[50] T. Leweke, C.H.K. Williamson, Experiments on long-wavelength instability and reconnection of a vortex pair, Phys. Fluids. 23 (2011). doi:10.1063/1.3531720.

[51] R.L. Bristol, J.M. Ortega, O. Savas, Experimental Study of Corotating Wake-Vortex Merger at Reynolds Numbers of Order 105, AIAA J. 41 (2003) 741–744. doi:10.2514/2.2006.

[52] T. Sarpkaya, New Model for Vortex Decay in the Atmosphere, J. Aircr. 37 (2008) 53–61. doi:10.2514/2.2561.

Appendix A. deterministic wake vortex model (DVM) [17]

In the paper of De visscher et al., there is a simplified modeling of wake vortex transport and decay. The modeling of the vortex transport considers the Biot-Savart effect and the stratification as Eq. (A.1).

$$\frac{\boldsymbol{dz^*}}{\boldsymbol{dt^*}} = \boldsymbol{v^*_{BS}} + \boldsymbol{v^*_{str}} \quad \text{(A.1)}$$

Considering the stratification level as zero, the v^*_{str} term can be ignored so the effect of Biot-Savart, v^*_{BS} can only be in effect as Eq. (2.55). In case of the modeling of the vortex circulation decay, De Visscher et al. made an improvement of the model developed by Sarpkaya [52]. Considering the stratification level as zero, the model can be summarized as Eq. (A.2)

$$\frac{\mathrm{d}\Gamma^*_{tot}}{dt^*} = \begin{cases} -\dfrac{c_1}{t^*_{d,S}}\Gamma^*_{tot} & \left(if\ t^* \le t^*_d - \dfrac{\Delta t^*}{2}\right) \\ -\dfrac{c_2}{t^*_{d,S}}\Gamma^*_{tot} & \left(if\ t^* \ge t^*_d - \dfrac{\Delta t^*}{2}\right) \\ \left(\dfrac{1}{2}\left(\dfrac{c_2}{t^*_\Gamma} + \dfrac{c_1}{t^*_{d,S}}\right) + \left(\dfrac{c_2}{t^*_\Gamma} - \dfrac{c_1}{t^*_{d,S}}\right)\dfrac{t^* - t^*_d}{\Delta t^*}\right)\Gamma^*_{tot} & (otherwise) \end{cases} \quad \text{(A.2)}$$

Here, t^*_d is the starting time of the fast-decay phase. It depends on the turbulence and since we do not consider the stratification, $t^*_d = t^*_\Gamma = t^*_{d,S}$.

$t^*_{d,S}$ is from Sarpkaya's model, and it is computed with respect to ε^*. In addition, there is an interval Δt^* for fitting the results better to the model. It can be a ratio of t^*_d. In other words, $\Delta t^* = \alpha t^*_d$, and α is chosen to be 0.15. The fitting of the model on the present results provides $c_1 = 0.035$, and $c_2 = 1.2$.

Appendix B. Vortex parameters raw data for vertical four vortex interaction cases

The transport and decay processes of the V4VS were summarized by studying the evolution of the related wake vortex parameters. In this study, 18 simulation cases with different combinations of the circulation ratio ($R_\Gamma \equiv \Gamma_u/\Gamma_l$) and vertical distance ($h^* \equiv h/b$) are considered. The case names are selected to indicate their parameters. The vortex parameters such as the vertical and lateral positions and circulation were calculated along the core line. Parameters of each vortex were determined by averaging the values obtained for different core segments.

B.1 Hv05Rg10

	upper_starboard				upper_port				lower_starboard				lower_port			
time	y^*	z^*	Γ^*_{max}	Γ^*_{515}	y^*	z^*	Γ^*_{max}	Γ^*_{515}	y^*	z^*	Γ^*_{max}	Γ^*_{515}	y^*	z^*	Γ^*_{max}	Γ^*_{515}
0.0	0.500	0.500	1.876	0.905	-0.500	0.500	1.809	0.891	0.500	0.000	1.888	0.887	-0.500	0.000	1.838	0.894
0.4	0.390	-0.300	1.881	0.870	-0.380	-0.303	1.842	0.861	0.628	-0.622	1.883	0.873	-0.602	-0.631	1.842	0.870
0.8	0.538	-1.171	1.846	0.670	-0.472	-1.195	1.800	0.665								
1.1	0.574	-1.846	1.480	0.465	-0.467	-1.888	1.468	0.467								
1.5	0.616	-2.499	1.233	0.367	-0.429	-2.565	1.187	0.351								
1.9	0.672	-3.119	0.962	0.268	-0.423	-3.183	0.916	0.261								
2.3	0.724	-3.670	0.782	0.221	-0.399	-3.759	0.781	0.219								
2.7	0.794	-4.191	0.690	0.206	-0.339	-4.314	0.705	0.210								
3.0	0.874	-4.640	0.594	0.200	-0.384	-4.768	0.591	0.198								
3.4	0.908	-5.207	0.450	0.190	-0.249	-5.336	0.500	0.199								
3.8	0.971	-5.681	0.458	0.191	-0.204	-5.852	0.413	0.200								
4.2	1.099	-6.135	0.406	0.192	-0.146	-6.328	0.424	0.183								
4.6	1.204	-6.512	0.347	0.170	-0.067	-6.754	0.394	0.160								
4.9	1.289	-6.873	0.313	0.151	-0.094	-7.090	0.349	0.125								
5.3	1.357	-7.163	0.286	0.135	-0.116	-7.359	0.312	0.097								

B.2 Hv10Rg10

	upper_starboard				upper_port				lower_starboard				lower_port			
time	y^*	z^*	Γ^*_{max}	Γ^*_{515}	y^*	z^*	Γ^*_{max}	Γ^*_{515}	y^*	z^*	Γ^*_{max}	Γ^*_{515}	y^*	z^*	Γ^*_{max}	Γ^*_{515}
0.0	0.500	1.000	0.969	0.899	-0.500	1.000	0.927	0.884	0.500	0.000	0.964	0.884	-0.500	0.000	0.939	0.881
0.4	0.297	0.244	0.961	0.893	-0.307	0.253	0.942	0.887	0.714	-0.408	1.006	0.895	-0.693	-0.418	0.973	0.887
0.8	0.308	-1.219	0.936	0.854	-0.322	-1.217	0.919	0.850	0.712	-0.520	0.976	0.860	-0.661	-0.543	0.952	0.855
1.1	0.501	-1.938	0.937	0.747	-0.554	-1.906	0.912	0.732	0.536	-0.936	0.960	0.756	-0.431	-1.032	0.931	0.752
1.5	0.666	-2.389	0.859	0.578	-0.780	-2.185	0.871	0.545	0.432	-1.614	0.926	0.586	-0.172	-1.943	0.906	0.578
1.9	0.856	-2.707	0.641	0.413	-0.678	-2.307	0.745	0.382	0.504	-2.516	0.631	0.424	-0.081	-3.058	0.717	0.420
2.3	0.882	-2.995	0.566	0.284	-0.571	-2.653	0.475	0.231	0.382	-3.151	0.530	0.336	0.006	-3.745	0.565	0.315
2.7	0.786	-3.230	0.526	0.241	-0.476	-3.081	0.423	0.223	-0.032	-4.302	0.467	0.223	-0.032	-4.302	0.467	0.223
3.0	0.883	-3.576	0.518	0.212	-0.536	-3.358	0.376	0.198	0.720	-4.536	0.409	0.150	0.720	-4.536	0.409	0.150
3.4	1.006	-3.652	0.434	0.198	-0.610	-3.546	0.358	0.189	0.442	-5.014	0.361	0.149	0.442	-5.014	0.361	0.149
3.8	1.027	-3.962	0.341	0.161	-0.734	-3.627	0.321	0.159	0.024	-5.731	0.290	0.148	0.024	-5.731	0.290	0.148
4.2	1.030	-4.065	0.255	0.122	-0.839	-3.851	0.331	0.139								
4.6	0.955	-4.267	0.274	0.074	-0.835	-3.982	0.264	0.134								
4.9					-0.771	-4.007	0.291	0.113								
5.3					-0.849	-4.055	0.248	0.106								

B.3 Hv15Rg10

	upper_starboard				upper_port				lower_starboard				lower_port			
time	y^*	z^*	Γ^*_{max}	Γ^*_{515}	y^*	z^*	Γ^*_{max}	Γ^*_{515}	y^*	z^*	Γ^*_{max}	Γ^*_{515}	y^*	z^*	Γ^*_{max}	Γ^*_{515}
0.0	0.500	1.500	0.978	0.890	-0.500	1.500	0.960	0.885	0.500	0.000	0.962	0.883	-0.500	0.000	0.940	0.880
0.4	0.414	0.980	0.974	0.896	-0.447	0.997	0.973	0.897	0.588	-0.433	0.979	0.896	-0.564	-0.438	0.952	0.888
0.8	0.298	0.310	0.967	0.889	-0.374	0.350	0.967	0.889	0.704	-0.798	0.983	0.889	-0.638	-0.830	0.954	0.882
1.1	0.114	-0.829	0.928	0.820	-0.291	-0.687	0.912	0.803	0.855	-1.002	1.000	0.839	-0.762	-1.150	0.925	0.832
1.5	-0.358	-2.078	0.717	0.491	-0.353	-2.159	0.679	0.528	0.792	-1.156	0.957	0.693	-0.650	-1.313	0.830	0.663
1.9	-0.748	-2.522	0.566	0.340	-0.748	-2.522	0.566	0.340	0.769	-1.419	0.931	0.535	-0.609	-1.858	0.682	0.391
2.3	-0.857	-3.192	0.517	0.214	-0.857	-3.192	0.517	0.214	0.787	-1.669	0.874	0.423	-0.664	-2.223	0.642	0.321
2.7	-1.350	-3.282	0.439	0.177	-1.350	-3.282	0.439	0.177	0.829	-1.895	0.804	0.355	-0.710	-2.494	0.552	0.264
3.0	-1.520	-3.403	0.406	0.132	-1.520	-3.403	0.406	0.132	0.881	-2.097	0.754	0.304	-0.733	-2.714	0.512	0.205
3.4	-1.843	-3.922	0.410	0.129	-1.843	-3.922	0.410	0.129	0.948	-2.287	0.688	0.265	-0.731	-2.907	0.515	0.191
3.8	-2.004	-4.434	0.364	0.110	-2.004	-4.434	0.364	0.110	1.005	-2.465	0.611	0.238	-0.731	-3.079	0.431	0.175
4.2	-2.227	-4.499	0.360	0.119	-2.227	-4.499	0.360	0.119	1.050	-2.646	0.558	0.222	-0.711	-3.244	0.394	0.136
4.6	-2.563	-4.598	0.271	0.149	-2.563	-4.598	0.271	0.149	1.114	-2.824	0.547	0.196	-0.695	-3.402	0.369	0.123
4.9	-2.626	-4.843	0.274	0.121	-2.626	-4.843	0.274	0.121	1.173	-2.967	0.511	0.181	-0.687	-3.550	0.320	0.083
5.3	-2.721	-5.212	0.297	0.143	-2.721	-5.212	0.297	0.143	1.219	-3.110	0.458	0.169	-0.680	-3.675	0.310	0.092

B.4 Hv20Rg10

	upper_starboard				upper_port				lower_starboard				lower_port			
time	y^*	z^*	Γ^*_{max}	Γ^*_{515}	y^*	z^*	Γ^*_{max}	Γ^*_{515}	y^*	z^*	Γ^*_{max}	Γ^*_{515}	y^*	z^*	Γ^*_{max}	Γ^*_{515}
0.0	0.500	2.000	0.973	0.897	-0.500	2.000	0.987	0.900	0.500	0.000	0.960	0.883	-0.500	0.000	0.938	0.880
0.4	0.456	1.532	0.973	0.898	-0.490	1.557	0.997	0.903	0.541	-0.414	0.968	0.895	-0.521	-0.417	0.945	0.888
0.8	0.403	1.032	0.965	0.897	-0.473	1.078	0.987	0.903	0.602	-0.803	0.971	0.895	-0.539	-0.819	0.943	0.887
1.1	0.332	0.479	0.957	0.887	-0.453	0.548	0.978	0.894	0.672	-1.160	0.965	0.883	-0.557	-1.210	0.939	0.878
1.5	0.226	-0.182	0.947	0.840	-0.442	-0.072	0.965	0.845	0.757	-1.476	0.959	0.836	-0.573	-1.586	0.938	0.829
1.9	0.043	-1.085	0.868	0.704	-0.483	-0.847	0.844	0.679	0.888	-1.709	0.956	0.717	-0.602	-1.956	0.931	0.710
2.3	0.021	-2.170	0.723	0.497	-0.583	-2.493	0.740	0.454	0.924	-1.808	0.937	0.560	-0.626	-1.592	0.683	0.465
2.7	-0.281	-3.195	0.494	0.313	-0.281	-3.195	0.494	0.313	0.831	-2.003	0.852	0.425	-0.649	-1.911	0.558	0.303
3.0	-0.081	-3.873	0.368	0.213	-0.081	-3.873	0.368	0.213	0.767	-2.288	0.737	0.333	-0.606	-2.258	0.516	0.197
3.4	-0.066	-4.297	0.333	0.153	-0.066	-4.297	0.333	0.153	0.731	-2.602	0.658	0.278	-0.575	-2.594	0.392	0.170
3.8	-0.051	-4.679	0.331	0.153	-0.051	-4.679	0.331	0.153	0.713	-2.907	0.528	0.222	-0.636	-2.993	0.367	0.152
4.2	0.076	-5.062	0.278	0.177	0.076	-5.062	0.278	0.177	0.684	-3.203	0.454	0.190	-0.689	-3.276	0.397	0.147
4.6									0.660	-3.473	0.402	0.180	-0.626	-3.544	0.378	0.142
4.9									0.665	-3.747	0.349	0.173	-0.633	-3.913	0.358	0.127
5.3									0.654	-3.987	0.331	0.207	-0.589	-4.135	0.321	0.113

B.5 Hv25Rg10

	upper_starboard				upper_port				lower_starboard				lower_port			
time	y^*	z^*	Γ^*_{max}	Γ^*_{515}	y^*	z^*	Γ^*_{max}	Γ^*_{515}	y^*	z^*	Γ^*_{max}	Γ^*_{515}	y^*	z^*	Γ^*_{max}	Γ^*_{515}
0.0	0.500	2.500	0.977	0.889	-0.500	2.500	0.980	0.899	0.500	0.000	0.953	0.882	-0.500	0.000	0.940	0.888
0.4	0.470	2.060	0.975	0.896	-0.482	2.073	1.013	0.902	0.524	-0.400	0.969	0.896	-0.509	-0.401	0.946	0.888
0.8	0.446	1.600	0.963	0.895	-0.476	1.630	1.003	0.900	0.558	-0.787	0.969	0.894	-0.505	-0.800	0.942	0.886
1.1	0.413	1.130	0.958	0.893	-0.480	1.175	0.996	0.900	0.601	-1.160	0.965	0.892	-0.498	-1.194	0.938	0.884
1.5	0.361	0.634	0.952	0.879	-0.484	0.706	0.988	0.886	0.646	-1.516	0.963	0.878	-0.488	-1.581	0.935	0.869
1.9	0.296	0.098	0.939	0.826	-0.495	0.200	0.978	0.833	0.710	-1.855	0.957	0.828	-0.486	-1.958	0.934	0.818
2.3	0.203	-0.494	0.910	0.705	-0.526	-0.342	0.953	0.709	0.784	-2.166	0.951	0.714	-0.485	-2.318	0.924	0.708
2.7	0.060	-1.164	0.806	0.552	-0.600	-0.936	0.794	0.532	0.888	-2.439	0.937	0.581	-0.473	-2.660	0.892	0.571
3.0	-0.004	-1.880	0.713	0.471	-0.769	-1.453	0.688	0.470	1.003	-2.644	0.888	0.457	-0.435	-2.996	0.850	0.457
3.4	-0.485	-2.360	0.560	0.363	-0.485	-2.360	0.560	0.363	1.093	-2.774	0.789	0.367	-0.295	-3.342	0.713	0.373
3.8	-0.439	-2.840	0.482	0.253	-0.439	-2.840	0.482	0.253	1.124	-2.879	0.724	0.297	-0.029	-3.811	0.452	0.303
4.2									1.121	-3.055	0.569	0.231				
4.6									1.157	-3.240	0.508	0.191				
4.9									1.204	-3.405	0.417	0.169				
5.3									1.197	-3.526	0.301	0.151				

B.6 Hv30Rg10

	upper_starboard				upper_port				lower_starboard				lower_port			
time	y^*	z^*	Γ^*_{max}	Γ^*_{515}	y^*	z^*	Γ^*_{max}	Γ^*_{515}	y^*	z^*	Γ^*_{max}	Γ^*_{515}	y^*	z^*	Γ^*_{max}	Γ^*_{515}
0.0	0.500	3.000	0.982	0.897	-0.500	3.000	0.966	0.894	0.500	0.000	0.962	0.883	-0.500	0.000	0.940	0.880
0.4	0.485	2.589	0.975	0.887	-0.462	2.593	1.001	0.889	0.517	-0.389	0.976	0.887	-0.499	-0.390	0.959	0.879
0.8	0.476	2.154	0.977	0.880	-0.438	2.154	0.998	0.881	0.539	-0.774	0.974	0.879	-0.487	-0.784	0.954	0.873
1.1	0.463	1.707	0.977	0.882	-0.434	1.700	0.994	0.882	0.572	-1.152	0.974	0.880	-0.463	-1.184	0.949	0.870
1.5	0.452	1.248	0.969	0.890	-0.426	1.245	0.987	0.891	0.603	-1.517	0.969	0.886	-0.453	-1.570	0.943	0.878
1.9	0.434	0.779	0.971	0.875	-0.425	0.791	0.983	0.877	0.645	-1.876	0.971	0.871	-0.444	-1.955	0.944	0.860
2.3	0.405	0.293	0.981	0.808	-0.422	0.317	0.979	0.806	0.689	-2.221	0.971	0.803	-0.440	-2.328	0.942	0.791
2.7	0.373	-0.218	0.971	0.669	-0.427	-0.174	0.965	0.666	0.744	-2.554	0.962	0.670	-0.436	-2.675	0.929	0.661
3.0	0.333	-0.762	0.905	0.502	-0.428	-0.702	0.870	0.503	0.811	-2.862	0.939	0.530	-0.445	-3.006	0.906	0.523
3.4	0.274	-1.368	0.646	0.321	-0.452	-1.282	0.584	0.325	0.892	-3.147	0.875	0.425	-0.455	-3.297	0.863	0.419
3.8	0.243	-1.833	0.292	0.090	-0.481	-1.653	0.375	0.118	0.987	-3.392	0.772	0.347	-0.465	-3.571	0.781	0.339
4.2									1.086	-3.593	0.648	0.288	-0.452	-3.819	0.663	0.285
4.6									1.178	-3.754	0.557	0.240	-0.405	-4.092	0.516	0.227
4.9									1.238	-3.893	0.492	0.210	-0.342	-4.376	0.435	0.183
5.3									1.309	-4.050	0.443	0.169	-0.316	-4.736	0.280	0.048

B.7 Hv05Rg15

	upper_starboard				upper_port				lower_starboard				lower_port			
time	y^*	z^*	Γ^*_{max}	Γ^*_{515}	y^*	z^*	Γ^*_{max}	Γ^*_{515}	y^*	z^*	Γ^*_{max}	Γ^*_{515}	y^*	z^*	Γ^*_{max}	Γ^*_{515}
0.0	0.500	0.500	1.607	0.900	-0.500	0.500	1.510	0.892	0.500	0.000	2.330	0.886	-0.500	0.000	2.248	0.881
0.4	0.512	-0.470	1.592	0.885	-0.500	-0.475	1.555	0.882	0.476	-0.035	2.314	0.846	-0.477	-0.038	2.270	0.833
0.8	0.468	-0.811	1.492	0.840	-0.430	-0.835	1.465	0.851	0.651	-1.135	1.970	0.523	-0.609	-1.126	2.049	0.485
1.1	0.539	-1.507	1.390	0.711	-0.441	-1.550	1.349	0.731								
1.5	0.602	-2.067	1.246	0.578	-0.425	-2.130	1.232	0.589								
1.9	0.642	-2.600	1.104	0.450	-0.417	-2.693	1.099	0.468								
2.3	0.692	-3.095	0.976	0.355	-0.420	-3.195	0.992	0.393								
2.7	0.748	-3.544	0.874	0.300	-0.401	-3.642	0.898	0.329								
3.0	0.792	-3.970	0.747	0.260	-0.378	-4.082	0.784	0.275								
3.4	0.839	-4.382	0.654	0.226	-0.361	-4.499	0.590	0.176								
3.8	0.882	-4.772	0.514	0.138	-0.316	-4.886	0.571	0.137								
4.2	0.935	-5.164	0.533	0.148	-0.287	-5.278	0.512	0.168								
4.6	0.980	-5.539	0.517	0.147	-0.247	-5.654	0.496	0.153								
4.9	1.028	-5.900	0.474	0.128	-0.196	-6.082	0.405	0.076								
5.3	1.106	-6.288	0.379	0.067	-0.170	-6.464	0.403	0.109								

B.8 Hv10Rg15

	upper_starboard				upper_port				lower_starboard				lower_port			
time	y^*	z^*	Γ^*_{max}	Γ^*_{515}	y^*	z^*	Γ^*_{max}	Γ^*_{515}	y^*	z^*	Γ^*_{max}	Γ^*_{515}	y^*	z^*	Γ^*_{max}	Γ^*_{515}
0.0	0.500	1.000	0.959	0.898	-0.500	1.000	0.919	0.880	0.500	0.000	0.941	0.876	-0.500	0.000	0.932	0.885
0.4	0.349	0.387	0.966	0.895	-0.367	0.392	0.949	0.889	0.723	-0.316	0.972	0.894	-0.705	-0.326	0.958	0.883
0.8	0.306	-0.739	0.952	0.877	-0.308	-0.730	0.935	0.871	0.813	-0.293	0.966	0.876	-0.786	-0.314	0.939	0.866
1.1	0.468	-1.468	0.956	0.827	-0.464	-1.463	0.929	0.815	0.589	-0.524	0.958	0.829	-0.517	-0.587	0.912	0.819
1.5	0.593	-1.932	0.927	0.700	-0.588	-1.908	0.896	0.679	0.442	-0.973	0.935	0.710	-0.295	-1.133	0.901	0.692
1.9	0.703	-2.306	0.862	0.535	-0.698	-2.156	0.856	0.523	0.392	-1.631	0.809	0.492	-0.060	-2.042	0.718	0.496
2.3	0.835	-2.594	0.665	0.365	-0.626	-2.358	0.746	0.390	0.511	-2.308	0.808	0.323	0.079	-3.041	0.583	0.325
2.7	0.922	-2.871	0.493	0.278	-0.557	-2.695	0.588	0.283								
3.0	1.001	-3.043	0.425	0.169	-0.574	-3.009	0.468	0.218								
3.4	1.094	-3.200	0.382	0.154	-0.596	-3.243	0.392	0.186								
3.8	0.981	-3.505	0.278	0.154	-0.611	-3.468	0.344	0.188								
4.2	0.991	-3.678	0.255	0.126	-0.588	-3.659	0.275	0.164								
4.6	1.035	-3.876	0.245	0.125	-0.586	-3.871	0.290	0.140								
4.9	1.056	-4.083	0.255	0.137	-0.583	-4.088	0.241	0.135								
5.3	1.054	-4.335	0.217	0.127	-0.555	-4.281	0.241	0.105								

B.9 Hv15Rg15

	upper_starboard				upper_port				lower_starboard				lower_port			
time	y^*	z^*	Γ^*_{max}	Γ^*_{515}	y^*	z^*	Γ^*_{max}	Γ^*_{515}	y^*	z^*	Γ^*_{max}	Γ^*_{515}	y^*	z^*	Γ^*_{max}	Γ^*_{515}
0.0	0.500	1.500	1.000	0.906	-0.500	1.500	1.000	0.906	0.500	0.000	0.952	0.878	-0.500	0.000	0.928	0.873
0.4	0.433	1.031	0.976	0.896	-0.473	1.047	0.975	0.897	0.589	-0.326	0.976	0.896	-0.577	-0.331	0.945	0.884
0.8	0.342	0.453	0.969	0.894	-0.412	0.487	0.968	0.894	0.735	-0.608	0.977	0.887	-0.663	-0.626	0.938	0.883
1.1	0.203	-0.419	0.953	0.876	-0.327	-0.320	0.951	0.873	0.904	-0.719	0.972	0.880	-0.824	-0.842	0.972	0.869
1.5	0.151	-1.576	0.929	0.758	-0.458	-1.508	0.923	0.753	0.841	-0.733	0.961	0.805	-0.762	-0.818	0.970	0.774
1.9	-0.251	-2.186	0.679	0.629	-0.251	-2.186	0.679	0.629	0.753	-0.917	0.952	0.659	-0.563	-1.176	0.924	0.599
2.3	-0.499	-2.658	0.569	0.368	-0.499	-2.658	0.569	0.368	0.720	-1.136	0.927	0.529	-0.520	-1.591	0.658	0.367
2.7	-0.627	-3.184	0.541	0.231	-0.627	-3.184	0.541	0.231	0.738	-1.347	0.890	0.437	-0.504	-1.879	0.604	0.305
3.0	-0.776	-3.595	0.488	0.198	-0.776	-3.595	0.488	0.198	0.785	-1.536	0.815	0.362	-0.492	-2.107	0.563	0.282
3.4	-0.920	-4.076	0.465	0.204	-0.920	-4.076	0.465	0.204	0.846	-1.698	0.690	0.294	-0.445	-2.302	0.535	0.237
3.8	-1.066	-4.530	0.446	0.159	-1.066	-4.530	0.446	0.159	0.927	-1.852	0.634	0.262	-0.416	-2.499	0.495	0.220
4.2	-1.174	-4.915	0.413	0.107	-1.174	-4.915	0.413	0.107	0.992	-1.996	0.541	0.231	-0.365	-2.664	0.492	0.205
4.6	-1.388	-5.246	0.343	0.059	-1.388	-5.246	0.343	0.059	1.071	-2.152	0.489	0.197	-0.370	-2.834	0.328	0.060
4.9	-1.536	-5.599	0.309	0.084	-1.536	-5.599	0.309	0.084	1.135	-2.295	0.457	0.178	-0.392	-3.053	0.331	0.052
5.3	-1.681	-5.910	0.273	0.043	-1.681	-5.910	0.273	0.043	1.202	-2.430	0.444	0.173	-0.328	-3.196	0.354	0.051

B.10 Hv20Rg15

	upper_starboard				upper_port				lower_starboard				lower_port			
time	y^*	z^*	Γ^*_{max}	Γ^*_{515}	y^*	z^*	Γ^*_{max}	Γ^*_{515}	y^*	z^*	Γ^*_{max}	Γ^*_{515}	y^*	z^*	Γ^*_{max}	Γ^*_{515}
0.0	0.500	2.000	0.973	0.897	-0.500	2.000	0.987	0.900	0.500	0.000	0.948	0.878	-0.500	0.000	0.926	0.873
0.4	0.465	1.560	0.974	0.897	-0.502	1.585	0.999	0.902	0.541	-0.302	0.963	0.894	-0.531	-0.303	0.935	0.883
0.8	0.422	1.098	0.967	0.894	-0.489	1.142	0.989	0.902	0.607	-0.589	0.958	0.893	-0.557	-0.600	0.926	0.881
1.1	0.359	0.592	0.959	0.895	-0.474	0.655	0.981	0.899	0.694	-0.852	0.959	0.892	-0.589	-0.890	0.921	0.881
1.5	0.257	-0.027	0.950	0.881	-0.449	0.081	0.972	0.887	0.815	-1.066	0.949	0.879	-0.643	-1.179	0.913	0.867
1.9	0.085	-0.893	0.924	0.816	-0.463	-0.653	0.933	0.814	0.950	-1.144	0.949	0.823	-0.746	-1.460	0.911	0.804
2.3	-0.373	-1.625	0.782	0.617	-0.373	-1.625	0.782	0.617	0.905	-1.173	0.926	0.680	-0.849	-1.613	0.905	0.614
2.7	-0.492	-2.367	0.624	0.437	-0.492	-2.367	0.624	0.437	0.852	-1.309	0.862	0.525	-0.767	-1.677	0.678	0.424
3.0	-0.598	-3.308	0.556	0.338	-0.598	-3.308	0.556	0.338	0.841	-1.467	0.769	0.419	-0.841	-1.890	0.642	0.311
3.4	-0.831	-3.689	0.535	0.271	-0.831	-3.689	0.535	0.271	0.860	-1.614	0.713	0.337	-0.870	-2.072	0.527	0.248
3.8	-1.154	-4.049	0.506	0.200	-1.154	-4.049	0.506	0.200	0.880	-1.761	0.661	0.289	-0.889	-2.337	0.459	0.234
4.2	-1.263	-4.513	0.442	0.160	-1.263	-4.513	0.442	0.160	0.921	-1.891	0.586	0.252	-0.877	-2.424	0.413	0.165
4.6	-1.201	-4.804	0.393	0.120	-1.201	-4.804	0.393	0.120	0.921	-2.167	0.514	0.167	-0.883	-2.699	0.369	0.104
4.9									0.921	-2.422	0.417	0.139	-0.905	-2.913	0.297	0.071
5.3									0.921	-2.634	0.375	0.083	-0.864	-3.142	0.248	0.042

B.11 Hv25Rg15

	upper_starboard				upper_port				lower_starboard				lower_port			
time	y^*	z^*	Γ^*_{max}	Γ^*_{515}	y^*	z^*	Γ^*_{max}	Γ^*_{515}	y^*	z^*	Γ^*_{max}	Γ^*_{515}	y^*	z^*	Γ^*_{max}	Γ^*_{515}
0.0	0.500	2.500	0.977	0.889	-0.500	2.500	0.980	0.899	0.500	0.000	0.938	0.875	-0.500	0.000	0.931	0.884
0.4	0.474	2.079	0.976	0.895	-0.489	2.091	1.015	0.901	0.522	-0.283	0.965	0.895	-0.510	-0.286	0.936	0.884
0.8	0.461	1.641	0.964	0.891	-0.490	1.670	1.006	0.897	0.558	-0.565	0.957	0.891	-0.506	-0.574	0.928	0.880
1.1	0.426	1.196	0.959	0.890	-0.492	1.240	0.996	0.895	0.605	-0.838	0.956	0.888	-0.515	-0.857	0.920	0.879
1.5	0.375	0.722	0.953	0.888	-0.492	0.793	0.989	0.896	0.665	-1.090	0.948	0.889	-0.526	-1.141	0.915	0.877
1.9	0.306	0.198	0.944	0.876	-0.496	0.305	0.983	0.886	0.742	-1.327	0.947	0.878	-0.541	-1.423	0.908	0.864
2.3	0.197	-0.411	0.930	0.833	-0.520	-0.237	0.966	0.839	0.849	-1.526	0.939	0.840	-0.559	-1.704	0.903	0.820
2.7	0.041	-1.137	0.890	0.727	-0.585	-0.823	0.917	0.707	0.970	-1.632	0.929	0.745	-0.575	-2.012	0.887	0.726
3.0	-0.043	-1.894	0.782	0.504	-0.706	-1.298	0.732	0.412	0.994	-1.642	0.896	0.582	-0.540	-2.408	0.802	0.547
3.4	0.086	-2.533	0.381	0.224	-0.753	-1.695	0.558	0.227	0.912	-1.704	0.812	0.428	-0.373	-2.783	0.509	0.383
3.8	0.169	-3.269	0.299	0.183	-0.834	-1.920	0.415	0.193	0.822	-1.856	0.741	0.341	-0.110	-3.244	0.399	0.197
4.2																
4.6																
4.9																
5.3																

B.12 Hv30Rg15

	upper_starboard				upper_port				lower_starboard				lower_port			
time	y^*	z^*	Γ^*_{max}	Γ^*_{515}	y^*	z^*	Γ^*_{max}	Γ^*_{515}	y^*	z^*	Γ^*_{max}	Γ^*_{515}	y^*	z^*	Γ^*_{max}	Γ^*_{515}
0.0	0.500	3.000	0.982	0.897	-0.500	3.000	0.966	0.894	0.500	0.000	0.951	0.878	-0.500	0.000	0.928	0.873
0.4	0.489	2.604	0.975	0.885	-0.460	2.603	1.000	0.886	0.514	-0.270	0.978	0.885	-0.498	-0.272	0.953	0.875
0.8	0.484	2.182	0.980	0.866	-0.441	2.185	0.998	0.867	0.540	-0.543	0.969	0.869	-0.490	-0.549	0.948	0.860
1.1	0.469	1.755	0.980	0.856	-0.438	1.746	0.995	0.858	0.564	-0.809	0.965	0.860	-0.486	-0.827	0.939	0.853
1.5	0.458	1.309	0.982	0.859	-0.434	1.308	0.992	0.861	0.602	-1.073	0.966	0.863	-0.479	-1.106	0.931	0.853
1.9	0.436	0.853	0.976	0.875	-0.429	0.865	0.990	0.877	0.646	-1.328	0.961	0.874	-0.476	-1.384	0.924	0.859
2.3	0.409	0.372	0.963	0.881	-0.422	0.397	0.970	0.879	0.694	-1.577	0.952	0.874	-0.479	-1.660	0.914	0.852
2.7	0.365	-0.149	0.974	0.844	-0.414	-0.106	0.970	0.834	0.760	-1.815	0.960	0.839	-0.490	-1.933	0.917	0.811
3.0	0.303	-0.736	0.962	0.721	-0.410	-0.658	0.930	0.711	0.853	-2.021	0.953	0.741	-0.518	-2.204	0.924	0.718
3.4	0.260	-1.399	0.674	0.377	-0.446	-1.254	0.664	0.368	0.967	-2.174	0.945	0.583	-0.571	-2.473	0.899	0.562
3.8	0.234	-1.892	0.377	0.151	-0.446	-1.699	0.346	0.087	1.050	-2.240	0.839	0.432	-0.657	-2.740	0.790	0.381
4.2									1.034	-2.291	0.665	0.290	-0.700	-2.898	0.563	0.222
4.6									0.961	-2.429	0.558	0.186	-0.728	-2.976	0.428	0.153
4.9									0.930	-2.592	0.465	0.174	-0.749	-2.837	0.338	0.111
5.3									0.943	-2.696	0.417	0.153	-0.762	-3.266	0.319	0.083

B.13 Hv05Rg07

	upper_starboard				upper_port				lower_starboard				lower_port			
time	y^*	z^*	Γ^*_{max}	Γ^*_{515}	y^*	z^*	Γ^*_{max}	Γ^*_{515}	y^*	z^*	Γ^*_{max}	Γ^*_{515}	y^*	z^*	Γ^*_{max}	Γ^*_{515}
0.0	0.500	0.500	2.296	0.910	-0.500	0.500	2.198	0.889	0.500	0.000	1.587	0.886	-0.500	0.000	1.537	0.892
0.3	0.514	-0.668	2.287	0.846	-0.489	-0.675	2.225	0.842	0.503	-0.227	1.600	0.886	-0.494	-0.231	1.558	0.877
0.6	0.421	-0.735	1.957	0.531	-0.366	-0.788	2.032	0.461	0.593	-1.094	1.428	0.819	-0.524	-1.079	1.438	0.801
1.0									0.565	-1.536	1.372	0.689	-0.474	-1.566	1.344	0.694
1.3									0.591	-2.096	1.224	0.571	-0.439	-2.161	1.180	0.555
1.6									0.644	-2.614	1.098	0.446	-0.426	-2.704	1.062	0.429
1.9									0.692	-3.124	0.963	0.362	-0.418	-3.200	0.940	0.349
2.2									0.747	-3.563	0.844	0.302	-0.414	-3.662	0.806	0.292
2.6									0.802	-3.974	0.766	0.249	-0.378	-4.082	0.677	0.254
2.9									0.846	-4.374	0.637	0.224	-0.365	-4.489	0.585	0.224
3.2									0.907	-4.755	0.556	0.209	-0.313	-4.863	0.492	0.211
3.5									0.969	-5.118	0.524	0.212	-0.263	-5.236	0.453	0.196
3.8									1.030	-5.464	0.475	0.209	-0.217	-5.619	0.440	0.172
4.2									1.076	-5.807	0.431	0.203	-0.157	-6.001	0.375	0.174
4.5									1.178	-6.109	0.370	0.204	-0.109	-6.350	0.317	0.151

B.14 Hv10Rg07

	upper_starboard				upper_port				lower_starboard				lower_port			
time	y^*	z^*	Γ^*_{max}	Γ^*_{515}	y^*	z^*	Γ^*_{max}	Γ^*_{515}	y^*	z^*	Γ^*_{max}	Γ^*_{515}	y^*	z^*	Γ^*_{max}	Γ^*_{515}
0.0	0.500	1.000	0.960	0.899	-0.500	1.000	0.905	0.873	0.500	0.000	0.955	0.882	-0.500	0.000	0.940	0.888
0.3	0.313	0.449	0.959	0.894	-0.330	0.458	0.930	0.884	0.631	-0.412	0.978	0.895	-0.610	-0.409	0.951	0.888
0.6	0.152	-0.771	0.890	0.800	-0.174	-0.747	0.889	0.794	0.749	-0.622	0.947	0.877	-0.703	-0.651	0.934	0.872
1.0	0.296	-1.816	0.908	0.781	-0.419	-1.780	0.884	0.747	0.644	-0.876	0.974	0.803	-0.542	-0.947	0.941	0.796
1.3	0.398	-2.347	0.874	0.632	-0.680	-2.190	0.826	0.566	0.581	-1.275	0.963	0.678	-0.389	-1.467	0.932	0.668
1.6	0.426	-2.767	0.769	0.490	-0.864	-2.288	0.588	0.348	0.567	-1.733	0.930	0.536	-0.280	-2.182	0.886	0.502
1.9	0.315	-3.175	0.596	0.369	-0.742	-2.265	0.531	0.232	0.617	-2.178	0.729	0.453	-0.442	-2.893	0.759	0.383
2.2	0.253	-3.340	0.361	0.222	-0.709	-2.493	0.441	0.161	0.704	-2.574	0.619	0.340	-0.601	-3.189	0.529	0.300
2.6									0.821	-2.854	0.491	0.280	-0.563	-3.602	0.363	0.180
2.9									0.933	-2.948	0.404	0.170	-0.803	-3.280	0.226	0.075
3.2																
3.5																
3.8																
4.2																
4.5																

B.15 Hv15Rg07

	upper_starboard				upper_port				lower_starboard				lower_port			
time	y^*	z^*	Γ^*_{max}	Γ^*_{515}	y^*	z^*	Γ^*_{max}	Γ^*_{515}	y^*	z^*	Γ^*_{max}	Γ^*_{515}	y^*	z^*	Γ^*_{max}	Γ^*_{515}
0.0	0.500	1.500	0.979	0.887	-0.500	1.500	0.951	0.881	0.500	0.000	0.962	0.883	-0.500	0.000	0.940	0.880
0.3	0.421	1.118	0.974	0.894	-0.460	1.137	0.969	0.895	0.556	-0.408	0.979	0.897	-0.536	-0.412	0.953	0.889
0.6	0.345	0.667	0.964	0.890	-0.409	0.710	0.973	0.890	0.622	-0.776	0.980	0.890	-0.557	-0.797	0.952	0.883
1.0	0.246	0.127	0.959	0.866	-0.363	0.190	0.963	0.866	0.695	-1.099	0.984	0.864	-0.568	-1.171	0.960	0.848
1.3	0.113	-0.171	0.916	0.804	-0.330	-0.023	0.846	0.748	0.786	-1.507	0.962	0.799	-0.597	-1.444	0.934	0.811
1.6	0.026	-1.529	0.778	0.407	-0.322	-1.138	0.832	0.430	0.854	-1.805	0.976	0.660	-0.615	-1.708	0.932	0.532
1.9	-0.254	-2.784	0.694	0.333	-0.402	-1.935	0.750	0.333	0.824	-2.017	0.943	0.528	-0.637	-2.456	0.717	0.283
2.2	-0.521	-3.329	0.736	0.333	-0.521	-3.329	0.736	0.333	0.800	-2.123	0.849	0.415	-0.679	-3.079	0.623	0.226
2.6	-0.531	-3.881	0.694	0.306	-0.531	-3.881	0.694	0.306	0.850	-2.335	0.774	0.340	-0.732	-3.291	0.528	0.208
2.9	-0.766	-3.883	0.611	0.208	-0.766	-3.883	0.611	0.208	0.883	-2.519	0.724	0.302	-0.782	-3.397	0.453	0.151
3.2	-0.840	-4.303	0.503	0.184	-0.840	-4.303	0.503	0.184	0.928	-2.735	0.626	0.253	-0.828	-3.822	0.425	0.132
3.5	-0.955	-4.099	0.451	0.171	-0.955	-4.099	0.451	0.171	0.969	-2.919	0.555	0.208	-0.865	-4.034	0.397	0.094
3.8	-0.849	-3.985	0.320	0.117	-0.849	-3.985	0.320	0.117	1.009	-3.111	0.526	0.187	-0.955	-4.140	0.205	0.067
4.2	-0.796	-3.930	0.213	0.073	-0.796	-3.930	0.213	0.073	1.058	-3.286	0.477	0.177	-0.870	-3.864	0.131	0.047
4.5	-0.796	-4.140	0.192	0.064	-0.796	-4.140	0.192	0.064	1.110	-3.451	0.417	0.153	-0.892	-4.213	0.082	0.034

B.16 Hv20Rg07

	upper_starboard				upper_port				lower_starboard				lower_port			
time	y^*	z^*	Γ^*_{max}	Γ^*_{515}	y^*	z^*	Γ^*_{max}	Γ^*_{515}	y^*	z^*	Γ^*_{max}	Γ^*_{515}	y^*	z^*	Γ^*_{max}	Γ^*_{515}
0.0	0.500	2.000	0.967	0.898	-0.500	2.000	0.989	0.902	0.500	0.000	0.960	0.883	-0.500	0.000	0.938	0.880
0.3	0.459	1.654	0.966	0.900	-0.493	1.681	1.008	0.907	0.529	-0.394	0.969	0.896	-0.515	-0.397	0.945	0.888
0.6	0.419	1.303	0.958	0.899	-0.484	1.349	0.989	0.908	0.566	-0.774	0.972	0.894	-0.510	-0.786	0.944	0.887
1.0	0.377	0.933	0.952	0.889	-0.476	1.001	0.979	0.898	0.609	-1.130	0.969	0.881	-0.501	-1.167	0.938	0.876
1.3	0.324	0.552	0.939	0.859	-0.475	0.637	0.969	0.868	0.647	-1.473	0.964	0.848	-0.485	-1.540	0.933	0.843
1.6	0.265	0.142	0.928	0.789	-0.478	0.244	0.964	0.795	0.700	-1.803	0.955	0.772	-0.474	-1.902	0.929	0.767
1.9	0.191	-0.303	0.896	0.680	-0.493	-0.181	0.912	0.680	0.757	-2.113	0.948	0.674	-0.454	-2.260	0.920	0.670
2.2	0.093	-0.818	0.750	0.556	-0.534	-0.656	0.806	0.569	0.825	-2.405	0.936	0.572	-0.443	-2.585	0.887	0.565
2.6	-0.297	-1.199	0.641	0.524	-0.297	-1.199	0.641	0.524	0.900	-2.665	0.902	0.480	-0.417	-2.902	0.856	0.474
2.9	-0.392	-1.640	0.552	0.431	-0.392	-1.640	0.552	0.431	0.982	-2.901	0.844	0.413	-0.375	-3.183	0.820	0.413
3.2	-0.413	-2.030	0.562	0.416	-0.413	-2.030	0.562	0.416	1.069	-3.118	0.745	0.360	-0.300	-3.460	0.749	0.357
3.5	-0.424	-2.498	0.506	0.416	-0.424	-2.498	0.506	0.416	1.158	-3.309	0.653	0.306	-0.187	-3.736	0.667	0.316
3.8	-0.662	-2.892	0.593	0.416	-0.662	-2.892	0.593	0.416	1.255	-3.484	0.590	0.269	-0.058	-4.034	0.444	0.253
4.2	-0.957	-2.822	0.531	0.374	-0.957	-2.822	0.531	0.374	1.343	-3.638	0.554	0.228	0.116	-4.365	0.289	0.179
4.5	-0.824	-3.152	0.522	0.349	-0.824	-3.152	0.522	0.349	1.410	-3.786	0.506	0.209	0.167	-4.520	0.221	0.161

B.17 Hv25Rg07

	upper_starboard				upper_port				lower_starboard				lower_port			
time	y^*	z^*	Γ^*_{max}	Γ^*_{515}	y^*	z^*	Γ^*_{max}	Γ^*_{515}	y^*	z^*	Γ^*_{max}	Γ^*_{515}	y^*	z^*	Γ^*_{max}	Γ^*_{515}
0.0	0.500	2.500	0.977	0.889	-0.500	2.500	0.980	0.899	0.500	0.000	0.946	0.879	-0.500	0.000	0.935	0.886
0.3	0.472	2.070	0.976	0.895	-0.485	2.082	1.014	0.901	0.523	-0.341	0.967	0.896	-0.510	-0.343	0.941	0.886
0.6	0.453	1.621	0.964	0.893	-0.483	1.650	1.005	0.899	0.558	-0.676	0.963	0.893	-0.506	-0.687	0.935	0.883
1.0	0.420	1.163	0.959	0.891	-0.486	1.207	0.996	0.897	0.603	-0.999	0.961	0.890	-0.507	-1.025	0.929	0.881
1.3	0.368	0.678	0.953	0.884	-0.488	0.750	0.989	0.891	0.656	-1.303	0.956	0.884	-0.507	-1.361	0.925	0.873
1.6	0.301	0.148	0.942	0.851	-0.495	0.252	0.980	0.860	0.726	-1.591	0.952	0.853	-0.514	-1.690	0.921	0.841
1.9	0.200	-0.452	0.920	0.769	-0.523	-0.290	0.960	0.774	0.817	-1.846	0.945	0.777	-0.522	-2.011	0.913	0.764
2.2	0.050	-1.151	0.848	0.640	-0.593	-0.879	0.855	0.620	0.929	-2.036	0.933	0.663	-0.524	-2.336	0.890	0.648
2.6	-0.024	-1.887	0.748	0.487	-0.737	-1.376	0.710	0.441	0.999	-2.143	0.892	0.519	-0.487	-2.702	0.826	0.502
2.9	-0.199	-2.447	0.470	0.293	-0.619	-2.028	0.559	0.295	1.002	-2.239	0.800	0.398	-0.334	-3.063	0.611	0.378
3.2	-0.135	-3.055	0.390	0.218	-0.637	-2.380	0.449	0.223	0.973	-2.368	0.732	0.319	-0.069	-3.528	0.425	0.250
3.5																
3.8																
4.2																
4.5																

B.18 Hv30Rg07

	upper_starboard				upper_port				lower_starboard				lower_port			
time	y^*	z^*	Γ^*_{max}	Γ^*_{515}	y^*	z^*	Γ^*_{max}	Γ^*_{515}	y^*	z^*	Γ^*_{max}	Γ^*_{515}	y^*	z^*	Γ^*_{max}	Γ^*_{515}
0.0	0.500	3.000	0.982	0.898	-0.500	3.000	0.961	0.893	0.500	0.000	0.962	0.883	-0.500	0.000	0.940	0.880
0.3	0.484	2.708	0.973	0.895	-0.460	2.710	1.009	0.896	0.509	-0.377	0.975	0.893	-0.499	-0.381	0.957	0.884
0.6	0.482	2.404	0.971	0.893	-0.431	2.403	1.004	0.894	0.532	-0.751	0.975	0.888	-0.480	-0.765	0.951	0.883
1.0	0.477	2.087	0.967	0.894	-0.419	2.088	0.993	0.896	0.554	-1.124	0.972	0.889	-0.457	-1.151	0.948	0.883
1.3	0.466	1.772	0.965	0.891	-0.417	1.766	0.990	0.893	0.582	-1.488	0.972	0.885	-0.430	-1.546	0.944	0.875
1.6	0.463	1.450	0.970	0.872	-0.417	1.446	0.982	0.875	0.616	-1.850	0.979	0.860	-0.411	-1.929	0.947	0.850
1.9	0.454	1.130	0.970	0.815	-0.423	1.137	0.986	0.817	0.650	-2.203	0.977	0.795	-0.391	-2.305	0.945	0.785
2.2	0.448	0.815	0.969	0.705	-0.427	0.828	0.987	0.703	0.692	-2.548	0.963	0.682	-0.372	-2.661	0.934	0.677
2.6	0.435	0.498	0.950	0.581	-0.438	0.520	0.961	0.583	0.743	-2.877	0.933	0.563	-0.364	-3.000	0.912	0.552
2.9	0.411	0.176	0.898	0.476	-0.446	0.213	0.914	0.485	0.787	-3.192	0.902	0.474	-0.355	-3.319	0.892	0.465
3.2	0.395	-0.153	0.807	0.395	-0.462	-0.099	0.832	0.403	0.845	-3.491	0.829	0.398	-0.335	-3.603	0.815	0.388
3.5	0.374	-0.483	0.732	0.327	-0.473	-0.414	0.726	0.337	0.890	-3.769	0.761	0.340	-0.326	-3.884	0.740	0.325
3.8	0.348	-0.799	0.608	0.268	-0.507	-0.730	0.573	0.277	0.944	-4.026	0.673	0.288	-0.309	-4.146	0.644	0.286
4.2	0.316	-1.131	0.499	0.200	-0.512	-1.054	0.430	0.181	0.996	-4.272	0.599	0.250	-0.285	-4.413	0.570	0.241
4.5	0.372	-1.355	0.329	0.080	-0.581	-1.259	0.382	0.129	1.039	-4.505	0.518	0.220	-0.263	-4.662	0.527	0.213

B.19 Single wake vortex pair at $\Gamma_0 = 530\mathrm{m}^2/s$

	starboard				port			
time	y^*	z^*	Γ^*_{max}	Γ^*_{515}	y^*	z^*	Γ^*_{max}	Γ^*_{515}
0.0	0.500	0.000	0.986	0.878	-0.500	0.000	0.958	0.889
0.4	0.506	-0.235	0.981	0.894	-0.489	-0.238	0.945	0.882
0.8	0.512	-0.479	0.981	0.885	-0.474	-0.484	0.945	0.874
1.1	0.530	-0.719	0.985	0.867	-0.445	-0.737	0.944	0.858
1.5	0.554	-0.957	0.983	0.841	-0.416	-0.995	0.945	0.833
1.9	0.578	-1.202	0.970	0.796	-0.383	-1.259	0.940	0.790
2.3	0.602	-1.483	0.967	0.736	-0.352	-1.566	0.933	0.750
2.7	0.628	-1.680	0.969	0.684	-0.321	-1.790	0.921	0.672
3.0	0.659	-1.924	0.962	0.615	-0.288	-2.060	0.918	0.607
3.4	0.693	-2.164	0.946	0.542	-0.264	-2.321	0.904	0.542
3.8	0.727	-2.408	0.901	0.467	-0.243	-2.565	0.866	0.474
4.2	0.772	-2.649	0.824	0.414	-0.211	-2.808	0.822	0.414
4.6	0.817	-2.873	0.761	0.364	-0.184	-3.033	0.786	0.370
4.9	0.865	-3.085	0.697	0.326	-0.167	-3.257	0.698	0.334
5.3	0.916	-3.279	0.598	0.272	-0.153	-3.468	0.631	0.293

B.20 Single wake vortex pair at $\Gamma_0 = 360\mathrm{m}^2/s$

	starboard				port			
time	y^*	z^*	Γ^*_{max}	Γ^*_{515}	y^*	z^*	Γ^*_{max}	Γ^*_{515}
0.0	0.500	0.000	0.962	0.883	-0.500	0.000	0.940	0.880
0.3	0.505	-0.356	0.980	0.893	-0.488	-0.357	0.955	0.886
0.5	0.527	-0.719	0.984	0.879	-0.462	-0.729	0.957	0.872
0.8	0.550	-1.079	0.984	0.839	-0.434	-1.106	0.958	0.841
1.0	0.564	-1.437	0.979	0.789	-0.401	-1.496	0.954	0.779
1.3	0.601	-1.798	0.980	0.715	-0.370	-1.879	0.947	0.710
1.5	0.628	-2.156	0.971	0.622	-0.348	-2.260	0.940	0.619
1.8	0.676	-2.511	0.941	0.532	-0.320	-2.622	0.909	0.526
2.1	0.718	-2.845	0.898	0.447	-0.298	-2.968	0.876	0.447
2.3	0.764	-3.169	0.826	0.380	-0.271	-3.305	0.815	0.366
2.6	0.809	-3.489	0.725	0.311	-0.258	-3.617	0.703	0.305
2.8	0.859	-3.793	0.590	0.257	-0.220	-3.905	0.633	0.243
3.1	0.905	-4.098	0.498	0.201	-0.184	-4.227	0.527	0.220
3.4	0.965	-4.382	0.470	0.151	-0.158	-4.519	0.465	0.183
3.6	1.023	-4.636	0.396	0.094	-0.137	-4.793	0.368	0.122

국문초록

항공기의 와후류는 자기 유도에 의해 하강하는 특징을 가지기 때문에 그 위치를 식별할 수 있다. 이륙하는 조종사는 선행 항공기의 이륙 지점 앞에서 이륙하고 선행 항공기의 등반 경로 위로 비행하면 와후류를 피할 수 있다. 이러한 회피 비행은 두 개의 와후류가 동시에 근접하여 대기 중에 존재하는 상황이 발생할 수 있으며 두 쌍 사이의 거리가 충분히 가까운 경우 상호작용이 발생할 것이다. 또한 선행 항공기에서 발생한 와후류가 인접 활주로로 이동할 경우에도 와후류 간의 상호작용이 발생할 수 있다. 본 연구는 선행 항공기와 후행 공기에 의해 생성된 서로 다른 wake vortex pair간의 상호 작용으로 인해 발생하는 이동 및 소산 특성 프로세스를 수치해석으로 분석하였다.

후행 항공기의 높은 고도는 초기 조건으로 고려되었으며, 와후류의 불안정성과 비선형 수송 및 붕괴를 설명하기 위해 대기 난류 조건이 수치해석에 적용되었다. 해석 결과를 분석하여 단일 와후류 쌍으로의 합병, 빠른 소산, vortex ring의 형성 이후 하부 vortex pair를 변형하거나 변형없이 각각 소산하는 프로세스를 확인하였다.

본 연구의 해석은 선행 항공기에 의해 형성된 와후류가 상호 작용으로 후행 항공기의 와후류를 효과적으로 소산 시킬 수 있음을 밝혀냈다. 또한, 와후류 쌍의 상호 작용을 고려할 때 발생하는 추가적인 소산 효과를 이륙 분리 시간에 적용하여 효율성을 분석하였다. 선행 항공기에서 발생하는 vortex 간의 상호작용을 고려할 때 항공기 간 이륙 분리 시간을 줄이고 공항 용량을 늘리는 데 도움이 될 수 있다는 것을 확인하였다.

주요어: 항공기 와후류, 와류 상호작용, 전산 유체해석, 가시화, 공항 이착륙 분리간격, 항공교통관제

학 번 : 2015-30174

성 명 : 조 준 호